School of Chemical and Petroleum Engineering

Department of Chemical Engineering

Influence of surfactants on Fe_2O_3 and WO_3 nanostructured photoanodes and their photoelectrochemical behaviour

Amir Memar

This thesis is presented for the degree of

Doctor of Philosophy

of

Curtin University

May 2014

DECLARATION

To the best of my knowledge and belief this thesis contains no material previously published by any other person except where due acknowledgement has been made.
This thesis contains no material which has been accepted for the award of any other degree or diploma in any university.

Signature: ……

Date: ……

ACKNOWLEDGEMENTS

I would like to express the deepest of gratitude to my supervisors, Dr. Chi M. Phan and Prof. Moses O. Tade, whose patience, vision, encouragement and advice guided me through my PhD program and the completion of this thesis at the Chemical Engineering Department, Curtin University. I would also like to thank Prof. Ming Ang, as Chair Person of the Thesis Committee, who has organized regular meetings to support and help in resolving any issues raised by my research.

I would like to thank Curtin University for supporting this work with a Curtin International Postgraduate Research Scholarship (CIPRS).

My special thanks go to the technicians at the Chemical Engineering Lab, Karen Haynes and all of her team members, who have given very much assistance during the experimental work. I would also like to thank the Curtin Electron Microscope Facility and, particularly, Dr. Rob Hart and Elaine Miller for their technical support. I give my best regards to my colleagues within Curtin University, my friends and all the others who have assisted me in any way during my studies in Australia.

I am warmly thankful to my parents for their unwavering support during my time of studying abroad. My cheerful thank you goes out to my lovely wife, Mrs Ghazaleh Pourfallah, for her constant encouragement and steadfastness when I felt alone, weak and tired.

ABSTRACT

Influence of surfactants on Fe_2O_3 and WO_3 nanostructured photoanodes and their photoelectrochemical behaviour

Amir Memar

Hydrogen, as an energy carrier, plays an important role in renewable energy issues. One of the most promising methods of producing hydrogen is photoelectrochemical water splitting by solar light. However, photoelectrochemical water splitting is still too inefficient for large scale commercialization due to the poor performance of photoelectrodes. Despite numerous efforts to improve photoelectrode performance, there are still some challenges that need to be addressed, especially the efficiency and stability of the photoelectrode.

This study aims to improve photoelectrode performance by varying the nanostructural characteristics of different metal oxides, Fe_2O_3 and WO_3, in a single layer photoanode. The surface area of a nanostructured electrode is a key factor in the efficiency of a photoelectric cell. Increasing the surface area of nanoparticles with small crystal size can increase the photoactivity of these particles. Additionally, charge recombination could be encouraged by increasing the amount of surface defects. Consequently, the optimization of these two key factors is needed to obtain suitable crystalline size in order to improve the efficiency and stability of photoelectrodes.

Metal oxide nanostructures can be prepared by sputtering, electro-spinning, chemical vapour deposition or sol-gel processing. Among these methods, sol-gel technology for deposition of thin nanostructure has gained impetus in the last decade owing to the low capital cost and its adaptability towards large area deposition. In the sol-gel process, surfactants are required to prevent agglomeration and enhance the quality of the nanostructures. Moreover, surfactants can be utilized to control the grain size of metal oxides, which is important for photocatalytic processes like water splitting. However,

the influence of surfactant on the grain size of nanoparticles is not well understood. In this study, we have investigated the effects of various surfactants on characterized size (e.g. crystallite, grain or particle size) of Fe_2O_3 and WO_3 nanoparticles.

Furthermore, the effect of a surfactant`s adsorption time and vacant position were investigated and related to the characterized size of nanoparticles. Also, we have used these relationships to model the effect of surfactant size (head and tail) on the characteristic size of Fe_2O_3 and WO_3 nanoparticles when they were treated with cationic and Triton surfactants, respectively.

The results highlighted the significance of surfactant size within the calcination process and upon the produced anodes. In addition to water splitting, the findings have important implications for other applications in which a precise control of the metal oxide grain size is desirable.

PUBLICATIONS BY THE AUTHOR IN SUPPORT OF THIS THESIS

1. **Amir Memar**, Chi M. Phan, Moses O. Tade "Influence of Surfactants on Fe_2O_3 Nanostructure Photoanode", *International Journal of Hydrogen Energy, Elsevier publication* 37 (2012) pp. 16835-16843.

2. **Amir Memar**, Chi M. Phan, Moses O. Tade "Controlling particle size and photoelectrochemical properties of nanostructured WO_3 with surfactants", *Applied Surface Science, Elsevier publication* 305 (2014) pp. 760-767.

3. **Amir Memar**, Chi M. Phan, Moses O. Tade "Study on photocatalytic activity of $(WO_3)_{1-x}$-$(Fe_2O_3)_x$ nanocomposite photoanode for hydrogen production" under revision for submission.

4. **Amir Memar**, Chi M. Phan, Moses O. Tade "Influence of surfactants on Fe_2O_3 nanostructure photoanode", *Chemeca 2012 New Zealand*, September 23–26, 2012.

5. **Amir Memar**, Chi M. Phan, Moses O. Tade "Controlling the grain size of nanoparticles in calcination process by surfactants", *9th World Congress of Chemical Engineering (WCCE9)* Coex, Seoul, Korea, August 18-23, 2013.

TABLE OF CONTENTS

LIST OF FIGURES

LIST OF TABLES

LIST OF ABBREVIATIONS

PEG 300	Polyethylene glycol 300
F127	Pluronic F127
CTAB	Cetyltrimethylammonium bromide
OTAB	Octadecyltrimethylammonium bromide
TTAB	Tetradecyltrimethylammonium bromide
T-X45	Triton X-45
T-X100	Triton X-100
T-X305	Triton X-305
T-X405	Triton X-405
T-X705	Triton X-705
SDS	Sodium dodecyl sulfate
PPTA	Peroxopolytungstic acid
SEM	Scanning electron microscope
EDX	Energy-dispersive X-ray spectroscopy
AFM	Atomic force microscopy
XRD	X-ray diffraction
ABPE	Applied bias photon-to-current efficiency

LIST OF SYMBOLS

E_v	Valence band
E_c	Conduction band
E_g	Band-gap
E_F	Fermi level
E_i	Intrinsic Fermi level
E_B	Bonding energy
λ	Wavelength
n_0	Concentration of conducting electron
p_0	Electron hole concentration
n_i	Intrinsic carrier concentration
α	Absorption coefficient
hv	Energy of the incident photon
ρ	Specific density
S_g	BET surface area
eV	Electron volt
θ	Diffraction angle
β	Full width at half maximum
R_z	Surface roughness
$Vaoc$	circuit potential Open

J_{ph}	Photocurrent density
P_{total}	Intensity of the incident light
V_b	Applied bias
μ_e	Electron mobility
μ_h	Hole mobility
ε	Dielectric constant
k_b	Boltzman constant
N_D	Carrier concentration
L_h	Hole diffusion length
D	Particle size
D_0	Critical particle size
M	Molecular weight of surfactants
t_{eff}	Absorption time
C_p	Coverage factor

1. INTRODUCTION

1.1. Background

To support every aspect of human life, the global economy uses a massive amount of energy. This energy could be produced by direct combustion of fossil fuel or by harnessing various alternative sources of energy for heat or electricity. At present, approximately 88% of the world's energy supply is derived from fossil fuel [1]. Combustion of fossil fuel brings about severe pollution and contributes to the greenhouse effect. Hence, developing technologies that utilize renewable energies is an urgent priority. So far, scientists have developed a number of ways to harness energy from the ongoing natural processes of our environment. These renewable sources include water (as hydroelectricity), biomass, wind, geothermal, ocean and solar energies. Together, these resources provide a hope of producing carbon-free energy.

1.1.1. Current energy use

Australia is rich in commodities, including fossil fuel and uranium reserves, and is one of the few countries belonging to the Organization for Economic Cooperation and Development (OECD) that is a significant net hydrocarbon exporter, exporting over 70% of its total energy production, according to government sources. Australia was the world's second largest coal exporter, based on weight, in 2011 and the third largest exporter of liquefied natural gas (LNG) in 2012. Australia is heavily dependent upon fossil fuels for its primary energy consumption. In 2011, oil accounted for 36% of the country's energy usage (Figure 1-1). Coal and natural gas were at 33% and 25% of fuel used, respectively. Renewable sources, including hydroelectricity, wind, solar and biomass that are consumed on a lesser scale, accounted for about 6% of the total consumption. Although the country is rich in uranium, Australia has no nuclear powered electricity generation capacity. This could be due to the fact that Australia has historically used low cost coal and natural gas. The new carbon dioxide emissions tax implemented in July 2012 may lead to an increase in demand for natural gas and renewables to replace some coal or oil used in power generation and transportation. The

Australian government projects that the natural gas share of primary energy consumption will increase to 35% by 2035 [2].

1.1.2. Renewable energy options

Renewable energies could be one of the solutions for today's environmental problems. Renewable energy resources, such as wind, solar and hydropower, provide humans with clean alternatives to fossil fuels. These resources will never run out and do not produce any pollution or greenhouse gases. The renewable energies which are commonly used are as follow [3]:

(a) Solar energy
(b) Wind energy
(c) Hydropower energy
(d) Biomass energy (food sources)
(e) Hydrogen energy
(f) Geothermal energy
(g) Ocean energy

Solar energy is mostly used to generate electricity. However, most forms of renewable energy come either directly or indirectly from the sun. For instance, wind energy normally generates air pressure differences which are the result of uneven heating of the atmosphere by the sun. Solar energy also has an impact on biomass energy production which comes from consumption of plants. Furthermore, by heating up sea water, the sun influences its evaporation and precipitation, and produces hydropower energy. In past centuries, renewable energy was normally used to sail ships and drive windmills that could grind grain. However, today, by utilizing wind turbines and capturing wind energy, electricity is produced. Furthermore, water alone is a powerful force. The global cycle of evaporation and precipitation can generate a renewable source of energy. Heating of ocean water by solar radiation causes evaporation that forms clouds. The formed clouds then return to Earth as rain or snow that drains into rivers and streams, which flow back to the ocean. Mechanical energy can be obtained by capturing that water flow energy via water wheels. This energy then can be converted to electricity by

turbines and generators. Even though wood is still the most common source of biomass energy, other sources such as organic components from industrial wastes, methane gas, food crops, grasses and other plants also are considered as sources of biomass energy. Biomass can be directly converted to electricity or used as fuel for transportation. Hydrogen can be considered as a wonderful energy carrier. Hydrogen also is the most common element in the world (as two thirds of all water consists of hydrogen). Additionally, the combination of this element with other elements can be found in nature. However, it needs to be separated before it can be utilized as a source of energy. This renewable and clean energy can be utilized to power vehicles, replace natural gas for heating and cooking, and to generate electricity. Another sustainable and renewable energy can be produced by utilizing the heat inside the Earth (geothermal energy) which produces steam and hot water that can be used to power generators and produce electricity. Geothermal energy can be drawn from deep, underground reservoirs, by drilling, or from other geothermal reservoirs closer to the surface. The ocean provides various sources of renewable energy. Ocean waves and tides can be harvested and converted to electricity. Also, the accumulated heat energy in sea water can be converted to electricity. Despite these advantages, using current technologies, ocean energy is not cost-effective when compared to other renewable energy sources. However, this renewable energy remains an important potential energy source for the future.

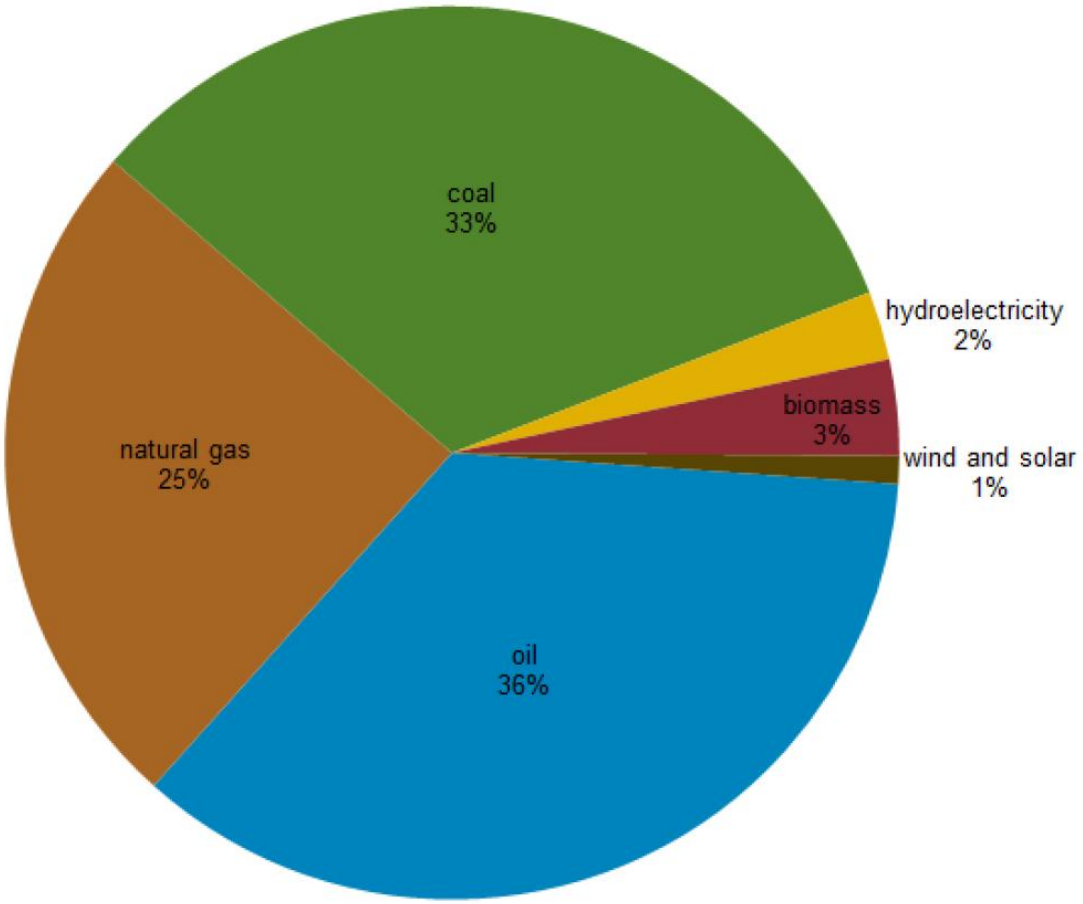

Figure 1-1 Sources of Australia's primary energy consumption in 2011 [2].

1.1.3. Solar Energy

Solar energy has been considered as the most commonly used renewable source for electricity generation at present [4]. Fortunately, 3×10^{24} J of energy is emitted from the sun to earth annually, which is about 10^4 times more than today's human consumption. It means that all of humanity's needs would be fulfilled if only 0.1% of the earth's surface was covered by 10 % efficient solar cells [5].

Different methods have been utilized, so far, to harness radiated light and heat from the sun. Solar heating, solar photovoltaics, solar thermal electricity, solar architecture and artificial photosynthesis have been considered as some methods of capturing solar energy. However, solid-state photovoltaic (PV) devices are known to be the most efficient method of harvesting solar energy. PV cells have recently gained the highest

overall conversion efficiency of 42% [6]. However, they can only produce electricity. For many applications, electricity is not the most practical conversion because it is difficult to store efficiently. Also, the PV cells cannot gain any solar irradiation during the night. Therefore, the energy must be stored for night time usage. Efficiency losses during the charging and discharging processes, and unacceptably short operational lifetimes make electricity storage inefficient. Therefore, storage remains one of the main obstacles for solar energy production. As a result, an effective energy carrier is needed. At present, one of the important energy carriers that can be synthesized efficiently, without material limitations, is hydrogen (H_2). Hydrogen, as an alternative fuel with respect to fossil fuels, is of great interest. Furthermore, the combustion of hydrogen only produces water. Thus, hydrogen as an energy carrier is one of the most promising yet challenging prospects among several clean and sustainable energy systems [7, 8].

1.2. Hydrogen Production

Solar energy can be stored by an energy carrier like hydrogen which is a renewable, sustainable and clean source of energy [9]. Each atom of hydrogen consists of one proton and one electron. Hydrogen atoms are very reactive and prefer to combine together and form molecular pairs (H_2). However, mixtures of this molecule with an oxidant like O_2, Cl, F, N_2O_4, etc., can result in combustion. Therefore, H_2 (like other fuels) requires proper understanding and handling to avoid any undesirable flammable or explosive environments. Hydrogen is known as an effective energy carrier but is not a primary source of energy. In order to produce hydrogen energy, it must be extracted from substances like natural gas, water, coal or any other hydrocarbon [10]. There are various methods of producing hydrogen (Figure 1-2) such as:

(a) Electrolysis
(b) Photolysis
(c) Thermochemical process
(d) Direct thermal decomposition (thermolysis)
(e) Biological production

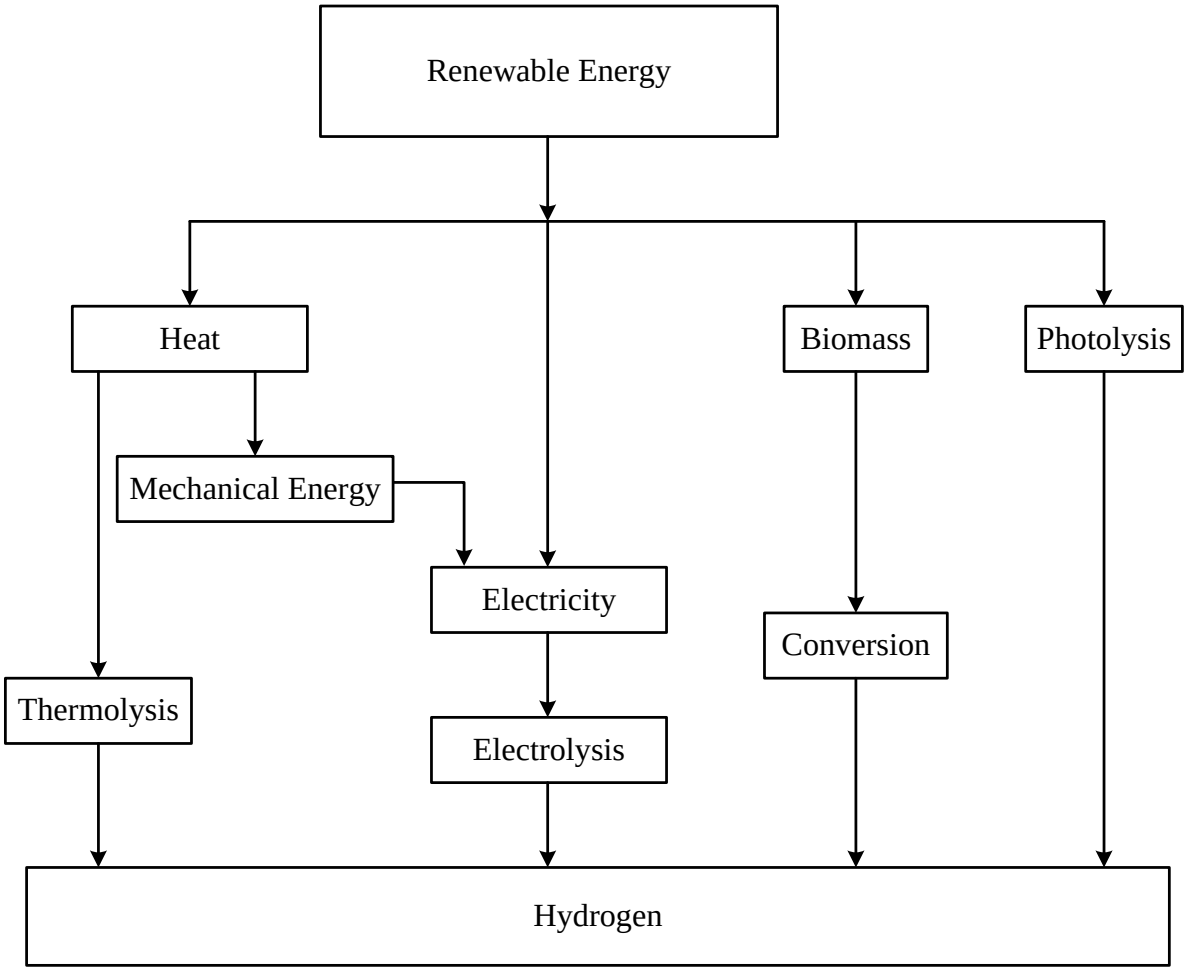

Figure 1-2 Sustainable paths to hydrogen production

As can be seen in Table 1-1, hydrogen is only 5×10^{-5} (volume ratio) of the earth's atmosphere. Thus, extracting hydrogen from the atmospheric air would be really expensive and time consuming [11]. Hydrogen production using steam reformation of natural gas is considered to be one of the most promising methods. However, this method is not an environmentally friendly process due to the generation of numerous pollutants, such as sulphur dioxide (SO_2), nitrogen oxides (NO_x) and carbon dioxide (CO_2) [12-14]. Having these pollutants in the air would result in various unwanted phenomena, such as acid rain and smog, which have negative impacts on human health [15].

Table 1-1 Composition of dry atmosphere (by volume) [16]

Gas	Volume (%)
Nitrogen (N_2)	78.084
Oxygen (O_2)	20.946
Argon (Ar)	0.9340
Carbon dioxide (CO_2)	0.0397
Neon (Ne)	0.001818
Helium (He)	0.000524
Methanol (CH_4)	0.000179
Krypton (Kr)	0.000114
Hydrogen (H_2)	0.000055

1.2.1. Photoelectrochemical water splitting process

One of the most promising methods of producing hydrogen is photoelectrochemical water splitting by solar light. Among various methods of producing hydrogen, direct splitting of water using photocatalysts has been given attention due to the availability and sustainability of this energy source. In this method, water molecules are broken down by applying a bias to electrodes immersed in an aqueous electrolyte. This results in the generation of hydrogen (H_2) and oxygen (O_2) at the cathode and anode, respectively (Figure 1-3). The produced hydrogen then can be used in fuel cells to produce electricity (Figure 1-4). Sustainable, renewable and green energy would be produced by this photoelectrochemical water splitting method.

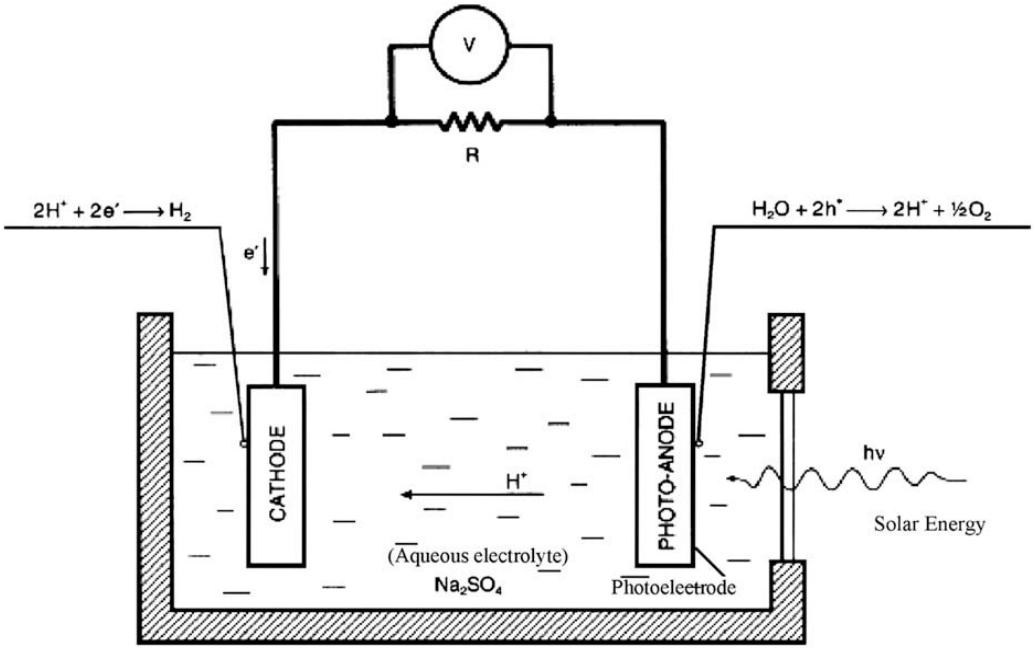

Figure 1-3 A schematic of a photoelectrochemical cell [17]

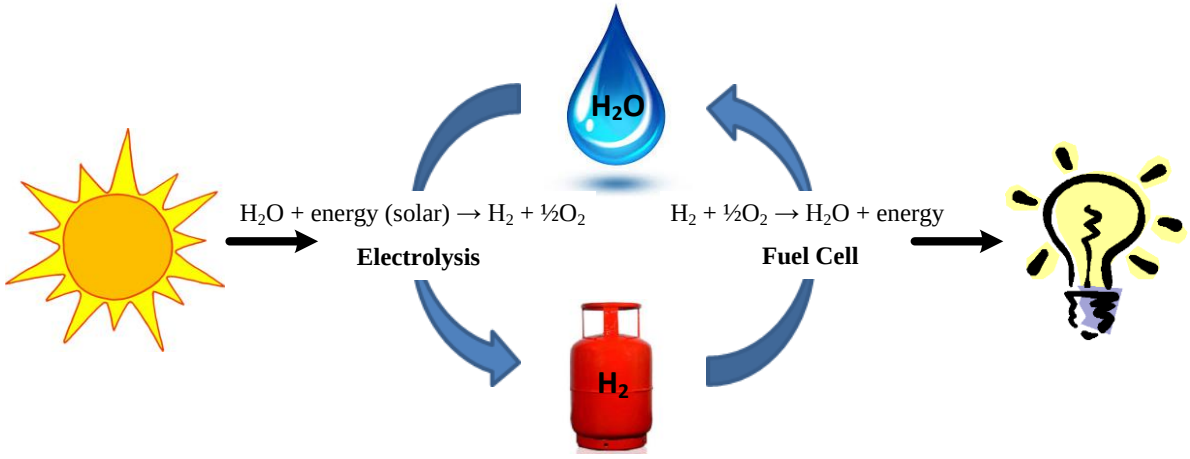

Figure 1-4 A schematic of renewable, sustainable and green energy produced by electrolysis of water

1.3. Motivations for this study

The photoelectrode is the main component of a photoelectrochemical water splitting cell. Numerous efforts have been made to prepare efficient photoelectrodes but there are challenges to overcome yet. Solving the two main problems of efficiency and stability has driven many studies on photoelectrode materials [14, 18].

Photoelectrodes normally are made using a metal oxide photoactive material, namely a "semiconductor". Semiconductor properties are determined by the surface characteristics of metal oxide nanoparticles [19, 20], specifically their grain size [21] and crystalline properties [22]. Surfactants often are employed to enhance the quality of nanoparticles, owing to their amphiphilic nature [23]. Hence, varying the structure of surfactants, at either head or tail, may have a deterministic effect on the surface characteristics of the semiconductor.

Surface characteristics of a photoelectrode`s nanoparticles are key factors for improving the efficiency and stability of a photoelectric cell. Increasing the surface area of nanoparticles by controlling grain size can increase the photoactivity of these particles. However, charge recombination could be created by increasing the number of surface defects. Consequently, optimization of these two key factors could lead to the achievement of optimum surface characteristics that would enhance the efficiency and stability of the photoelectric cell.

1.4. Contributions of this work

In this thesis, the problems of low efficiency and stability of semiconductors for photoelectrochemical water splitting applications was investigated and improved. By utilizing various surfactants (including cationic, anionic and non-ionic surfactants), the physical characteristics, solar absorption properties and, finally, photoelectrochemical activity of Fe_2O_3 and WO_3 nanoparticles was modified.

Also, we have successfully synthesised Fe_2O_3 nanoparticles in the range of 12 - 70 nm using different surfactants. Consequently, the photocatalytic activity of this photocatalyst was improved significantly. Additionally, we have succeeded in producing WO_3 nanoparticles in the range of 75 - 140 nm. Furthermore, a novel method was used

to model and predict the behaviour of nanoparticles after calcination using different series of Triton surfactants. The film thickness and roughness were linearly correlated to the surfactant size. Moreover, the photoelectrochemical properties of the synthesized WO_3 films also were correlated with the surfactant size.

1.5. Research objectives

In this study, we have quantified the influence of surfactant size (head and tail sizes) on the surface characteristics and photocatalytic activity levels of Fe_2O_3 and WO_3 by using various surfactants (anionic, non-ionic and cationic). Also, we have identified the effects of these surfactants on physical properties (morphology, film thickness, surface roughness and crystallite, grain and particle sizes) of WO_3 and Fe_2O_3. Furthermore, the photocatalytic activity of synthesised surfactant-treated metal oxides in a photoelectrochemical water splitting cell was investigated through measuring the photocurrent activity of each sample. The specific objectives of the thesis are to:

1. Synthesise and characterise the surfactant-treated nanoparticles: Fe_2O_3 and WO_3
2. Investigate the effects of surfactant size on the physical properties of nanomaterials
3. Optimize the nanoparticle grain and crystallite sizes utilizing different surfactants
4. Investigate the influence of surfactant on the photoelectrochemical properties of Fe_2O_3 and WO_3 nanomaterials

1.6. Hypothesis

Physical properties (morphology, film thickness, surface roughness and crystallinity, grain and particle sizes) and photoelectrochemical (PEC) properties of nanoparticles can be influenced by varying the surfactant molecules. Also, a predictable model can be developed to control the nanoparticle sizes using different surfactants. By addressing these issues, it is hypothesized that the influence of surfactants can be quantified and applied to improve the electrophotocatalytic properties of nanoparticles for water splitting processes.

1.7. Thesis organization

This thesis consists of six chapters. Chapter 1 (this chapter) describes the different sustainable and renewable energy systems and presents different methods of hydrogen production.

Chapter 2 presents some background information related to photoelectrochemistry and semiconductor theory. In this chapter, different setups for photoelectrochemical reactors also are discussed and the minimum requirements for the photoelectrochemical water splitting reaction are presented. Furthermore, the influence of different surfactants on modifying surface-related effects and the photocatalytic activity of metal oxides are reviewed.

Chapter 3 presents the preparation methods of different photocatalysts, along with the explanation of different characterization techniques which have been used during this PhD study. Chapters 4 and 5 outline the research works employed in the development of the photocatalytic activity of Fe_2O_3 and WO_3 for the application of hydrogen production.

Chapter 4 examines the iron oxide (Fe_2O_3) photocatalyst for hydrogen production via water splitting. In this study, Fe_2O_3 nanoparticles were synthesized by combination of different surfactants. The effect of the hydrocarbonic tail size of cationic surfactants on the crystallite size and photocatalytic activity of Fe_2O_3 is discussed. Chapter 4 also presents the modelling of surfactant adsorption kinetics for cationic surfactants. In this chapter we have modelled the behaviour of characterized size of Fe_2O_3 nanoparticles by varying the surfactant size. Also, we have investigated the effect of absorption time as well as vacant position of cationic surfactants on characterized size of nanoparticles. This chapter was published in the International Journal of Hydrogen Energy, in September 2011.

Chapter 5 investigates the influence of surfactant on the physical properties and photocatalytic activity of tungsten trioxide (WO_3) as a photocatalyst for photoelectrochemical water splitting purposes. In this study, the influence of surfactant head size in tuning of nanoparticle size and morphology, and consequently the photocurrent activity, of a WO_3 photoanode was investigated. Chapter 5 also presents

the modelling of surfactant adsorption kinetics for Triton surfactant series. In this chapter we have modelled the behaviour of characterized size of WO_3 nanoparticles by varying the surfactant size. Also, we have investigated the effect of absorption time as well as vacant position of Triton surfactants on characterized size of nanoparticles. This chapter was published in the Applied Surface Science, in April 2014.

Finally, chapter 6 briefly discusses all the experimental results and forms conclusions. Also, in this chapter, proposals for future work are discussed. A schematic diagram of the thesis layout is presented in Figure 1-5.

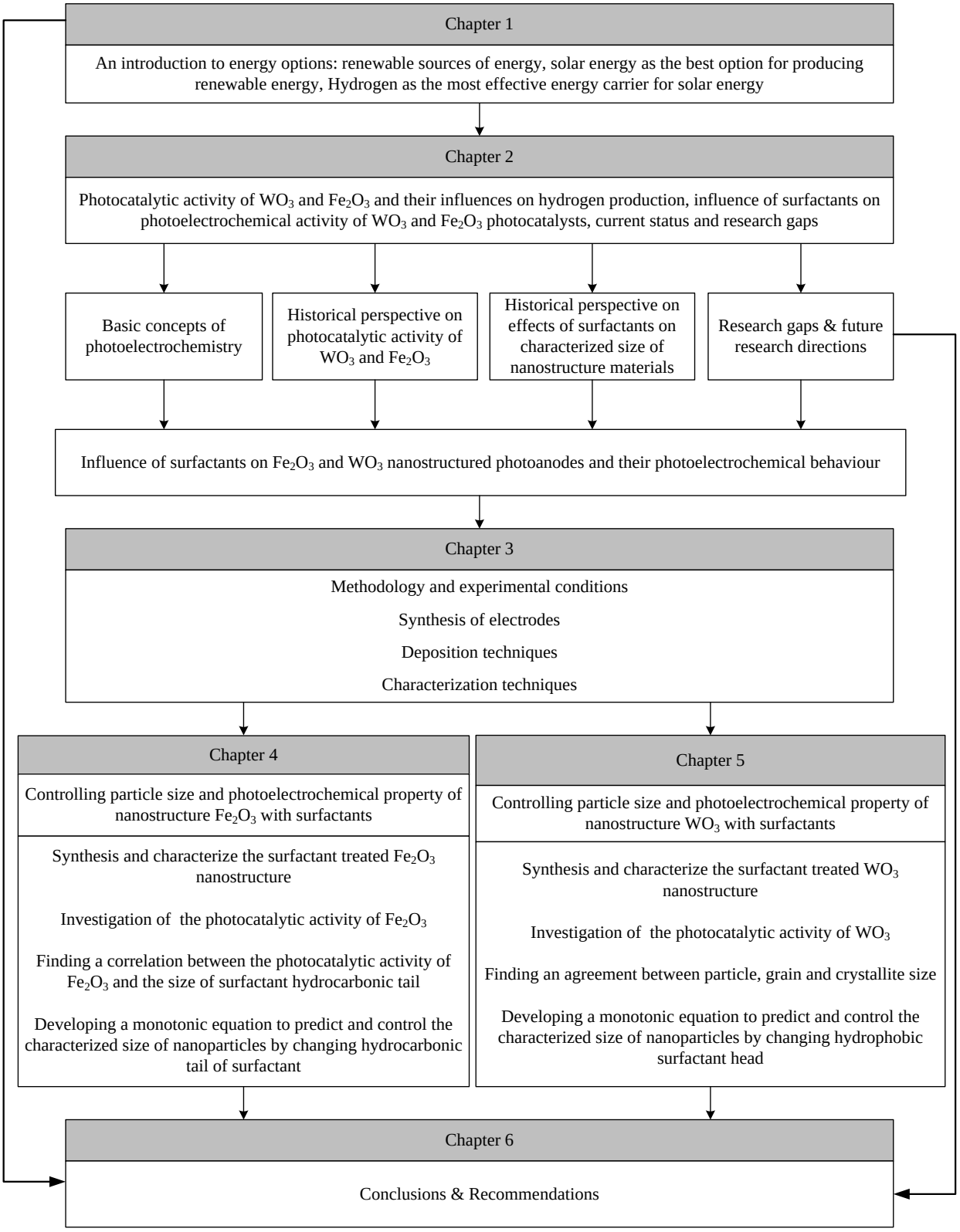

Figure 1-5 Schematic diagram of thesis layout

2. LITERATURE REVIEW

2.1. Photoelectrochemistry

To date, significant efforts have been done regarding to photoelectrochemical cells and the photo-processes occurring in semiconductor materials. These researches have highlighted new materials and reaction schemes. Although more efficient systems utilizing inexpensive and readily available semiconductors are still needed, the field of photoelectrochemistry has opened new areas in electrochemical research and has provided new insight into the interactions of light, electricity and chemical reactions in a number of different processes.

2.1.1. Photoelectrochemical cell setup

One of the most efficient and cost effective methods for converting solar energy into a chemical fuel is photoelectrochemical water splitting. In this method, a photoelectrode absorbs solar radiation and directly decomposes water into oxygen and hydrogen. The photoelectrochemical installation (Figure 2-1) encompasses two electrodes, which are wrapped up within an aqueous electrolyte in a vessel. In this case, either of the electrodes can be photoactive [24]. The vessel, with a quartz optical window, is filled with an aqueous electrolyte. The quartz optical window allows light to reach the photoactive electrode. The photoelectrode absorbs photons with sufficient energy to inject electrons from the valence shell to the conduction band of the semiconductor, creating electron-hole pairs. Holes oxidize water in the semiconductor surface and gaseous oxygen evolves at the photoanode surface. Simultaneously, hydrogen ions migrate to the cathode through the aqueous electrolyte, resulting in the reduction of hydrogen ions into gaseous hydrogen.

Water splitting will occur when the energetic requirements are met, as shown in Table 2-1, where the practical potential will be much higher than the minimum required to overcome over-potential and other system losses. The theoretically calculated electrode potential required for the electrolysis reaction is 1.229 eV [25, 26]. In conventional electrolysis, this energy is supplied from an external source such as a battery or solar

panel. The use of thin film photoactive materials as electrodes allows for the reduction and possible eventual elimination of any external voltage source. In addition to eliminating the need for a separate power source, the photoactive material used in these types of cell is quite inexpensive when compared to photovoltaic panels. With the development of the right semiconductor material, cells could be produced to output hydrogen and oxygen with water and sunlight as the only inputs. In a lab test situation for measurement of solar/photon-to-current conversion efficiency, a reference electrode also is used and this method is commonly referred to as the three electrodes cell. In practical applications, and also for measurement of true solar-to-hydrogen conversion efficiency, a two electrodes system is used [27].

The corresponding oxidation and reduction reactions are as follow:

Photoanode:

$2h\nu \rightarrow 2\bar{e} + 2h^{\cdot}$

$2h^{\cdot} + H_2O_{(liquid)} \rightarrow \frac{1}{2}\, O_{2(gas)} + 2H^{+}$ (2-1)

Cathode: $2H^{+} + 2\bar{e} \rightarrow H_{2(gas)}$

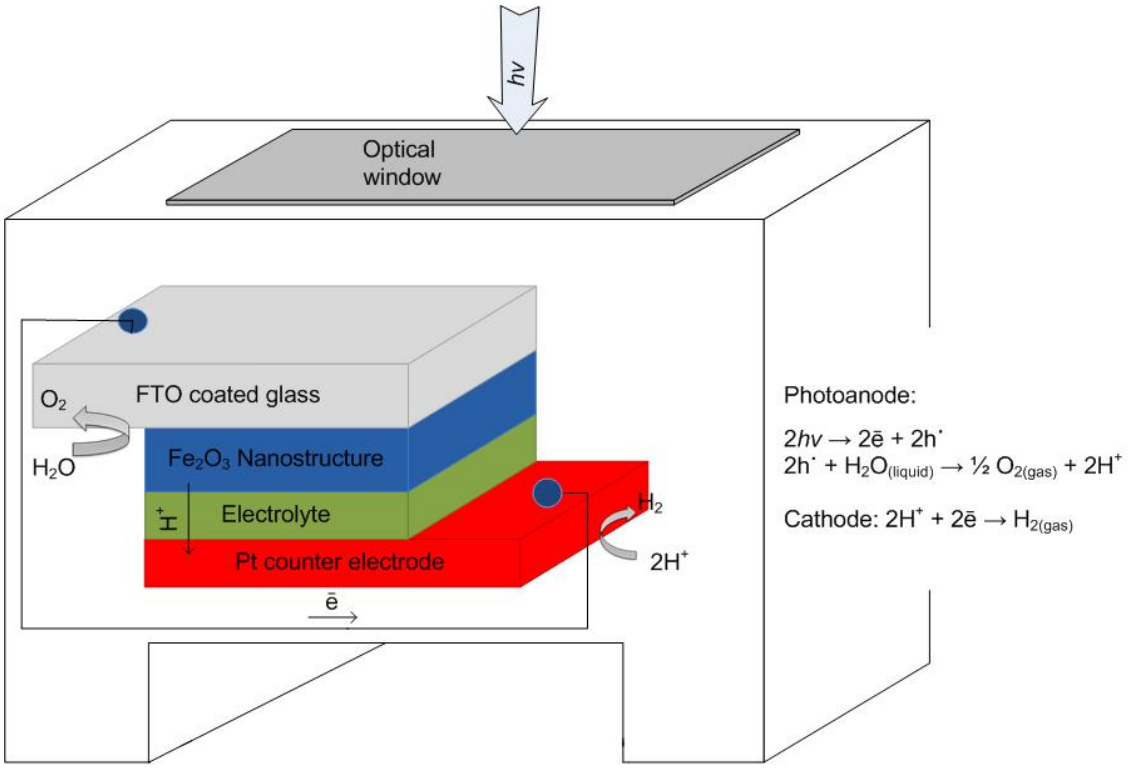

Figure 2-1 Structure of the photoelectrochemical cell

Table 2-1 Main PEC water splitting requirements

Conditions	Main requirements
PEC water splitting	$H_2O_{(liquid)} + 2h\upsilon \rightarrow \frac{1}{2}O_{2(gas)} + H_{2(gas)}$
Minimum potential requirement	$E°_{H_2O}(25°C)_{min} = 1.229\ eV$
For efficient utilization of sunlight	UV> $h\upsilon$ (Vis)> IR $h\upsilon \geq E_{band\text{-}gap}$

2.1.2. Solar requirement

The extra-terrestrial solar spectral distribution is modified through interactions with the gases and particles in the atmosphere to produce terrestrial spectral distributions that vary with respect to both amplitude and wavelength over a very wide range. In practice, the photoelectrochemical water splitting system is illuminated with the local solar spectrum. A common standard reference solar spectrum is the AM1.5 global solar spectrum shown in Figure 2-2. The air mass (AM) factor describes the effect of the Earth's atmosphere on the incident solar spectrum, where AM = 1/cos(α), where α, the zenith angle, is the angle between the overhead and actual position of the sun. The sharp dips in the spectrum are due to the absorption of certain wavelength bands by gases such as H_2O, O_3, O_2 and CO_2 in the atmosphere.

The solar spectrum reaching the surface of the Earth is dependent upon the location, season, time of day and local weather. However, most measurements of the water splitting affect are undertaken in laboratories using illumination from artificial light sources (e.g. xenon or mercury lamps). Spectral differences between artificial light sources and the AM1.5 reference spectrum can lead to erroneous efficiency measurements since the photocurrent generated by the photocatalyst material is highly dependent on the spectrum and intensity of the illumination source [28, 29].

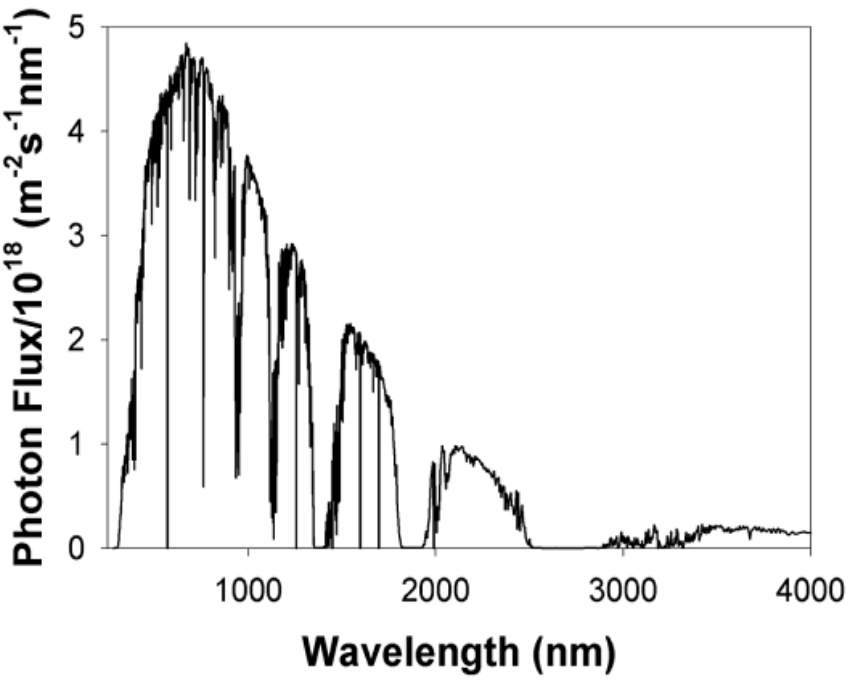

Figure 2-2 AM1.5 standard solar reference spectrum (adapted from [28]).

2.1.3. Photoelectrode preparation

The photoelectrode (Figure 2-3) is one of the most important constituents of a photoelectrochemical water splitting reactor; by applying semiconductors with suitable band-gaps and band-edges, solar radiation absorption can be improved. Transparent, conductive glass or metal foil normally is used as the substrate. By depositing a thin layer of the semiconductor on top of the conductive side of the substrate, the photoelectrode can be made. In order to make an electrical connection, a small area (usually a strip at the top or to the side of the conductive substrate) is left uncoated. The ohmic contact normally is made by attaching a copper wire to the exposed part, using silver conductive glue and covering the connection with epoxy resin to provide insulation and also to strengthen the connection. Subsequently, the copper wire is put into a glass tube, to be protected and also to act as a handle for the photoelectrode. All of the four edges and the back of the photoelectrode then are covered with epoxy resin for insulation. In photoelectrochemical water splitting studies, the photoelectrode produced by this method is completely immersed in the electrolyte.

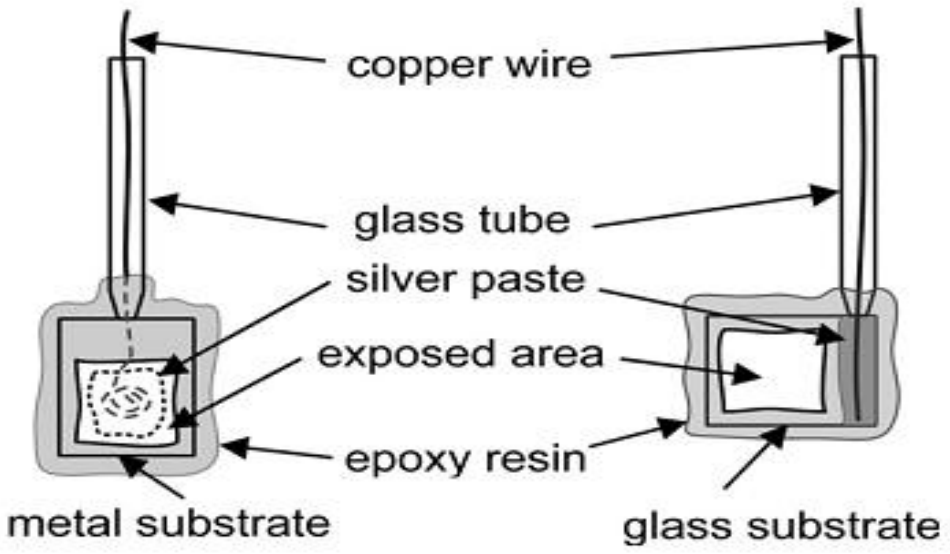

Figure 2-3 Components of a photoelectrode (adapted from [24]).

2.1.4. Photoelectrode configuration

The main photoactive material used for the photoelectrode is a semiconductor. The photoelectrochemical, water splitting semiconductor is categorized as a conventional photovoltaic material and metal oxide. The semiconductor can be n-type, like TiO_2 [17], p-type, like InP [30], or a coupling of n-type and p-type, like n-GaAs/p-InP [31].

2.1.5. Biased / non-biased reactors

The direct decomposition of water, with no other external energy, is an ideal way for photoelectrochemical water splitting to produce hydrogen; indeed, with appropriate band-gap, band-edge and natural light source, water splitting always will occur. As a result, additional potential may not be needed. Practically, a single junction (single band-gap) semiconductor does not have a satisfactory efficiency yet. In fact, inappropriate band-gap or non-matching band-edges can cause efficiency shortages in the single photo system configurations of either n-type or p-type arrangements. Additional voltage or bias is required to either increase the rate by reducing electron-hole recombination in the bulk semiconductor when using a wide band-gap semiconductor or, if it is not energetic enough, when the band-edges do not overlap the water splitting potential. There are a number of methods to prepare a biased reactor; electrical bias (grid) (Figure 2-4),

chemical bias pH (Figure 2-5), PV or dye sensitized solar cell (DSSC) bias (Figure 2-6) and internal bias (Figure 2-7). Biasing the photoelectrochemical water splitting system with electricity is not a desirable option. This is due to the fact that the electricity normally comes from burning fossil fuel, which produces greenhouse gases.

In a chemically biased system, two different electrolytes with different pH levels normally are used. Acid and alkaline electrolytes can be used in either of the sides. These electrolytes are separated by a proton exchange membrane. The difference in pH between the cathode and anode chambers results in production of energy that is essential for the photoelectrochemical water splitting system. However, this method of biasing is not suitable because the bias will progressively reduce the effectiveness of the system due to consumption of acid and alkaline in the chambers. Also, in pH biased reactors, Nafion membranes can be utilized in order to separate gases (O_2 and H_2); however, the Nafion membrane is not suitable for use in an electrolyte that contains cation (eg. Na^+) as this will replace the H^+ in the membrane and therefore limit the movement of H^+ across it. Hence, less H^+ ions are available to be reduced to H_2 at the cathode.

As can be seen in Figure 2-6, another method of biasing a photoelectrochemical water splitting system is to convert solar radiation to electricity via a photovoltaic cell and to transfer this electricity to the system to perform water electrolysis [32, 33]. The dye-sensitized solar cell (DSSC) is a new generation of solar cells. In this system a DSSC is used to capture sunlight and convert it to current, which then flows to the PEC cell where water splitting occurs [34]. Internal biasing (Figure 2-7) is produced by layering of the photoelectrode with different semiconductor thin films. This method is named as “layered”, “stacked” or “hybrid”.

There are numerous possibilities of combinations to achieve the appropriate band-gap and band-edges for direct water splitting techniques by internal biasing. The only drawback of this system is the complexity of the process [35]. A layered arrangement is essential due to the fact that all of the band-edges of semiconductors should match and be related to the band-edges of water [36].

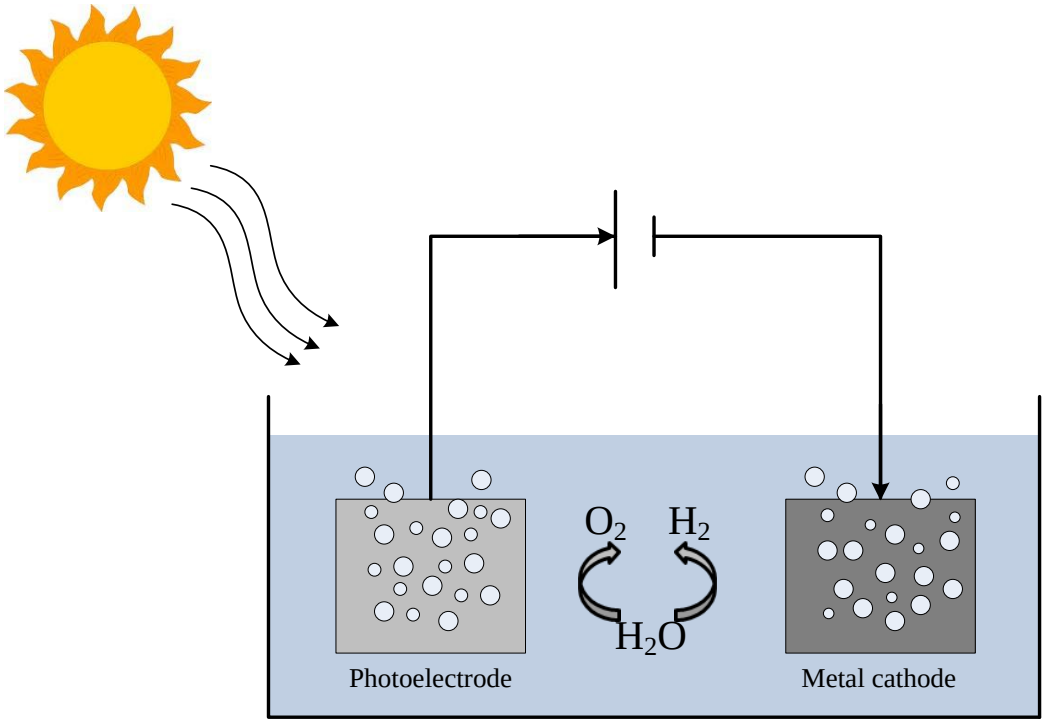

Figure 2-4 Structure of the grid-biased photoelectrochemical cell

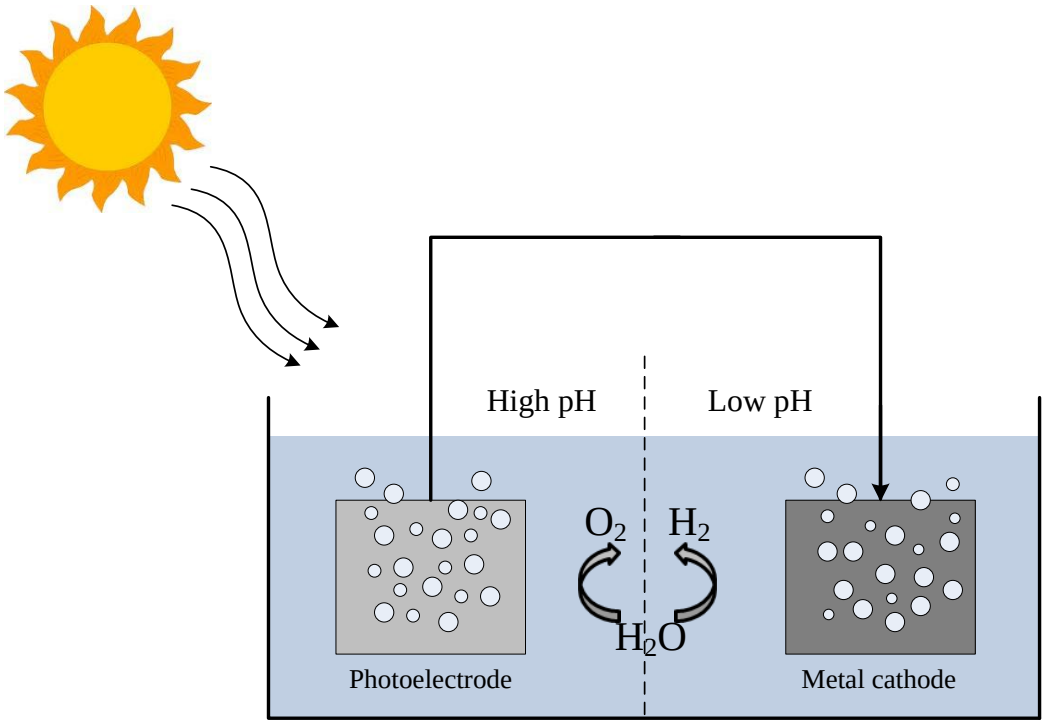

Figure 2-5 Structure of the chemical-biased photoelectrochemical cell

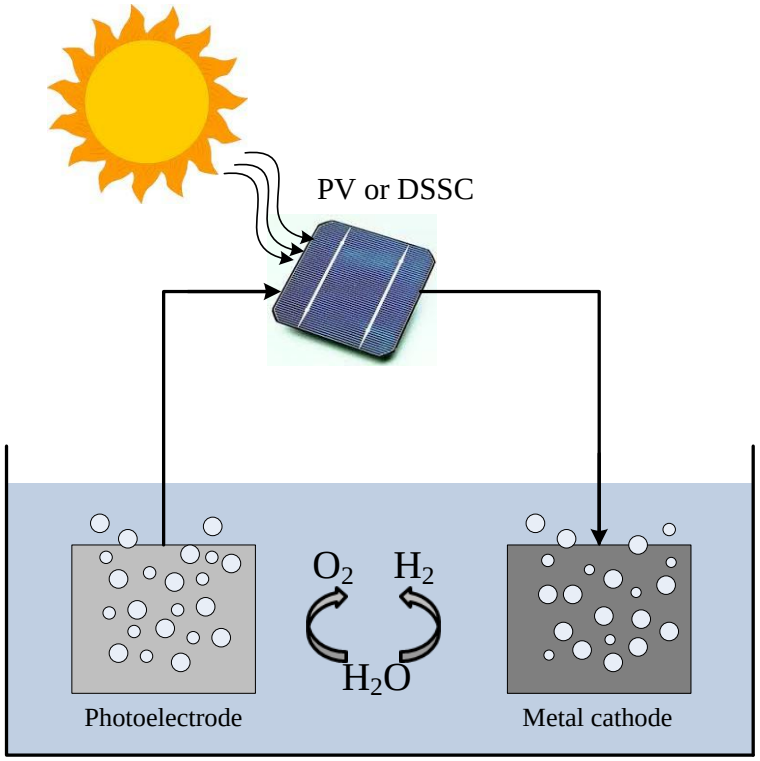

Figure 2-6 Structure of the PV- or DSSC-biased photoelectrochemical cell

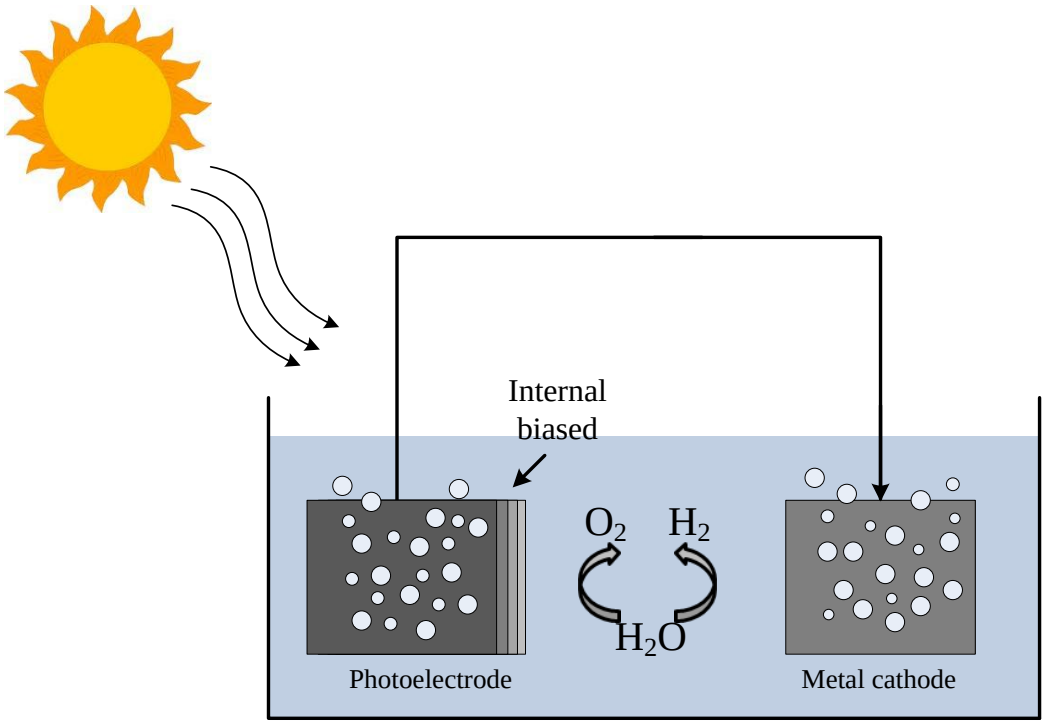

Figure 2-7 Structure of the internally biased photoelectrochemical cell

2.2. Influence of surfactants

Semiconductors have been of significant interest due to their extraordinary electrical, magnetic, optical and mechanical properties [37]. Having these suitable properties, semiconductors have been found to be useful in a wide variety of industrial areas such as electronics, catalysis and ceramics, and for magnetic and structural components [38]. One of the most interesting applications of these materials is photocatalytic hydrogen production. A clean and renewable source of energy (hydrogen fuel) can be developed by utilizing abundant solar radiation via photocatalytic splitting of water into hydrogen and oxygen. In order to produce a great amount of hydrogen fuel, photoelectrodes' semiconductors need to be of high efficiency and stability. In fact, a target efficiency of 10% is required to achieve commercialized production of hydrogen fuel [24]. However, the efficiency and stability of photocatalytic semiconductors have not yet reached a level for commercial applications [18].

Stable photoelectrodes made from metal oxide have shown low efficiency [34]. In contrast, multi-junction conventional semiconductor photoelectrodes have a high efficiency (slightly above 10%) [39, 40] but low stability, degrading within a short time. The type of photoelectrode, as well as the electrolytes used and other experimental conditions are important factors that can affect the efficiency and stability of semiconductors [8]. Various semiconductive metal oxides have been used widely as photoanodes with such photocatalytic properties [41] as band-gap, flat band potential, over potential and stability against corrosion [42]. More recently, multi-junction electrodes have been investigated to improve the stability and efficiency of photoelectrodes [43-45]. However, despite numerous efforts, the efficiency and stability of semiconductors are far from the level required for commercialization. Consequently, metal oxide nanostructures have been used to improve photoelectrochemical performance [46, 47]. These nanostructures have a large surface area, which provides a direct pathway for electrons to transfer [48]. Metal oxide nanostructures can be prepared by sputtering, electro-spinning, chemical vapour deposition or a sol-gel process [49]. Among these methods, sol-gel technology for deposition of a thin nanostructure has gained impetus in the last decade, owing to the low capital cost and its adaptability for

large area deposition [50, 51]. The sol-gel process often employs surfactants to enhance the quality of the nanostructures [52, 53].

Surfactants are well-established materials capable of controlling the characterized size (e.g. crystallite, grain or particle size) of semiconductors by preventing agglomeration and enhancing the quality of the nanostructures [54]. Basically, surfactants are molecules with a polar hydrophilic head and a hydrophobic hydrocarbon chain tail [22]. Recently, surfactants have been taken into major consideration for particle size control by their adsorption onto the particles' surfaces, where one end of the surfactant chain is anchored to the particle surface and other end is free [23]. Surfactants play an important role in changing the inter-particle potential within the nanoparticles, hence changing their aggregation behaviour [55]. Therefore, different surfactants with different structures and head sizes may tune the inter-particle interactions to different extents and have different tendencies for controlling the size of nanoparticles. Calcination also is used to increase the stability of nanocrystalline materials [56]. Calcination can be varied by a colloidal template which depends on surfactant, solvent, concentration, calcination temperature and duration [57]. However, when the nanomaterials have reached a sufficient degree of condensation, the surfactant-based templates are no longer needed and can be removed to open the porous structure.

2.2.1. Surfactant classifications

Surfactants are organic compounds that contain hydrophobic and hydrophilic groups. Having this property will result in having both water insoluble and water soluble components. Surfactants normally adsorb at the interface between air and water or, in the case of mixing with oil, they will adsorb at the interface between oil and water. The insoluble hydrophobic group may extend out of the bulk water phase, into the air or into the oil phase, while the water soluble head group remains in the water phase. This alignment of surfactants at the surface modifies the surface properties of water at the water/air or water/oil interface.

Surfactants also are known to be interesting materials for controlling the grain size of metal oxides. Furthermore, surfactants are necessary in sol-gel processes, to prevent

agglomeration and enhance the quality of the nanostructures [52, 53]. The surface area of a metal oxide semiconductor is a key factor in the efficiency of a photoelectrochemical water splitting cell. Increasing the surface area of metal oxide particles with controlled grain size can increase the photoactivity of these particles. However, charge recombination could occur due to the increase in surface defects. Consequently, the optimization of these two key factors is needed to produce the most suitable grain size and improve the efficiency.

All surfactants are categorized in three different groups: cationic, anionic and non-ionic surfactants.

2.2.1.1. Cationic surfactants

Any soap or detergent, in which the hydrophilic or water-loving end contains a positively-charged ion (cation), is called a cationic surfactant. Typical examples are cetyltrimethylammonium bromide (CTAB), octadecyltrimethylammonium bromide (OTAB) and tetradecyltrimethylammonium bromide (TTAB). Hydrophilic substances dissolve readily in water, and lipophilic substances dissolve in hydrocarbons, which are organic compounds containing a lot of carbon and hydrogen.

Cationic surfactants are almost all man-made, and their ionic portion is positively charged. They are good emulsifying agents too, and do not form insoluble scums with positively-charged hard-water ions. These surfactants also have been found to be good bactericides, and some find use as topical antiseptics. Their germicidal properties make them especially useful in bathroom and hand sanitizers. The usual job of these soaps or detergents is to make lipophilic substances (like oils, fats and greases) soluble in water, so that they can be washed away. Since water easily dissolves ionic substances or materials that contain one or more charged atoms, and hydrocarbons dissolve oils, fats and greases, a detergent molecule has a hydrocarbon end and an ionic end. The hydrocarbon end of the soap molecule dissolves in a particle of grease or oil, leaving the ionic end exposed to the water.

2.2.1.2. Anionic surfactants

An anionic surfactant is a macromolecule, usually in the sulphonate or sulphate group of chemicals such as sodium dodecyl sulfate (SDS), which acts as an active surface agent to lower the surface tension of liquids. This allows them to bind to impurities and particles that are suspended in the liquid, which makes them effective cleaning agents in water. In small concentrations, they also can cause the foaming of compounds in water by creating large numbers of small bubbles of gas, and this makes them effective in cosmetics such as shampoo and toothpaste, and in fire-suppressing agents.

Basic soap, used to clean the human body, also is a type of surfactant or detergent made from natural fatty acids of plant or animal origin. The difference with an anionic surfactant is that it is largely a synthetic chemical, and it has been designed to act not only as a surfactant that binds to oils and particulates in water, but also as a denaturing chemical for proteins. Since anionic surfactants break down proteins attached to clothing in water, they are not recommended for ordinary soap use, as human skin is also a type of protein.

2.2.1.3. Non-ionic surfactants

The non-ionic category of surfactants includes chemical structures that contain active molecules with no electrical charge. Unlike molecules with surface properties due to a positive (cationic) or negative (anionic) charge, non-ionic surfactants do not react with other ions. As a result, they do not form insoluble salts, can be used in strong acidic solutions and tend to have low toxicity profiles.

Non-ionics are found in everyday products used in households, including personal care items, cosmetic formulations and laundry and dish detergents, as well as in commercial scale industrial applications such as environmental protection, paper processing and thin films. Depending on the application, a non-ionic surfactant often will serve a specific purpose in the formulation. For instance, they are used as de-foaming aids in automatic dish washing, oil recovery agents in clean-up operations, and wetting and dispersing agents for soil and turf treatments. Some examples of non-ionic surfactants are polyethylene glycol and Triton surfactants.

2.2.2. Influence of surfactants on particle size

Extensive research studies have been carried out on tuning the crystallite sizes of Fe_2O_3 and WO_3 photocatalysts using cationic [58], anionic [59] and non-ionic [60] surfactants.

Since commencing exploration of Fe_2O_3 nanocatalysts as a photocatalyst, the small diffusion length of this material was reported as one of its drawbacks [61]. The reported diffusion length for Fe_2O_3 is between 2 – 4 nm [62]. So, the diameter of the nanocrystals would have to be decreased to 5 – 10 nm in order to prevent recombination of electron and holes [63]. The Teng group [64] have focused their study on the synthesis and characterization of Fe_2O_3 nanoparticles. Utilizing stearic acid as a surfactant, they have achieved production of monodisperse 3 nm Fe_2O_3 particles. Also, Bumajdad and his co-workers have utilized tetrabutylammonium hydroxide (TBAH) as a precipitant to modify the crystallite size of Fe_2O_3. They have achieved the preparation of a smooth and uniform surface with particles in a range of around 4 nm.

Tungsten trioxide has a diffusion length of ~150 nm [65]. Therefore, an efficient WO_3 photocatalyst might have a crystalline size of less than 150 nm [8]. Asim's group [66] have synthesized WO_3 nanoparticles sized between 10–50 nm by utilizing sucrose ester microemulsion as a biodegradable agent. Further, they have reduced the particle size to 3-15 nm by using the cationic surfactant cetyltrimethylammonium bromide (CTAB) as a structure-directing agent [58]. Deepa and co-workers [67] have focused on preparation of WO_3 nanoparticles treated with an anionic surfactant, sodium dodecyl sulfate (SDS). They have controlled the crystal growth by optimizing the surfactant content in the precursor solution. Lai et al. [68] also reported the influence of the concentration of L62 and P123 copolymers as non-ionic surfactants on the surface area of WO_3 nanoparticles.

Therefore, the characterized sizes (particle size, grain size and crystallite size) of Fe_2O_3 and WO_3 nanoparticles are vigorously dependent on the type of surfactant and surfactant size (either head or tail). However, the relationship between surfactant structure and synthesized photocatalyst is not well known. This correlation could be confirmed based on (A) adsorption density of surfactants and (B) vacant space between the surfactants.

2.2.2.1. Adsorption density of surfactants

The existing model (equation 2-2) can be used to describe the growth of individual crystals of average particle diameter, *D*, dispersed in a homogeneous matrix [69]:

$$D = D_0 + k\, t^{1/n} \tag{2-2}$$

Where D is the particle size, D_0 is the critical particle size, t is time, k and n are constant.

The value of *n* is dependent on the type of crystal growth [70-72]. If *n* is equal to 2, it is inferred that crystal growth is controlled by the diffusion of ions along the matrix-particle boundary; when *n* = 3, the growth is controlled by the volume diffusion of ions in the matrix; and when *n* = 4, it is deduced that growth is controlled by dissolution kinetics at the particle–matrix interface. Since, in this study, the crystal growth is controlled by the diffusion of ions along the matrix-particle boundary, we can set *n* as 2. Equation 2-2 is a general equation for calculating particle size of nanoparticles; however, with the presence of surfactants, crystals cannot grow infinitely. Thus, equation 2-3 can be used instead. In this equation *t* would be equal to t_{eff} (effective time) which is dependent upon surfactant type.

$$D = D_0 + k\, t_{eff}^{1/2} \tag{2-3}$$

2.2.2.2. Vacant space between the surfactants

In this study, we have named the distance between each pair of surfactants as vacant space or coverage factor (C_p).

% coverage = C_p

With increasing molecular weight of surfactants, vacant space (C_p) decreases. Utilizing equation (2-3) and applying C_p to the equation, particle size of nanoparticles would be calculated as:

$$D = D_0 + k\, C_p\, t_{eff}^{1/2} \tag{2-4}$$

2.3. Semiconductors

A semiconductor is a material which has a degree of electrical conductivity between that of a metal (such as copper) and that of an insulator (such as glass). Semiconductors are the foundation of modern solid state electronics, including transistors, solar cells, light emitting diodes (LEDs), quantum dots and digital and analogue integrated circuits. A semiconductor may have a number of unique properties, one of which is the ability to change its conductivity by the addition of impurities ("doping") or by interaction with another phenomenon, such as an electric field or light; this ability makes a semiconductor very useful for constructing a device that can amplify, switch or convert an energy input. The modern understanding of the properties of a semiconductor relies on quantum physics to explain the movement of electrons inside a lattice of atoms.

In a semiconductor, the valence band is the highest energy band that is fully occupied by electrons at 0 K, with its upper edge labelled E_v. The next energy band above the valence band is referred to as the conduction band, with its lower edge labelled E_c. The energy gap between the valence band and the conduction band is known as the band-gap, E_g. Electrons in the valence band are bound to the atoms in the solid and cannot conduct unless they are excited to the conduction band. Electrons promoted to the conduction band leave behind empty states in the valence band, not occupied by electrons, which are known as holes. These act essentially as positive charges. In conducting materials, such as metals, the valence and conduction bands overlap.

Insulating materials have a very large band-gap, too large for any valence electrons to be thermally excited into the conduction band. Semiconductors have a small band-gap from 0.2 to 3.5 eV that allows thermal and optical excitations of valence band electrons into the conduction band [73].

In the case of direct band-gap semiconductors, the bottom of the conduction band and the top of the valance band occur at the same position in wave vector momentum k space, $k = 0$. The absorption of a photon with an energy greater than or equal to the band-gap energy will generate an electron-hole pair. The electron is excited to the conduction band, leaving a hole in the valence band. This is known as the direct or optical transition. In indirect band-gap semiconductors, the bottom of the conduction

band is shifted in k space and no longer matches up with the top of the valence band. The indirect transition involves both a photon, to excite an electron to the conduction band energy level, and a phonon (lattice vibration), to move the electron across k space. Schematic diagrams of the direct and indirect processes are shown in Figure 2-8.

All real crystal lattices deviate from ideal atomic structures and possess defects which influence various physical properties of the material, including its electrical conductivity. Intrinsic semiconductors (such as very high-purity Si) have a negligible number of impurities, while extrinsic semiconductors have impurities that "donate" electrons to the conduction band, or "accept" electrons from the valence band. Usually, intrinsic semiconductors are "doped" with foreign impurities to produce an extrinsic semiconductor. Donor or acceptor energy levels are formed just below the conduction band-edge or just above the valence band-edge, respectively [74].

Donor impurities result in n-type conductivity, where conduction is dominated by electrons: the negative charge carriers. Alternatively, acceptor impurities result in p-type conductivity, where conduction is dominated by holes: the positive charge carriers. In the case of an n-type semiconductor, such as α-Fe_2O_3, the dominant charge carriers (electrons) are known as majority carriers and the holes as minority carriers.

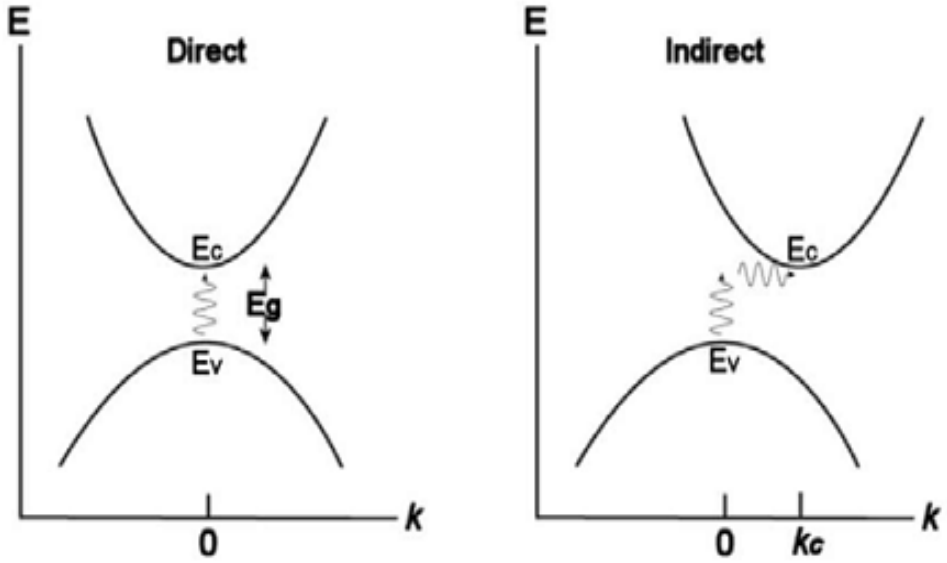

Figure 2-8 Schematic diagrams of the direct and indirect band-gap transition processes, where E is energy and k is the wave vector (Obtained from [73])

In the case of an intrinsic semiconductor, thermal excitation of electrons from the valence band to the conduction band occurs, leaving behind an equal number of holes as electrons, $n = p = n_i$ (intrinsic carrier density).

Metal oxide semiconductors are generally of much lower purity than traditional semiconductors, such as Si and Ge, and often possess lattice defects (such as vacancies and interstitials) that act as donors or acceptors. Ionic defects such as vacancies and interstitials are known as point defects. Electronic defects, such as extra electrons from dopants and polarons (electron and local lattice distortion created by the charge carrier), are electrically active and can introduce charge carriers into mid band-gap energy levels [75].

Metal oxide semiconductors cannot be thought of as intrinsic semiconductors. However, as the intrinsic carrier density is highly temperature-dependent, there exists a high temperature range where the concentration of intrinsic charge carriers exceeds that of the extrinsic carriers, so the electrical properties of the semiconductor are independent of the impurities within the material, and the semiconductor exhibits intrinsic behaviour [76]. At lower temperatures, the conductivity is dominated by impurity conduction mechanisms resulting from the largely temperature-independent extrinsic defects.

For oxides such as hematite, that have transition metal ions with incompletely filled 3d shells, conduction can be achieved through the introduction of vacancies or impurity ions into the lattice. The deviation in valency as a result of the introduction of a dopant (either point defects or foreign ions) is compensated by a neighbouring parent metal ion. The metal ion that has undergone a valency change as a result of the dopant (to retain charge neutrality) is referred to as a donor centre, or more specifically as a majority centre or a minority centre, depending on valence change.

The Fermi function (equation 2-5) describes the probability $f(E - E_F)$ that a given available energy state will be occupied at a given temperature T (K), where E is the energy, E_F is the Fermi level and k is Boltzmann's constant.

$$f(E-E_F)=\left[1+\exp(\frac{E-E_F}{KT})\right]^{-1} \quad (2\text{-}5)$$

The Fermi level is the energy at which the probability of an energy level being occupied by an electron equals one half. The Fermi level also can be defined as the electrochemical potential of the electron in a material [77].

In semiconductors, the Fermi level is within the band-gap. For intrinsic semiconductors E_F is around the midpoint between E_c and E_v. In the case of an n-type semiconductor, E_F is shifted towards E_c and is often between the donor level and the conduction band. An electronic band structure (for the case of n-type Ti-doped hematite) is shown in Figure 2-9. The impurity ions produce a donor level E_D just below the empty conduction band. The Fermi energy has been shifted towards the conduction band-edge.

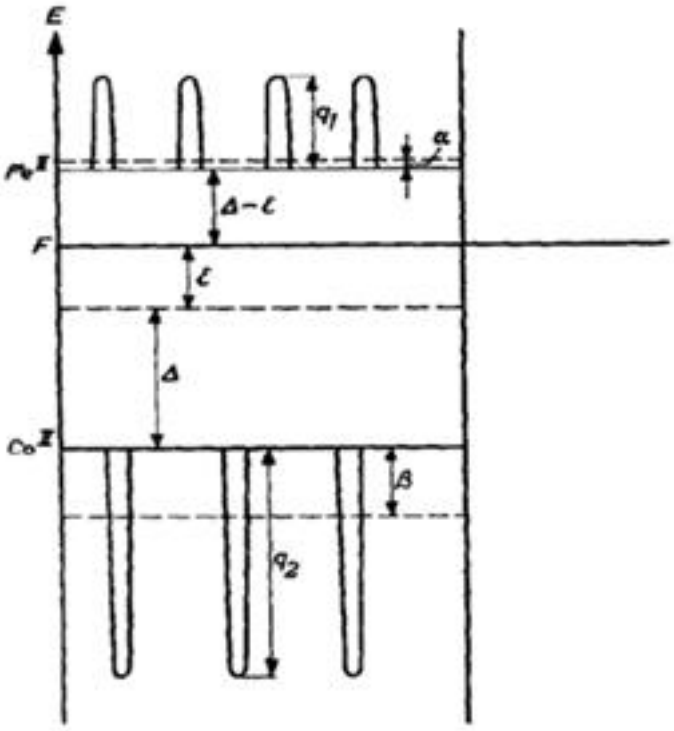

Figure 2-9 Electronic energy diagram of doped, n-type α-Fe_2O_3, showing localized energy levels (Obtained from [78])

2.4. Material aspects of photoelectrochemical cells

The materials required for the photoelectrodes of PECs should perform two fundamental functions:

- Optical function required to obtain maximal absorption of solar energy;
- Catalytic function required for water decomposition.

Most PEC photoelectrodes that exhibit sustainable performance are fabricated from oxide materials [17, 79], although the application of valence semiconductors, such as GaAs, has been studied as well [80].

Metal oxide semiconductors are categorized as a conventional photovoltaic material and metal oxides. The semiconductor can be n-type, p-type, or a coupling of n-type and p-type. There have been many reports of highly efficient n-type semiconductor photoanodes. However, there have been relatively few reports on highly efficient p-type semiconductor photocathodes. Also, single-crystal phosphides such as InP and $GaInP_2$ have been reported to be efficient photocathodes [81]. However, an efficient polycrystalline photocathode material is highly desirable for large-scale applications of PEC water splitting [82]. Therefore, we have selected two different n-type semiconductors (Fe_2O_3 and WO_3) for this study.

The properties of photoelectrodes should satisfy several specific requirements in terms of semiconducting and electrochemical properties, including [83]:

- Band-gap
- Flat band potential
- Schottky barrier
- Electrical resistance
- Helmholtz potential
- Corrosion resistance
- Microstructure

Consequently, the development of high efficiency photoelectrodes that satisfy all of these requirements entails processing of the materials in order to achieve optimized properties in terms of performance characteristics, including:

- High efficiency
- Durability
- Low cost of manufacturing
- Low cost and ease of maintenance

These properties and performance characteristics will be achieved principally through the imposition of bulk vs. interface properties in a controlled manner. This challenging requirement can be met through the development of new processing technologies that address this issue, and characterization techniques that allow the determination of the electrochemical properties of interfaces.

It has been documented that interfaces have a substantial impact on functional properties. For example, grain boundaries may act as weak links for charge transport in polycrystalline materials.

2.4.1. Photocatalytic activity of Iron oxide (Fe_2O_3)

Fe_2O_3 is known as an n-type semi-conductive oxide with a band-gap of 2.2 eV and a flat band potential of 0.32 V, which results in high theoretical efficiency of 12.9% [84]. Its absorption of the solar spectrum is in the range of 295-600 nm, which comprises 38% of the photons within the solar spectrum [85]. Although hematite possesses many favourable characteristics, the reported water splitting efficiencies in the literature for α-Fe_2O_3 are very low [32] due to its low charge carrier mobility, small hole diffusion length (2-4 nm < light penetration depth 118 nm at $\lambda = 550$ nm), fast recombination [86] and unfavourable band-edge positions [87]. Another drawback of hematite is its considerable interface state recombination issue that leads, in practice, to very low solar light-to-current conversion efficiencies and large over-potential for O_2 evolution. Despites of all the advantages/disadvantages mentioned above, n-type Fe_2O_3 semiconductor was selected in this study due to its ideal band-gap for solar water

splitting as well as abundance in the Earth's crust and its stability under harsh chemical conditions.

Various strategies have been employed to address these issues, for example, doping of the material to adjust the carrier mobility, incorporation of co-catalysts which reduce the over-potential, surface passivation to minimize losses by carrier recombination at the semiconductor–electrolyte interface and, as a key remedy, nanostructuring to meet the requirements of optimum solar light absorption length (several 100 nm) but short diffusion length [88].

The Aroutiounian group [89] conducted an experiment to test the photoelectrochemical activity of a tin-doped iron oxide photoelectrode. They synthesized and characterized n-type Fe_2O_3 with up to 2 at.% Sn-doping. They produced a photoanode with very good photoresponse to the visible region of solar irradiation. Also, by increasing Sn doping, the band-gap of the semiconductor was increased. In terms of efficiency, the sample with 0.75 at. % Sn-doping has shown the highest incident photon-to-current efficiency values.

However, in 2008, the Souza group [90] used Si-doped iron oxide to modify the photocatalytic activity of hematite. They also have presented a controlled thickness deposition method to obtain thin α-Fe_2O_3 in the range of 130 – 200 nm using spin-coating. The highest photocurrent response was obtained for the 0.5% Si-doped hematite film. Moreover, the results showed that the introduction of Si affected the grain growth, leading to a mesoporous structure. The Si-doped hematite exhibited higher photocurrent response when compared with undoped films.

Afterwards, in 2010, Saroj Kumari and his colleagues [91] used Ti^{4+} as a dopant to modify and enhance the Fe_2O_3 photoanode for hydrogen production in water splitting applications. Conducting the experiment, they found that increasing doping concentration led to an increase in the porosity of Fe_2O_3 thin film. Also, a significant decrease in the band-gap of Fe_2O_3 was found to be due to doping. The optimal doping concentration of Ti^{4+} in hematite was 0.02 M, at which level photocurrent density as well as solar-to-hydrogen conversion efficiency were maximised.

At the same time in 2010, Praveen Kumar's research group [92] investigated the effect of zirconium as a dopant in α-Fe_2O_3 thin film for photoelectrochemical water splitting applications. After performing photoelectrochemical measurements, the 2.0 at% Zr^{4+} doped α-Fe_2O_3 sample showed the highest photocurrent density as well as solar-to-hydrogen conversion efficiency. The improved performance of the Zr^{4+} doped α-Fe_2O_3 sample would be due to its improved conductivity through the substitution of Fe^{3+} by Zr^{4+} in the α-Fe_2O_3 lattice and the resultant higher value of flatband potential.

A year later, in 2011, a research project was conducted within Liu's group [93] in which they utilized Ni as a dopant for synthesisation of Fe_2O_3. Afterwards, the prepared sample was characterized and the photoelectrochemical activity was tested. The sample with 2.08 mol. % Ni showed the highest photocatalytic activity. Its high performance was attributed to the improvement of charge transport properties and retardation of the charge recombination resulting from the dopants in the lattice.

Ti-doped α-Fe_2O_3 thin films were prepared within Lian's research group [94]. After conducting the photoelectrochemical test, they realized that doped hematite was much more efficient than the undoped sample. Titanium in the lattice can positively affect the photoelectrochemical performance by increasing the conductivity of the thin film. So, the excited electrons and holes can live longer, rather than rapidly recombining with each other as undoped hematite.

In 2012, hematite nanorod arrays, modified by surface doping of chromium (III) ions (Cr^{3+}), were produced by Shen et al. [95] for hydrogen evaluation via the photoelectrochemical water splitting method. The photoelectrochemical performances of Cr-doped α-Fe_2O_3 nanorod films depended on Cr-doping content, with an optimal Cr dopant content of 1.47 wt. %. Examination of the relationship between photoluminescence intensity and Cr content suggests that the enhanced PEC performance for Cr-doped α-Fe_2O_3 nanorod films with low Cr contents can be attributed to reduced photo-induced charge recombination, which correlates photoelectrochemical performances with charge transfer in the photoelectrodes modified by surface ion doping. At low concentrations, the Cr dopants act as electron (or hole) traps to retard

charge recombination, whereas at high concentrations Cr dopants act as charge recombination sites.

In 2013, Lee's group [96] investigated the effect of Si-doping on Fe_2O_3 nanotubular layers for photoelectrochemical water splitting applications. The results highlighted the clear improvement in photocurrent density of the 5 at. % Si-doped Fe_2O_3 in comparison with the undoped sample.

In order to enhance the photocatalytic activity of a Fe_2O_3 photoanode, Frites' group have undertaken a research project [97]. By incorporating flame oxidation of iron metal sheeting, they have produced Fe_2O_3 in nanowire form to minimize the effect of its high resistivity by reducing the transport distance of the photogenerated carriers to species in solution (OH^-, H_2O). Moreover, they have modified the optical and electrical behaviour of Fe_2O_3 by incorporation of carbon in its lattice. Carbon-modified iron (III) oxide (CM-n-Fe_2O_3), synthesized by flame oxidation of iron metal sheeting, generated a much higher photoconversion efficiency when compared to undoped n-Fe_2O_3 (maximum photocurrent density of 3.0 mA cm^{-2} at 0.1 V/SCE, maximum photoconversion efficiency of 2.3% at 0.5 V) and also compared to those made by spray pyrolysis or by silicon doping.

Bak et al. [98], also conducted research to investigate the effects of Cd on the photoelectrochemical activity of hematite. They have synthesized and characterized cadmium (II)-incorporated hematite (Cd-Fe_2O_3) films with varying at. % of Cd(II) (0-32%). They reported that Cd deposition enhances the photocurrent generation, as compared to bare hematite. Such enhancement was highest with a Cd content of around 0.4 at. % (maximum photocurrent density of 2.5 mA cm^{-2} at 0.8 V/SCE). Such enhancement most likely results from the mixed effects of a shift of the flat band potential, a change in band-gap energy and an increase in conductivity. They also reported that the incorporated Cd most likely exists as CdO, which increases the conductivity of hematite.

Table 2-2 Comparison of effects of different dopants on Fe_2O_3 thin film

Ref.	Dopant	Deposition method	Potential (V)	Photocurrent density ($mAcm^{-2}$)	Band-gap (eV)	Electrolyte	Thickness (nm)	Morphology
[89]	0.75 at.% Sn	Electro-deposition	0.80	1.00	2.12	1 M NaOH	-	-
[90]	0.50 at.% Si	Spin-coating	1.60	0.15	2.05	1 M NaOH	200	Grain width reduced
[91]	0.02 M Ti^{4+}	Spray-pyrolysis	0.50	1.98	1.54	1 M NaOH	-	Porous granular
[92]	2.00 at.% Zr^{4+}	Electro-deposition	0.60	2.10	2.08	1 M NaOH	920	Grain width reduced
[93]	2.08 mol % Ni	Electro-deposition	0.65	1.50	2.01	1 M NaOH	500	Porous granular
[94]	3.54 mol % Ti	Spin-coating	0.60	0.14	2.10	1 M NaOH	-	Worm-like
[95]	1.47 wt % Cr	Spin-coating	1.23	0.05	2.10	0.5 M Na_2SO_4	500	Nanorod arrays
[96]	5.00 at.% Si	Anodization	1.60	1.50	2.10	1 M KOH	600	Nanotubular
[97]	-	Electro-deposition	0.10	1.46	-	5 M KOH	-	Nanowire
	Carbon modified			3.00				Nanocrystal
[98]	0.4 at.% Cd	Electro-deposition	0.80	2.50	2.25	1 M NaOH	1800	Porous granular

2.4.2. Photocatalytic activity of Tungsten trioxide (WO_3)

Tungsten trioxide (WO_3) has been considered as one of the favoured photocatalytic materials for its usage as a photoanode in photoelectrochemical (PEC) splitting of water into hydrogen and oxygen, due to its stability in acid, resilience to photocorrosion effects, good transport properties, wide band-gap of 2.7 eV (300 – 360 nm ultraviolet and blue regions) and suitable flat band potentials of 0.4 V as an n-type semi-conductive oxide which can generate sizable photocurrents [99, 100]. The efficiency of WO_3, however, is still far from being economically viable [101]. WO_3 was selected as one of the metal oxide nanoparticle in this study owing a sensitive crystallite/grain size by varying the type of surfactant [102, 103].

The surface area of a WO_3 electrode is a key factor in the efficiency of a photoelectric cell. Increasing the surface area of WO_3 particles with controlled grain size can increase the photoactivity of these particles. However, charge recombination could be introduced by increasing the amount of surface defects. Consequently, the optimization of these two key factors is needed to discover the most suitable grain size and improve efficiency. Surfactants are well-known materials that can be useful for controlling the grain size of metal oxides. Also, surfactants are necessary in sol-gel processes to prevent agglomeration and enhance the quality of the nanostructures [51, 104, 105].

Extensive research studies have been carried out on the production of WO_3 layers using cationic [58], anionic [59] and non-ionic [60] surfactants. Asim's group [66] have synthesized WO_3 nanoparticles, sized 10 – 50 nm, by utilizing sucrose ester micro-emulsion as a biodegradable agent. Further, they have reduced the particle size to 3 - 15 nm by using cationic surfactant (CTAB) as a structure-directing agent [58]. Deepa and co-workers [67] have focused on the preparation of WO_3 nanoparticles treated with an anionic surfactant (SDS). They have controlled the crystal growth by optimizing the surfactant content in precursor solution. Lai et al. [68] also reported the influence of the concentration of L62 and P123 copolymers as non-ionic surfactants on the surface area of WO_3 nanoparticles.

In 2006, Marsen's group [106] investigated the photocatalytic behaviour of sputtered tungsten trioxide. Their reported results confirm that the grain size of WO_3 is influenced by the substrate temperature during the deposition process. Also, they reported that the sample grain size correlated with photocurrent performance (the larger the grain, the higher photocurrent density). Moreover, by doping WO_3 with nitrogen they tried to increase the photocurrent activity; however, their results showed that at low dopant concentration nitrogen-doped WO_3 films exhibit a photocurrent comparable to undoped films but with decreasing performance at higher dopant concentration.

With the aim of improving the performance and extending the range of applications of mesoporous WO_3 films, Solarska's group [107] have investigated the effects of a number of dopants (lithium, silicon, ruthenium, molybdenum and tin). Through substitutional cation doping, they have modified the particle size, porosity, crystallinity and transparency of the WO_3 films. Despite this finding, all doped electrodes showed a decrease in their photocurrent generation compared to pristine WO_3 film.

Li and his co-workers [108] synthesized and characterized WO_3 nanostructure using a polymeric precursor. They tried to investigate the effects of different calcination temperatures (350℃ – 550℃) on the photocatalytic activity of this photocatalyst. Their results highlighted that the WO_3 films were crystallized by sintering at over 400℃. Also, the photoelectrochemical test showed that the WO_3 electrode that was calcined at 450℃ exhibited the highest photocurrent density.

At the same time, Li and his colleagues [109] investigated the effect of citric acid (CA) on the microstructure and photoelectrochemical properties of WO_3 films. They also used polyethylene glycol (PEG) as a dispersing agent. They reported that, with increasing content of citric acid in the WO_3 precursor solution, the produced film experienced a larger particle size and rougher surface. Also, the sample with a mass ratio of CA/PEG at 0.6 displayed the highest photocatalytic activity.

Chen et al. [110] synthesized and characterized WO_3 nanoflake arrays (WNA) on tungsten sheets through a facile hydrothermal process. They also tested the photoelectrochemical activity of the thin film. Synthesized WNA exhibited superior

photo-electrochemical properties, indicated by its UV-vis absorption spectra and chopped current-potential.

In order to enhance the photocatalytic activity of tungsten trioxide, Biswas and his co-workers [111] synthesized and characterized the hierarchical tungsten trioxide via a straightforward, template free, hydrothermal route from ammonium metatungstate hydrate. They have reported that the hierarchical architecture-based photoanode produced higher photocurrent (two-fold high) than a nanoparticle-based photoanode. The enhanced activity can be attributed to improved charge-separation by superior charge transportation through the single-crystalline 1D building block.

Kim et al. [112] focused their study on synthesis of WO_3 thin film using two different methods (photoelectrochemical anodization (PA) and normal anodization (NA)) for water splitting hydrogen production purposes. They found that, by utilizing the PA method, the thickness of WO_3 could be extended to more than 2.6 μm, which is double the thickness that can be obtained by NA. Also, PA films showed very high photoelectrochemical activity, due to their thickness.

Kim and his co-workers [99] focused their study on the synthesis and characterization of mesoporous, transparent WO_3 thin film. They used polyethylene glycol (PEG) as a surfactant. By controlling the weight ratio of the tungsten precursor to PEG, they achieved the preparation of a sphere-like WO_3 nanoparticle film with high transparency. Also, the reported results illustrated that the sample with W:PEG ratio of 1:10 gave the highest photocurrent density among all the samples. Also, by applying methanol as a sacrificial reagent in the electrolyte, they succeeded in increasing the photocurrent density. This is due to the oxidation of methanol instead of water decomposition. This phenomenon can be referred to as photocurrent doubling, in which an additional electron is injected into the conduction band of the electrode during the photodecomposition of methanol.

Utilizing the sol-gel route from an aqueous precursor solution containing peroxopolytungstic acid (PPTA), Yang et al. [100] have prepared mesoporous tungsten trioxide films. They reported that the pH used for the preparation of PPTA solutions can

strongly influence the texture of WO_3 films. Also, they reported that the maximum photocurrent was achieved by pH adjustment to a value of 0.8. Moreover, the influence of porosity of WO_3 nanoparticles on photocurrent generation was clearly discussed (the higher the porosity, the higher the photocurrent density).

Table 2-3 Comparison of effects of different dopants on WO_3 thin films

Ref.	Experimental condition	Deposition method	Potential (V)	Photocurrent density ($mAcm^{-2}$)	Band-gap (eV)	Electrolyte	Thickness (nm)	Morphology
[106]	Undoped	Sputtering	1.60	2.70	-	0.33 M H_3PO_4	900	Rounded nodular
	Doped with 0.7 at.% N_2			2.90				
[107]	Undoped	Spin-coating	1.00	2.80	-	1 M H_2SO_4	2400	Mesoporous structure
	Doped with 5 at.% Si^{4+}			1.30				Smooth surface
	Doped with 5 at.% Li^+			0.25				Particle size growth
[108]	Calcined at 450 ℃	Dip-coating	1.40	2.70	2.92	0.5 M H_2SO_4	2900	Smooth surface
[109]	Mass ratio of CA/PEG = 0.6	Dip-coating	1.20	2.10	2.70	0.5 M H_2SO_4	2900	Rough surface
[110]	WO_3 nanoflake arrays	Hydrothermal process	1.50	2.35	2.60	0.1 M Na_2SO_4	3910	Smooth and uniform
[111]	Hierarchical WO_3	Hydrothermal process	1.60	1.87	-	0.5 M H_2SO_4	4000	Flower-like micro-patterns
[112]	Photoelectrochemical anodization	Anodization	1.50	1.85	-	0.33 M H_3PO_4	2600	Rough surface
[99]	W:PEG ratio of 1:10	Doctor-blading	1.20	2.20	2.50	1 M H_2SO_4	3530	Mesoporous structure
				3.70			6084	
				5.10		1M H_2SO_4 + CH_3OH		
[100]	pH = 0.8	Doctor-blading	1.50	1.40	2.60	1 M H_2SO_4	2800	Mesoporous structure
				4.10		1M H_2SO_4 + CH_3OH		

2.5. Gap in the knowledge

From the literature review, the following conclusions have been identified:

1. Surfactant plays an important role in the intermediate process, by determining the crystal growth during the calcination procedure.
2. The morphology of nanostructure materials, in turn, plays deterministic roles in the photoelectrochemical behavior.
3. The relationship between surfactant size (head and tail) and the synthesized nanoparticles is not known yet.
4. The effect of surfactants on modifying the PEC has not been fully explored.

This study explores the above influences by addressing the focus questions in chapter 1. Ultimately, the study quantifies an economical and routine pathway to improve the efficiency of PEC. Moreover, the method can be combined with, and complements, other methods, such as doping, mixing and multilayering, to achieve the most desirable properties.

3. METHODOLOGY

3.1. Introduction

This section describes the preparation techniques used to fabricate the electrodes and outlines the synthesis and characterization of the WO_3 and Fe_2O_3 thin films. Also, the instrumentation which has been used in this study to characterize different films will be discussed briefly.

3.2. Synthesis of electrodes

3.2.1. Substrate

The thin films were fabricated on top of fluorine-doped tin oxide (FTO) conducting glass substrates (Pilkington glass (USA), 10 Ω/sq). FTO, which is a transparent conducting film, acts as a window for light to pass through to the active material beneath (where carrier generation occurs). It is an ohmic contact for carrier transport out of the photovoltaic, and can also act as a transparent carrier for surface-mounted devices or those used between laminated glass or light transmissive composites. Transparent materials possess band-gaps with energies corresponding to wavelengths that are shorter than the visible range of 380 nm to 750 nm. As such, photons with energies below the band-gap level are not collected by these materials and, thus, visible light passes through. However, applications such as photovoltaics may require an even broader band-gap to avoid unwanted absorption of the solar spectra. The conducting glass cannot be heated above 550 °C as the conductivity of the FTO can be thermally degraded. However, the FTO is very chemically stable. The scanning electron microscope (SEM), cross sectional view and atomic force microscopy (AFM) images of FTO conductive glass are shown in Figure 3-1.

All the FTO glasses had to be washed sequentially with acetone, ethanol and acetone. The FTO glasses were separately immersed into the solvents and treated in an ultrasonic bath for 15 min for each wash. In the final stage, after washing, the FTO glasses were dried using nitrogen gas.

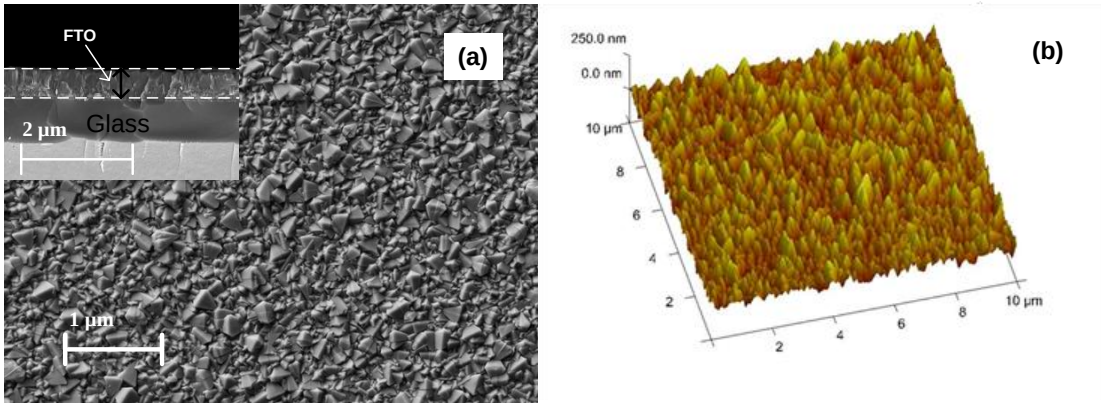

Figure 3-1 SEM (a) and AFM (b) images of FTO conductive glass

3.2.2. Working electrode

3.2.2.a. Fe_2O_3

Iron oxide is known as an n-type semiconductor and is one of the most suitable photoanodes for the purpose of water splitting hydrogen production. An iron oxide precursor solution can be produced according to the following recipe [8].

Iron nitrate (8.08 g) is dissolved in 20 ml ethanol under stirring for 30 minutes at 200 RPM speed, then 5 ml PEG and 2 drops Triton X-100 are added into the solution and stirred overnight at room temperature. Finally, it is placed under ultrasonic irradiation for 1 hour [8]. SEM and AFM images of calcined Fe_2O_3 nanoparticles are shown in Figure 3-2.

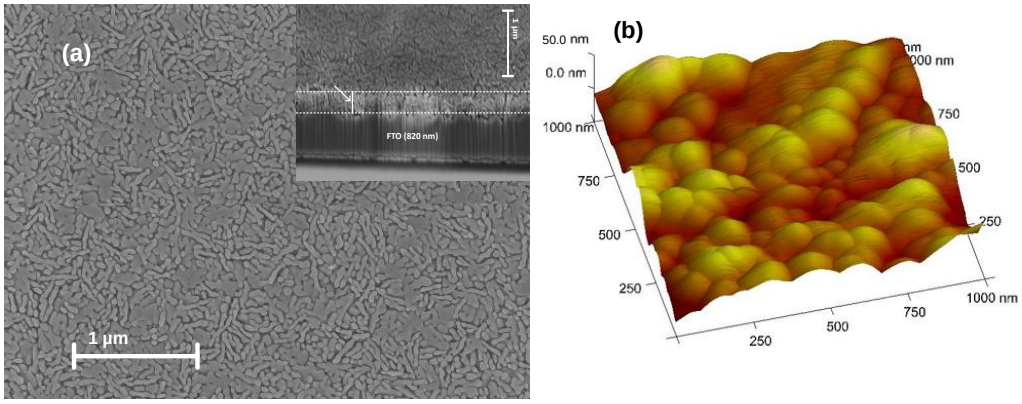

Figure 3-2 SEM (a) and AFM (b) images of Fe_2O_3 thin film

3.2.2.b. WO_3

Tungsten trioxide (WO_3), as an n-type semiconductor and owing to its relative narrow band-gap, is a promising material for many applications, such as water splitting, or for use in sensors, dye treatments, batteries and metal-inorganic frameworks,. However, both the efficiency and effectiveness of the WO_3 nanostructure must be improved to be practically useful in such applications. In this study, tungsten trioxide films have been prepared by the sol-gel method, using peroxotungstic acid (PTA) as the precursor sol. The preparation procedure for the tungsten trioxide nanoparticles was as follows [113]:

(1) 0.5 g of tungsten powder was dissolved in 15 mL of 30% (w/w) hydrogen peroxide aqueous solution, in a Pyrex container, to form peroxotungstic acid (PTA) and left for about 6 hours.

(2) The excess hydrogen peroxide was decomposed by adding 1 mg of platinum black.

(3) The solution was diluted to 0.1 M by adding approximately 10 mL of propan-2-ol.

SEM and AFM images of calcined WO_3 nanoparticles are shown in Figure 3-3.

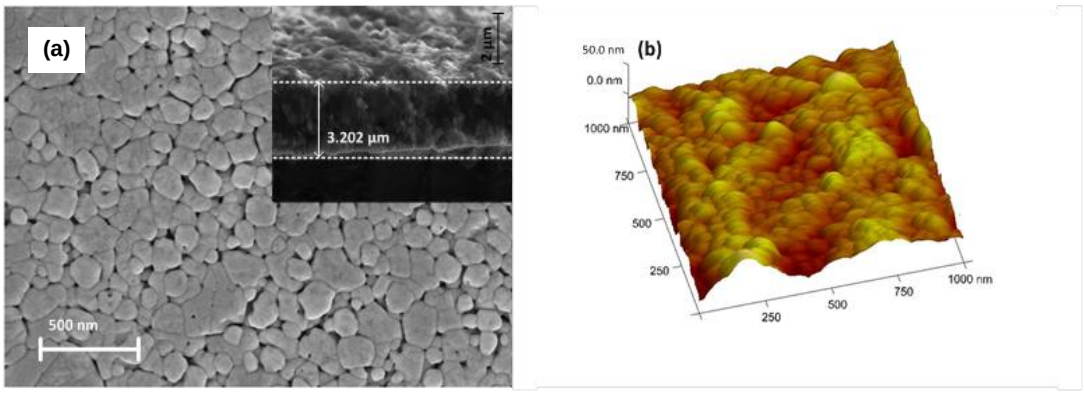

Figure 3-3 SEM (a) and AFM (b) images of WO_3 thin film

3.2.2.c. Sample preparation by different surfactants

Surfactants are well-known materials that can be useful in controlling the grain size of

metal oxides. Also, surfactants are necessary ingredients in sol-gel processes to prevent agglomeration and enhance the quality of the nanostructures. Therefore, in this study various surfactants, including cationic, anionic and non-ionic were trialled. The influences of these surfactants on particle size, morphology, surface roughness, crystalline structure and optical absorption were investigated. More importantly, by incorporating different surfactants we have aimed to improve and enhance the photoelectrochemical performance of these thin films.

3.2.3. Counter electrode

Platinum has continued to be at the forefront of interest as a cathode due to its superior H_2-evolving characteristics. For quantitative electrochemical analysis in laboratories, platinum electrodes of various types are used. Platinum is an excellent catalyst for H^+ reduction [114]. During this study, a coiled platinum counter electrode (Pt wire) has been used as the cathode (Figure 3-4).

Figure 3-4 The platinum counter electrode used in this study

This counter electrode design features a coiled platinum wire (99.99% pure) mounted at the end of a chemically-resistant epoxy rod. A fritted glass tube isolates the counter electrode from the main test solution. The glass tube is equipped with a Teflon adapter to enable mounting the tube in a 14/20 side port on the electrochemical cell.

Alternatively, the platinum rod may be removed from the glass tube and mounted directly in the electrochemical cell. The coil is fabricated from a platinum wire (0.5 mm OD) that is 29.0 (+/- 1.0) cm long. The approximate surface area of the platinum coil is 4.7 cm^2. The approximate diameter of the coil is 9 mm. The black epoxy rod (6.9 mm OD) is 150 mm long. The overall length of the rod and the coil is approximately 180 mm.

3.2.4. Reference electrode

A reference electrode is an electrode which has a stable and well-known electrode potential. The high stability of the electrode potential usually is attained by employing a redox system with constant (buffered or saturated) concentrations of each component of the redox reaction. There are many ways in which reference electrodes are used. The simplest is when the reference electrode is used as a half cell to build an electrochemical cell. This allows the potential of the other half cell to be determined. In a lab test situation for solar/photon-to-current conversion efficiency measurement, a reference electrode is used. This method is commonly referred to as the three electrodes cell. In this study we have utilized an Ag/AgCl reference electrode (Figure 3-5).

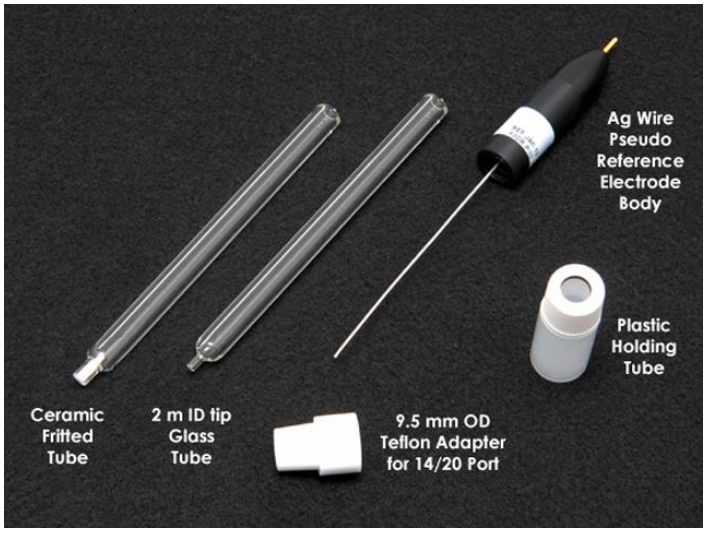

Figure 3-5 Schematic of Ag/AgCl reference electrode used in this study

3.3. Deposition technique

In this study, surfactant-treated Fe_2O_3 and WO_3 thin films were synthesized and deposited via sol-gel using both doctor blading and spin coating methods.

3.3.1. Doctor blading process

In this method, shown in Figure 3-6, a well-dispersed colloidal solution is dropped onto a substrate and spread with a glass rod to produce a thin film. Adhesive tape is usually used as a spacer to adjust the thickness of the film. The air-dried film is then sintered to improve its conductance and the adherence of particles onto the substrate.

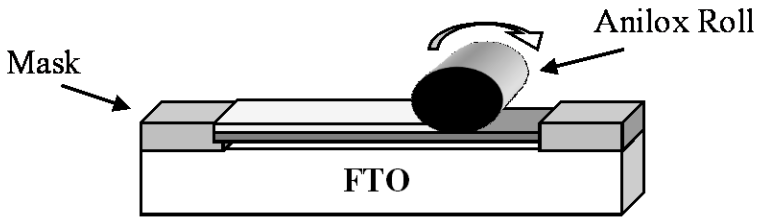

Figure 3-6 Schematic of doctor blading method

3.3.2. Spin coating process

Spin coating is a procedure used to apply uniform thin films to flat substrates. In short, an excess amount of a solution is placed on the substrate, which is then rotated at high speed in order to spread the fluid by centrifugal force. A machine used for spin coating is called a spin coater or, simply, a spinner. Rotation is continued while the fluid spins off the edges of the substrate, until the desired thickness of the film is achieved. The applied solvent is usually volatile, so simultaneously evaporates. The higher the angular speed of spinning, the thinner is the film. The thickness of the film also depends on the concentration of the solution and the type of solvent. Spin coating is widely used in micro-fabrication, where it can be employed to create thin films with thicknesses below 10 nm. It is used intensively in photolithography, to deposit layers of photoresist about 1 μm thick. Photoresist is typically spun at 20 to 80 RPS for 30 to 60 seconds. A schematic of the spin coating method is shown in Figure 3-7.

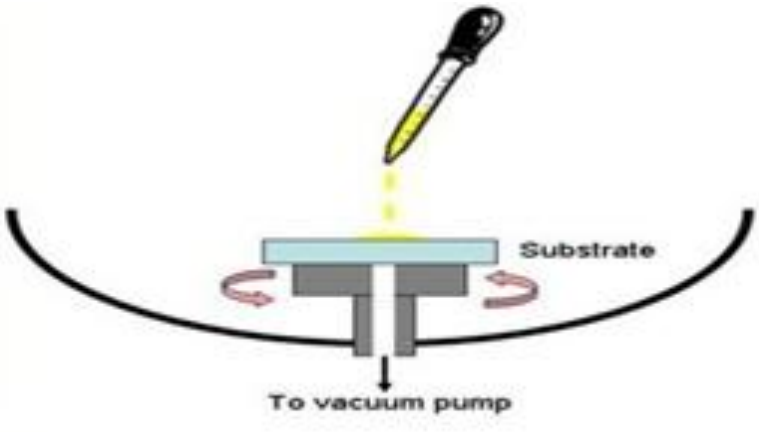

Figure 3-7 Schematic of spin coating method

3.4. Characterization techniques

In order to characterize samples, various techniques have been used. The characterization techniques used in this study are described in the following sub-sections.

3.4.1. Electron microscopy

A scanning electron microscope (SEM) is a type of microscope that produces images of a sample by scanning it with a focused beam of electrons. The electrons interact with atoms in the sample, producing various signals that can be detected and that contain information about the sample's surface topography and composition. The electron beam generally is scanned in a raster pattern, and the beam's position is combined with the detected signal to produce an image. SEM can achieve ultimate resolution of better than 1 nanometer. Specimens can be observed in high vacuum as well as in low vacuum. The most common mode of detection is by secondary electrons emitted by atoms that have been excited by the electron beam. The number of secondary electrons detected is a function of the angle between the surface and the beam. On a flat part of the surface, the plume of secondary electrons is mostly contained by the sample, but on a tilted part of the surface (such as an edge), the plume is partially exposed and more electrons are emitted. By scanning the sample and detecting the secondary electrons, an image displaying the topography of the surface is created. Field emission scanning electron microscopy (FESEM) was used in this study to investigate the surface morphology, and to obtain micrographs of grain and particle sizes, of different samples.

Focused ion beam SEM, also known as FIBSEM, is a technique used particularly in the semiconductor industry, materials science and, increasingly, in the biological field for site-specific analysis, deposition and ablation of materials. A FIBSEM is a scientific instrument that resembles a scanning electron microscope (SEM). However, while the SEM uses a focused beam of electrons to image the sample in the chamber, a FIB setup uses a focused beam of ions instead. FIB can also be incorporated into a system with both electron and ion beam columns, allowing the same feature to be investigated using either of the beams. FIB should not be confused with using a beam of focused ions for direct-write lithography (such as in proton beam writing), which is a quite different system where the material is modified by other mechanisms. For this study, FIB work was performed on all the samples, in order to investigate all film thicknesses, using the same instrument that was used for FESEM imaging, (Neon 40EsB FIBSEM, Carl Zeiss Pty Ltd, Germany).

Energy-dispersive X-ray spectroscopy (EDS) is an analytical technique used for the elemental analysis or chemical characterization of a sample. Its characterization capabilities are due in large part to the fundamental principle that each element has a unique atomic structure, leading to a unique set of peaks in its X-ray spectrum. To stimulate the emission of characteristic X-rays from a specimen, a high-energy beam of charged particles, such as electrons or protons, (or a beam of X-rays), is focused into the sample being studied. At rest, an atom within the sample contains ground state (or unexcited) electrons, within discrete energy levels or electron shells, bound to the nucleus. The incident beam may excite an electron in an inner shell, ejecting it from the shell while creating an electron hole where the electron used to be. An electron from an outer, higher-energy shell then fills the hole, and the difference in energy between the higher-energy shell and the lower energy shell may be released in the form of an X-ray. The number and energy of the X-rays emitted from a specimen can be measured by an energy-dispersive spectrometer. As the energy of such an X-ray is characteristic of the difference in energy between the two shells, and thus of the atomic structure of the element from which it was emitted, this allows the elemental composition of the specimen to be identified. EDS was employed during this study to identify and quantify elements present in a sample.

3.4.2. Atomic force microscope (AFM)

Atomic force microscopy (AFM) is a very high-resolution type of scanning probe microscopy, with demonstrated resolution of the order of fractions of a nanometer. The AFM consists of a cantilever with a sharp tip (probe) at its end, which is used to scan the specimen surface. The cantilever is typically silicon or silicon nitride, with a tip radius of curvature of the order of nanometers. When the tip is brought into proximity with a sample surface, force between the tip and the sample leads to a deflection of the cantilever according to Hooke`s law. Depending on the situation, forces that are measured in AFM include mechanical contact force and van der Waals forces. Along with force, additional quantities may simultaneously be measured through the use of specialized types of probe. Typically, the deflection is measured using a laser spot reflected from the top surface of the cantilever into an array of photodiodes. These cantilevers are fabricated with piezoresistive elements that act as a strain gauge. Using a Wheatstone bridge, strain in the AFM cantilever due to deflection can be measured, but this method is not as sensitive as laser deflection or interferometry. In this study, an atomic force microscope (Nanoscope (R) IIIa, Digital Instruments, Santa Barbara, CA) was used to determine the surface roughness and morphology of the thin films.

3.4.3. X-ray diffraction

X-ray crystallography is a method used for determining the atomic and molecular structure of a crystal, in which the crystalline atoms cause a beam of X-rays to diffract into specific directions. By measuring the angles and intensities of these diffracted beams, a crystallographer can produce a three-dimensional picture of the density of electrons within the crystal. From this electron density, the mean positions of the atoms in the crystal can be determined, as well as their chemical bonds, their disorder and various other characteristics. In an X-ray diffraction measurement, a crystal is mounted on a goniometer and gradually rotated while being bombarded with X-rays, producing a diffraction pattern of regularly spaced spots known as reflections. The two-dimensional images taken at different rotations are converted into a three-dimensional model of the density of electrons within the crystal, using the mathematical method of Fourier transforms, and are combined with the known chemical data for the sample. Poor

resolution (fuzziness) or even errors may result if the crystals are too small, or not uniform enough in their internal makeup and no useful data can be obtained from non-crystalline materials.

In this study X-ray diffraction (XRD) analyses were performed to find the structure of crystalline materials by exploiting the process of X-ray scattering from crystal planes. Crystallite size and phase identification were obtained using an X-ray powder diffractometer (D8 Advance, Bruker), with Cu Kα radiation (λ = 0.15418 nm). Diffraction peaks were recorded in the interval $20° \leq 2\theta \leq 60°$ at a scan rate of $0.01° \ s^{-1}$ to characterize all the film samples. The average crystallite size also was estimated from the Debye-Scherrer equation, equation 1:

$$D = \frac{0.94\lambda}{\beta} cos\theta \tag{3-1}$$

where D is the crystallite dimension, λ is the wavelength of the X-ray radiation (which is 0.15418 nm), θ is the diffraction angle, and β is the full width at half maximum.

3.4.4. Optical absorption

The optical properties (transmittance, absorption coefficient and optical band-gap energy) of thin films can be calculated from the variations in absorption density. In this study, the optical absorption was measured by a UV-visible spectrophotometer (JASCO, V- 670 spectrophotometer), which utilises absorption in the ultraviolet-visible spectral region. A blank FTO conductive glass sample was used as a reference and the absorption value was measured by calculating the area underneath the Uv-visible curve.

The band-gap of samples can be obtained from the absorption coefficient data, according to solid band theory:

$$(\alpha hv) = A\left(hv - E_g\right)^m \tag{3-2}$$

where α is the absorption coefficient, hv is the energy of the incident photon, A is a constant related to the effective mass of the electrons and holes, E_g represents the energy band-gap of samples and m = 2 for allowed indirect transition.

3.4.5. BET measurement

Brunauer–Emmett–Teller (BET) theory aims to explain the physical adsorption of gas molecules on a solid surface and serves as the basis for an important analysis technique for the measurement of the specific surface area of a material. The surface area of each sample was investigated by using this BET technique under N_2 constant adsorption at 77 K (Quantachrome, Autosorb-1). The grain size of each particle also can be calculated using equation 3:

$$d = \frac{6}{\rho\, S_g} \tag{3-3}$$

where ρ is the specific density of WO_3 (7.16 g/cm^3) and S_g is the BET surface area.

3.4.6. Photoelectrochemical measurement

Photoelectrochemical measurements were performed with linear polarization (I-V) techniques to evaluate the performance of the oxide film photoelectrodes. All photoelectrochemical measurements were carried out in a three electrode electrochemical cell containing 100 cm^3 of 0.5 M Na_2SO_4 electrolyte under illumination intensity of 100 mW cm^{-2} from a solar simulator. The sample's working electrode was fitted into a holder for illumination and testing of its photoelectrochemical reactions. A saturated Ag/AgCl electrode and a platinum wire were used as the reference and the auxiliary electrode, respectively. Linear scan voltammetry measurements were carried out using a Radiometer potentiostat (Versastat 4, Princeton Applied Research). The visible illumination was provided by the assembly of a 450 W Xenon arc lamp light source and focusing lenses. A schematic diagram of the photoelectrochemical measurement setup is shown in Figure 3-8.

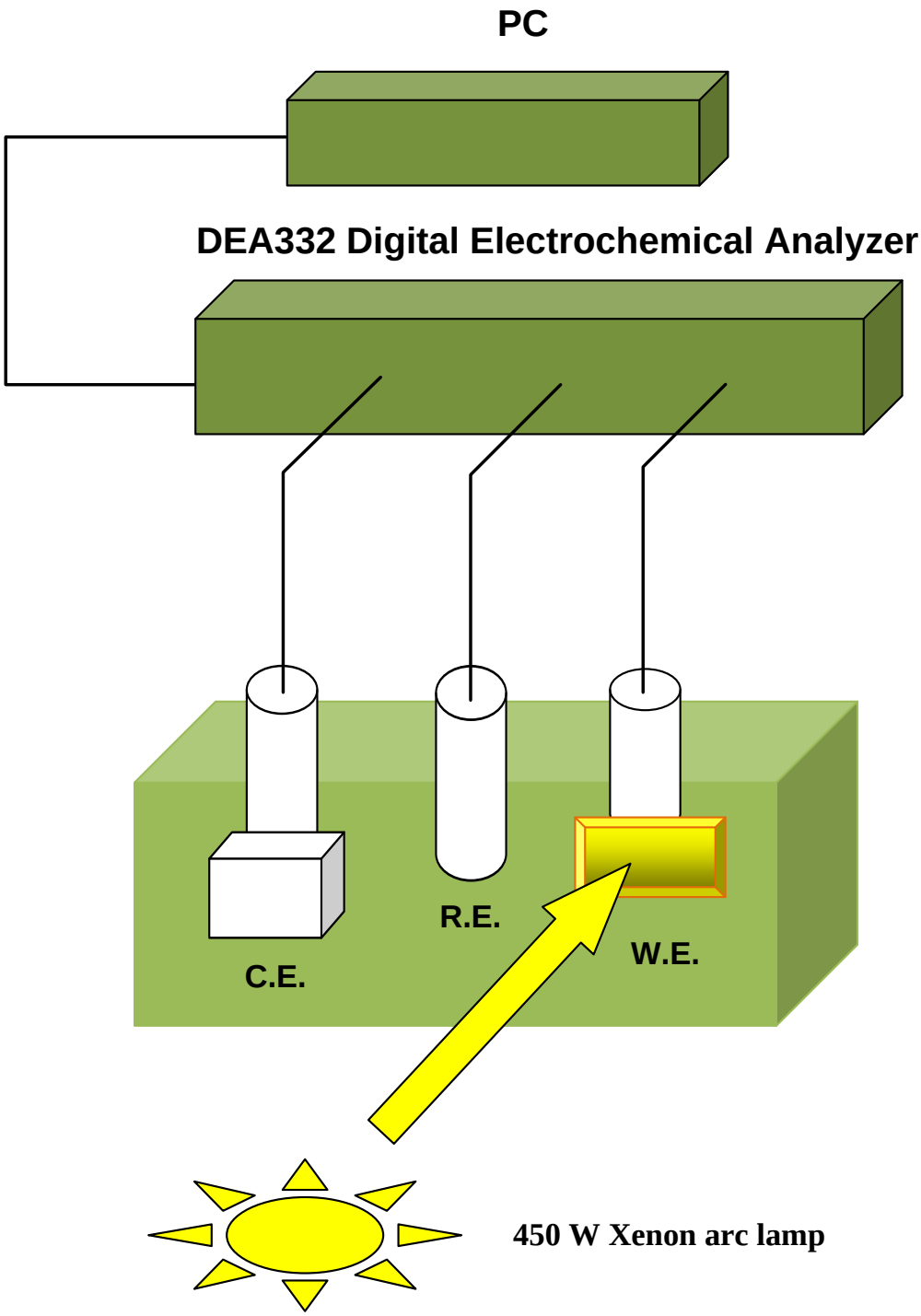

Figure 3-8 Experimental configuration for the photoelectrochemical measurements

4. CONTROLLING PARTICLE SIZE AND PHOTOELECTROCHEMICAL PROPERTIES OF NANOSTRUCTURED Fe_2O_3 WITH SURFACTANTS

4.1. Materials and methods

4.1.1. Materials

Chemicals, and their suppliers, used for this study are listed in Table 4-1. Fluorine-doped tin oxide (FTO) glass with a sheet resistance of $R_\Omega < 15$ Ω/sq was purchased from Pilkington Glass (USA).

Table 4-1 Chemicals used in this study

Name	Formula	Grade (%)	Supplier
Iron (III) Nitrate	$Fe(NO_3)_3.9H_2O$	99.9	Chem. supply Co.
Ethanol	C_2H_6O	70	Sigma Aldrich
PEG 300 (Polyethylene glycol 300)	$(C_2H_4O)_{6.4}H_2O$	99	Sigma Aldrich
T-100 (Triton X-100)	$(C_2H_4O)_{9.5}C_{14}H_{22}O$	99.9	Sigma Aldrich
F127 (Pluronic F127)	$HO(C_2H_4O)_{101}(C_3H_6O)_{56}(C_2H_4O)_{101}H$	99.9	Sigma Aldrich
CTAB (Cetyltrimethylammonium bromide)	$C_{19}H_{42}BrN$	98.5	AMRESCO
OTAB (Octadecyltrimethylammonium bromide)	$C_{21}H_{46}BrN$	98	Sigma Aldrich
TTAB (Tetradecyltrimethylammonium bromide)	$C_{17}H_{38}BrN$	99	Sigma Aldrich

4.1.2. Synthesis of Electrodes

The six FTO conductive glass substrates, 20 × 25 × 2 mm (width/length/thickness), were cleaned and sonicated in solvents sequentially (acetone, ethanol, acetone). The FTO glasses were separately immersed into the solvents and treated in an ultrasonic bath for 15 min for each wash. In the final stage, after this rinsing, the FTO glasses were dried using nitrogen gas. The compositions of solutions deposited onto the substrates are listed in Table 4-2, and they were prepared according to the following recipes:

a) PEG-300

Iron nitrate (2.02 g) was dissolved in 20 ml ethanol under ultrasonic irradiation; then 5 mL deionized water was added into the solution. 0.2 g concentrated PEG (consisting of 30 g PEG-300 and 30 g water) was added to the solution and stirred for 2 h at room temperature. The 0.4 mol L^{-1} deep red solution (pH ~ 2) was obtained.

b) T-100

Iron nitrate (2.5 g) was added to 1 ml water. 0.4 g Triton (X-100) was added to 1 ml ethanol and stirred for 10 min. Both solutions were mixed together and stirred for 2 h. A light red solution (pH ~ 1.7) was obtained.

c) F127

0.3 g F127 was added to 5 ml ethanol and stirred for 20 min. Then, 2 g iron nitrate was added to 1 ml deionized water. Both solutions were mixed and stirred for 3 h. The resultant solution was dark brown, with pH ~ 1.9.

d) CTAB

0.5 g CTAB was added to 4 ml of distilled water. The solution was stirred for 30 min. Then, 2 g iron nitrate was added to the solution. The mixture was stirred for 2 h and a dark orange solution (pH ~ 1.5) was obtained.

e) OTAB

A mixture of 0.5 g OTAB and 4 ml distilled water was stirred for 30 min. Subsequently, 2 g iron nitrate was added to the solution and stirred for 2 h. A yellow solution (pH ~ 1.8) was obtained.

f) TTAB

0.5 g TTAB was dissolved in 4 ml water after stirring for 30 min. Then 2 g iron nitrate was added to the solution and stirred for 2 h. A light orange solution (pH ~ 1.7) was obtained.

Table 4-2 Fe_2O_3 preparation methods for different samples

Sample	Iron (III) nitrate	Surfactant	Distilled water	Solvent (Ethanol)	Colour
PEG-300	2.02 g	0.2 g PEG	5 ml	20 ml	Deep red
T-100	2.5 g	0.4 g Triton	1 ml	1 ml	Light red
F127	2 g	0.3 g F127	1 ml	5 ml	Dark brown
CTAB	2 g	0.5 g CTAB	4 ml	----	Dark orange
OTAB	2 g	0.5 g OTAB	4 ml	----	Yellow
TTAB	2 g	0.5 g TTAB	4 ml	----	Light orange

Fe_2O_3 nanostructured photoanodes were prepared via the sol-gel spin coating method, using FTO glass substrates, and complied with the following deposition steps:

1. A spin coater (Laurell Tech., model WS-400-6NPP), at two fixed rotation speeds of 5 s (500 rpm) and 25 s (5000 rpm), was used to deposit a few drops of the resulting solutions onto the FTO substrates.
2. The substrates were dried on a hot plate (~ 50 °C) for 15 min.
3. To enhance the interconnectivity of the particles, samples were heated at 450 $\pm$ 1 °C, for 2 h, in air, with fixed heating and a cooling rate of 5 °C/min.

4.2. Results and discussion

4.2.1. Performance of the photoelectrochemical cell

Figure 4-1 shows the current density-voltage (J-V) curves, under illumination, for the photoelectrochemical cell with Fe_2O_3 nanostructures. The photoresponses of α-Fe_2O_3 films were evaluated by measuring photocurrent density, J_p. The externally applied bias was varied from -1.2 V/SCE (cathodic bias) to +1.2 V/SCE (anodic bias). The photocurrent density was normalized in order to eliminate the influence of film thickness. The results show a distinctive influence of the surfactants, with TTAB producing the highest photogeneration. As shown in Table 4-3, the photocurrent density of the TTAB-treated sample was 1.77 mA/cm^2 at 1 V/SCE, under an illumination intensity of 100 mW cm^{-2}, which is significantly larger than the values for the other samples (8 times more than PEG and 40% more than Triton and F127). The study demonstrates that cationic surfactants exhibit higher photogeneration when compare with the other samples. It should be noted that PEG, the sample with the lowest value, is often used in the sol-gel method. The photocurrent density of Fe_2O_3/PEG at 1.23 VRHE was 0.65 mA cm^{-2}, which is similar to the reported value for the same sample in the literature (0.89 mA cm^{-2}) [115].

4.2.2. Optical characterization

The optical properties (transmittance, absorption coefficient and optical band-gap energy) of surfactant-treated hematite films were determined from the variations in absorption density (Figure 4-2). Table 4-3 shows the UV-visible absorption values for all samples between 320 and 670 nm. The UV-vis analysis showed that cationic surfactants (TTAB, CTAB and OTAB) have higher levels of optical absorption, covering both UV and the visible spectrum. On the other hand, the values for the PEG and Triton samples diminished quickly with increasing wavelength. Again, the highest optical absorption value observed in the ultraviolet and visible region was for the Fe_2O_3/TTAB sample (350 A.U.). The results agree with improved photocurrent performance and confirm the assumption that the TTAB sample has a larger number of electron-hole pairs [87].

The band-gap of samples can be obtained from the absorption coefficient data, according to solid band theory [116]:

$$(\alpha hv) = A\left(hv - E_g\right)^m \quad (4\text{-}1)$$

where α is the absorption coefficient, hv is the energy of the incident photon, A is a constant related to the effective mass of the electrons and holes, E_g represents the energy band-gap of samples and m = 2 for allowed indirect transition.

Analysis found an onset region of around 600 nm, which is in agreement with the band-gap of α-Fe_2O_3. The band-gap values were determined from the curve extrapolations. Figure 4-3 presents the change in band-gap energy, E_g, after treating Fe_2O_3 with PEG and TTAB surfactants. It can be seen that the energy decreased slightly from indirect transition of 2.02 to 1.92 eV for Fe_2O_3 treated with PEG and TTAB, respectively. Similar values already have been reported in the literature, e.g. 2.05 eV [90] and 2 eV [53]. The indirect transition has been identified as a spin-forbidden $Fe^{3+} \rightarrow$ 3d excitation [117]. Furthermore, it has been observed that the surfactant-treated hematite film may not produce any intermediate level within the energy levels of iron oxide. These results are in good agreement with XRD diffraction data (shown below), which did not highlight any change in the structural parameters among the samples with various surfactants.

The calculated band-gaps are consistent with the measured optical absorption. Again, the Fe_2O_3 nanostructure treated with TTAB had the lowest band-gap when compared with the other samples. The lowest E_g, 1.92 eV, would be expected to generate the highest number of electron-hole pairs when illuminated with light. Moreover, with the lower band-gap, it is easier for electrons to be excited from the valence band to the conduction band of Fe_2O_3 [118].

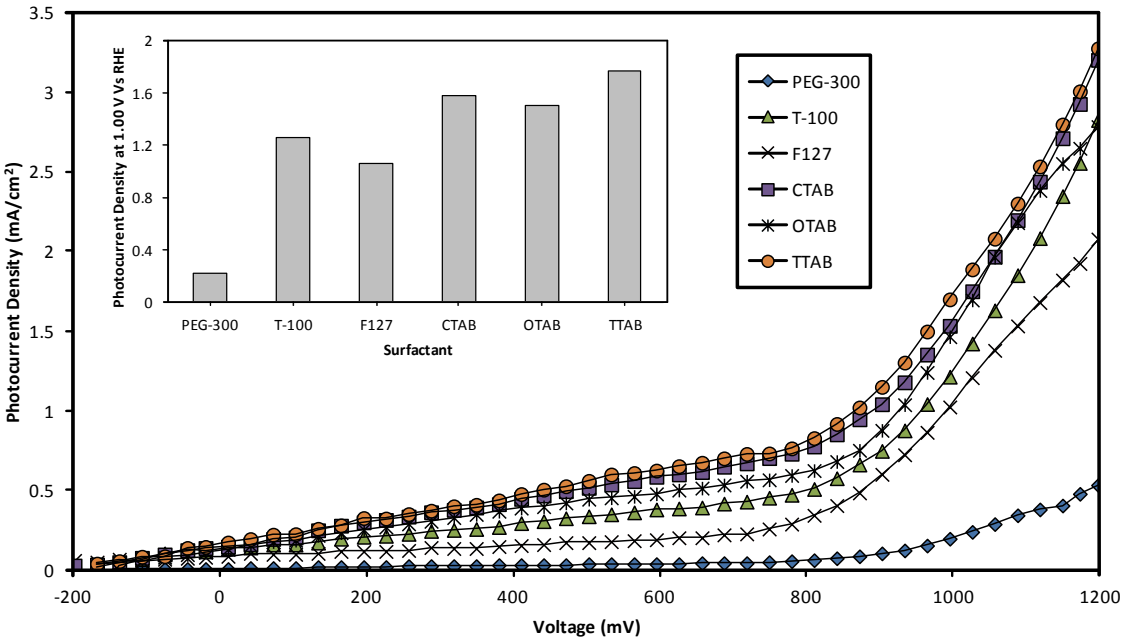

Figure 4-1 Photocurrent values of Fe_2O_3/PEG-300, Fe_2O_3/Triton X-100, Fe_2O_3/F127, Fe_2O_3/CTAB, Fe_2O_3/OTAB and Fe_2O_3/TTAB

Table 4-3 Comparison of various parameters as a function of Fe_2O_3 nanostructures treated with different types of surfactant

Sample	E_g (ev)	Absorption (A.U.) 320-670 nm	Grain size (nm)	Surface roughness R_z (nm)	Film Thickness (nm)	V_{aoc} (V/SCE)	Photocurrent density (mA/cm^2) At zero V/SCE	Photocurrent density (mA/cm^2) At 1 V/SCE
PEG-300	2.02	180	12 ± 2	2 ± 1	520 ± 10	- 0.180	0.000	0.220
T-100	1.99	262	21 ± 2	9 ± 1	660 ± 10	- 0.156	0.123	1.257
F127	2.00	237	16 ± 2	8 ± 1	980 ± 10	- 0.173	0.085	1.061
CTAB	1.94	290	50 ± 2	29 ± 1	850 ± 10	- 0.140	0.144	1.579
OTAB	1.96	285	36 ± 2	17 ± 1	770 ± 10	-0.151	0.131	1.510
TTAB	1.92	350	70 ± 2	32 ± 1	680 ± 10	-0.145	0.155	1.770

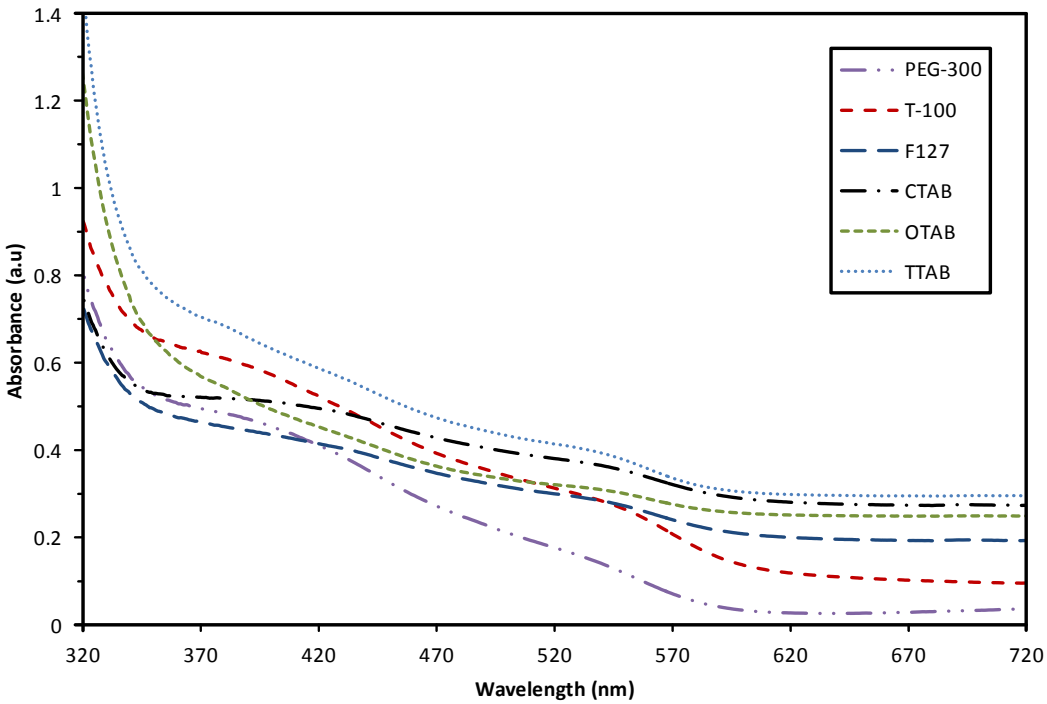

Figure 4-2 Absorption coefficients from transmittance measurements, normalized by individual thickness for all the samples

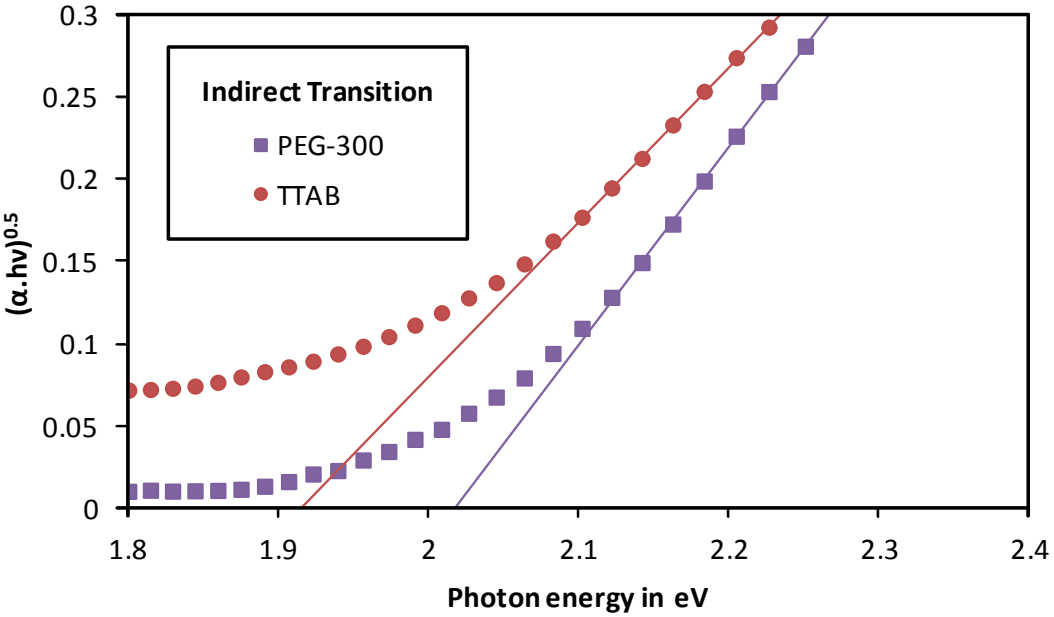

Figure 4-3 Calculation of the indirect electronic transition

4.2.3. Crystalline properties

In order to investigate phase formation and the crystalline properties of the films, XRD analysis was performed at room temperature. Similar hematite XRD signatures were obtained for all surfactant-treated hematite films (Figure 4-4). The diffraction peaks 24°, 33°, 34°, 36°, 41° and 55° in Figure 4-5a reveal the diffraction peaks of rhombohedral Fe_2O_3. Similar peak patterns also have been observed for α-Fe_2O_3 nanostructure film in studies carried out using the sol-gel method [48, 90].

The average crystallite size has been estimated from the Debye-Scherrer equation using the (110) peak:

$$D = 0.94\lambda/\beta \cos\theta \quad (4\text{-}2)$$

where D is the crystalline dimension, λ is the wavelength of the X-ray radiation (which is 0.15418 nm), θ is the diffraction angle and β is the full width at half maximum.

From Table 4-3, it can be seen that surfactants can strongly influence the crystallite size, with TTAB having particles almost six times bigger than the PEG sample. Also, it can be seen that the grain size is directly correlated to the optical absorption and the photocurrent density, i.e. bigger grain size gives better optical absorption and photoresponses. The correlation is expected and consistent with another previous study [48].

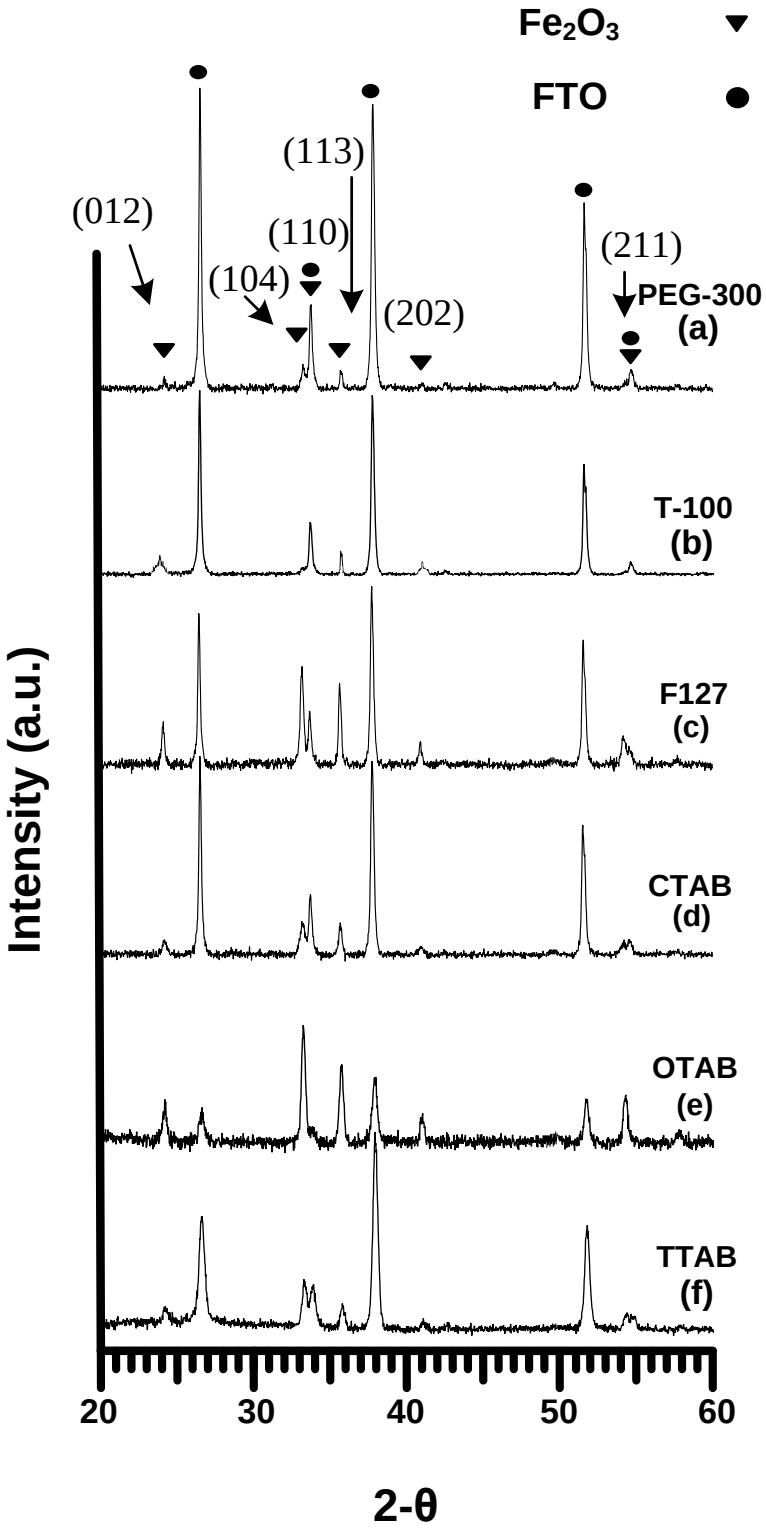

Figure 4-4 X-ray diffraction patterns of Fe_2O_3/PEG-300, Fe_2O_3/Triton X-100, Fe_2O_3/F127, Fe_2O_3/CTAB, Fe_2O_3/OTAB and Fe_2O_3/TTAB

4.2.4. Surface morphology

Field emission scanning electron microscopy was employed to investigate the morphology of the samples. The surfaces of the films were observed using a Zeiss NEON 40EsB CrossBeam FIBSEM, operating at 3 kV for both top and cross-sectional views, using the InLens detector. The SEM micrographs of six samples (Figure 4-5) show distinctive features, which correspond well to the XRD results.

The morphology of the Fe_2O_3/PEG film shows a uniform, smooth and compact structure with worm-like grains at a nanometric scale (Figure 4-5a). Treatment with the Triton-100 reduced the grain size (Figure 4-5b), which resulted in columnar tree-like structures. On the other hand, F127-treated Fe_2O_3 thin films formed a homogeneous and uniform surface (Figure 4-5c). CTAB-treated samples (Figure 4-5d) comprised of small clusters, about 250 nm in width, which consisted of much smaller primary particles in the range of 40-50 nm. During the annealing process for the CTAB sample, these smaller nanoparticles expectedly dispersed in the surface and formed a very compact layer. The morphology of OTAB- and TTAB-treated samples was similar to each other: uniform, compact, worm-like and without any cracks (Figures 4-5e and 4-5f).

The film thickness was measured by FIBSEM, and ranged between 520 $\pm$ 10 nm and 980 $\pm$ 10 nm. An uncoated, fluorine–doped, conductive oxide layer, with a thickness of about 820 nm, is shown in Figure 4-6. This image highlights the good adherence to the FTO substrate. There is no clear correlation between film thickness and particle size or grain size.

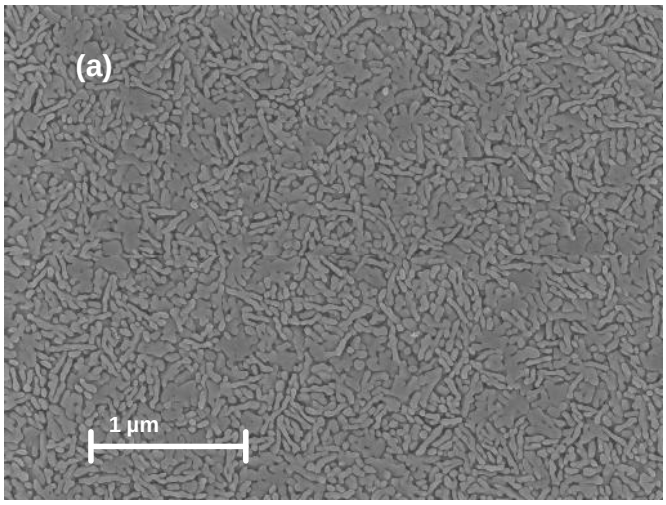
(a)
1 µm

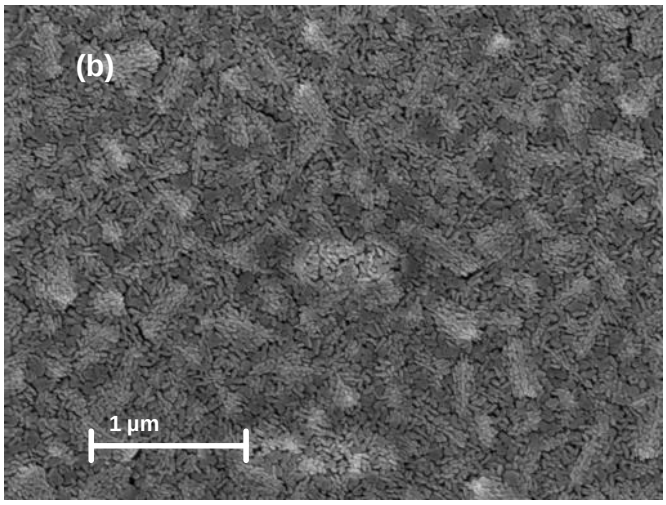
(b)
1 µm

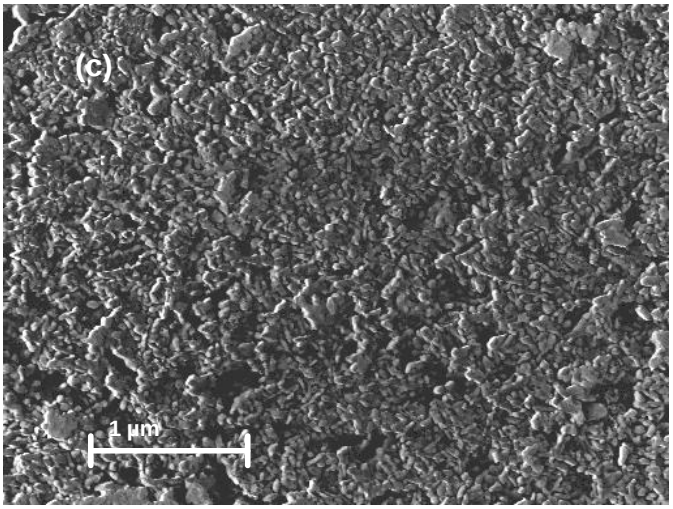
(c)
1 µm

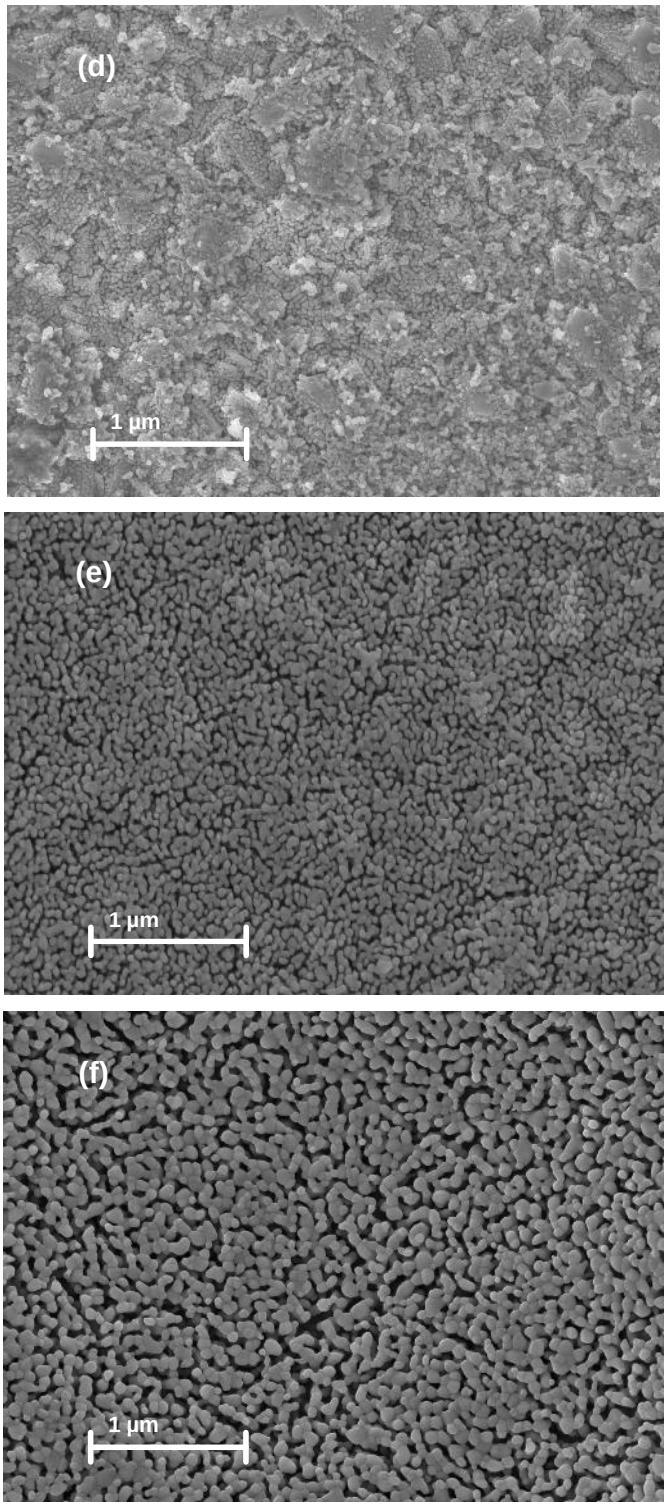

Figure 4-5 SEM images of the surface of films deposited by spin-coating solution on the FTO substrate with thickness of about 820 nm, (a) Fe_2O_3/PEG-300, (b) Fe_2O_3/Triton X-100, (c) Fe_2O_3/F127, (d) Fe_2O_3/CTAB, (e) Fe_2O_3/OTAB and (f) Fe_2O_3/TTAB

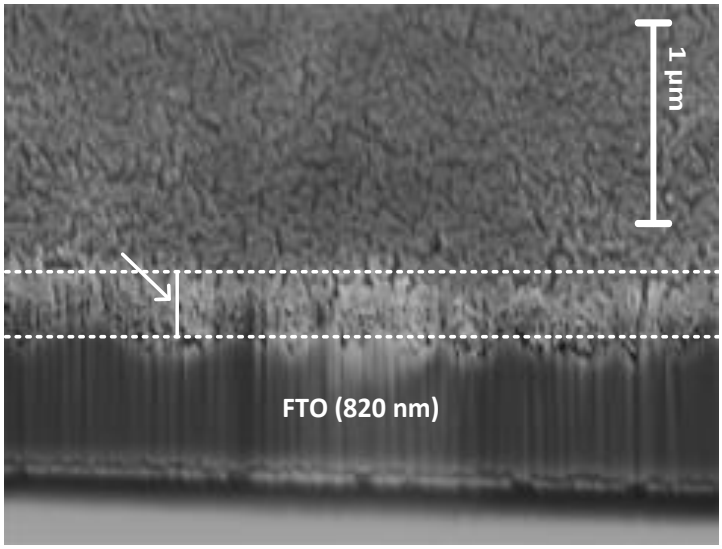

Figure 4-6 Cross-sectional view of Fe_2O_3/PEG-300 film

In order to investigate the surface roughness of the films, atomic force microscopy (AFM) measurements were performed. AFM images obtained for surfactant-treated hematite thin films are shown in Figure 4-7. The estimated average values of the grain sizes were found to closely match the average particle/grain sizes obtained from XRD. AFM photographs of surfactant-treated hematite films show that the Fe_2O_3/TTAB film was very rough, with extensive granular structures covering the film surface. This leads to a large number of intergranular surfaces and higher possibilities of surface-related effects. On the other hand, the F127 and PEG surfactants significantly reduced the surface roughness (Table 4-3). Among these samples, the PEG-treated film had the smoothest surface, with a roughness of only 2 nm.

The influence of surface roughness on photocurrent can be explained by the light absorption process. In general, a beam of radiation can be reflected, scattered and transmitted on the surface of a sample. However, the diffuse reflection phenomena, due to scattering of light, can increase the amount of absorption. On the other hand, a rough surface with large grain size can exhibit significantly increased diffuse reflection in the visible light region. A rough surface also has a higher electrode/electrolyte interfacial contact area, which enhances photocurrent and the multiple scattering of UV-vis light. The results confirmed that the film with the larger grain sizes and higher surface roughness (TTAB) displayed a better photocurrent.

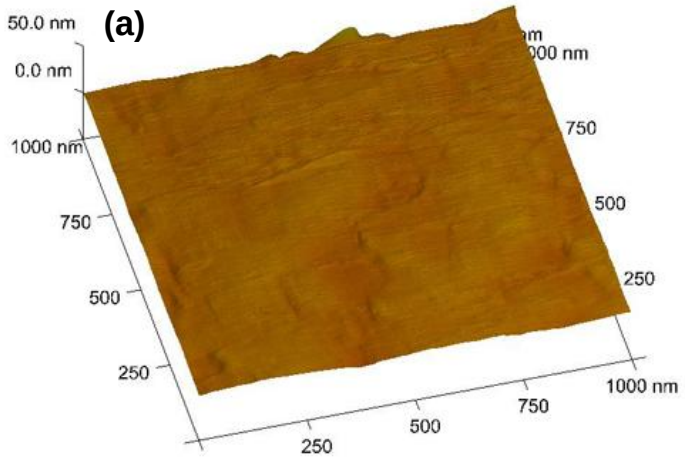
(a)
50.0 nm
0.0 nm
1000 nm
750
500
250
250
500
750
1000 nm

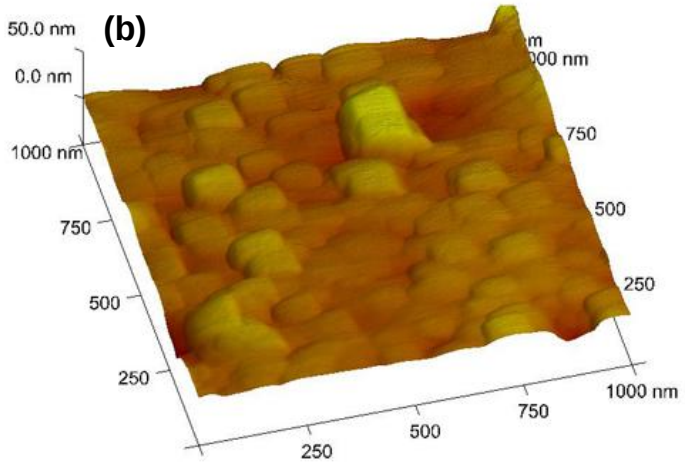
(b)
50.0 nm
0.0 nm
1000 nm
750
500
250
250
500
750
1000 nm

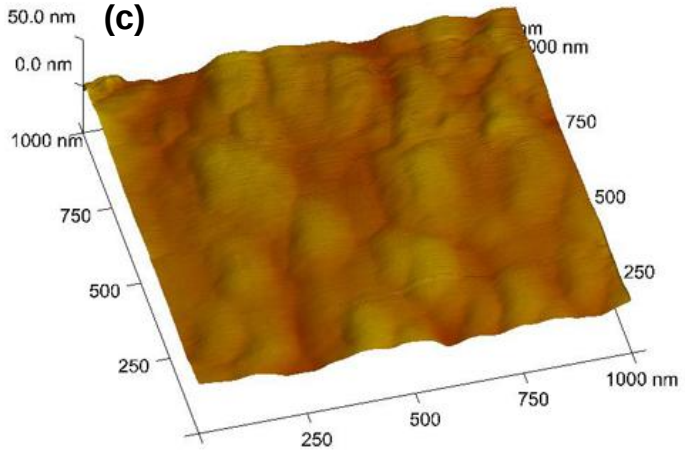
(c)
50.0 nm
0.0 nm
1000 nm
750
500
250
250
500
750
1000 nm

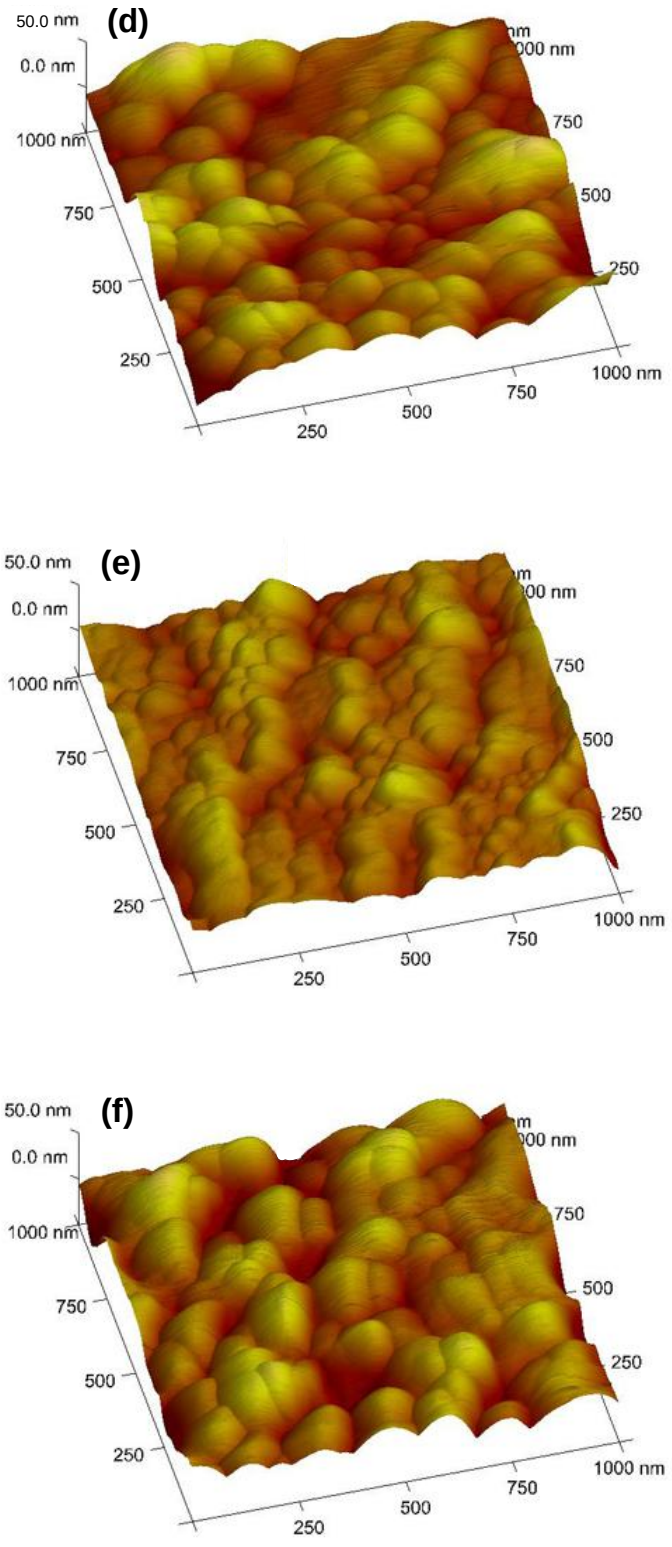

Figure 4-7 AFM images for (a) Fe_2O_3/PEG-300, (b) Fe_2O_3/Triton X-100, (c) Fe_2O_3/F127, (d) Fe_2O_3/CTAB, (e) Fe_2O_3/OTAB and (f) Fe_2O_3/TTAB

4.3. Controlling particle size of Fe_2O_3 nanoparticles with cationic surfactant

As has been mentioned previously in section 4-2-4, we have successfully synthesised Fe_2O_3 nanoparticles in the range of 12 – 70 nm using non-ionic and cationic surfactants. However, using cationic surfactants (TTAB ($C_{17}H_{38}BrN$), CTAB ($C_{19}H_{42}BrN$) and OTAB ($C_{21}H_{46}BrN$)), the particle size of Fe_2O_3 was decreased by increasing the surfactant particle sizes (from 32 nm to 17 nm). The relationship between the molecular sizes of surfactant and Fe_2O_3 particles follows in the equation (4-3):

$$D = D_0 + \frac{C_0}{M} \tag{4-3}$$

where D is the particle size, D_0 is the critical particle size, C_0 is constant and M is the molecular weight of the surfactant head.

Therefore, by taking the log of both sides of the equation we will have:

$$Log\ D = Log\ D_0 - C_0\ Log\ M \tag{4-4}$$

Figure 4-8 presents the best line of fit ($R^2 = 0.9995$) corresponding to equation 4-3. The values of slopes and intercepts of the line would be as follows.

$C_0 = 3.1924$, Log $D_0 = 9.457$

As can be seen from Figure 4-8, when Log M reaches to infinity, Log D reaches to Log D_0. This could be further evidence that the relationship between the Fe_2O_3 particle size and the molecular weight of the surfactant follows equation (4-3).

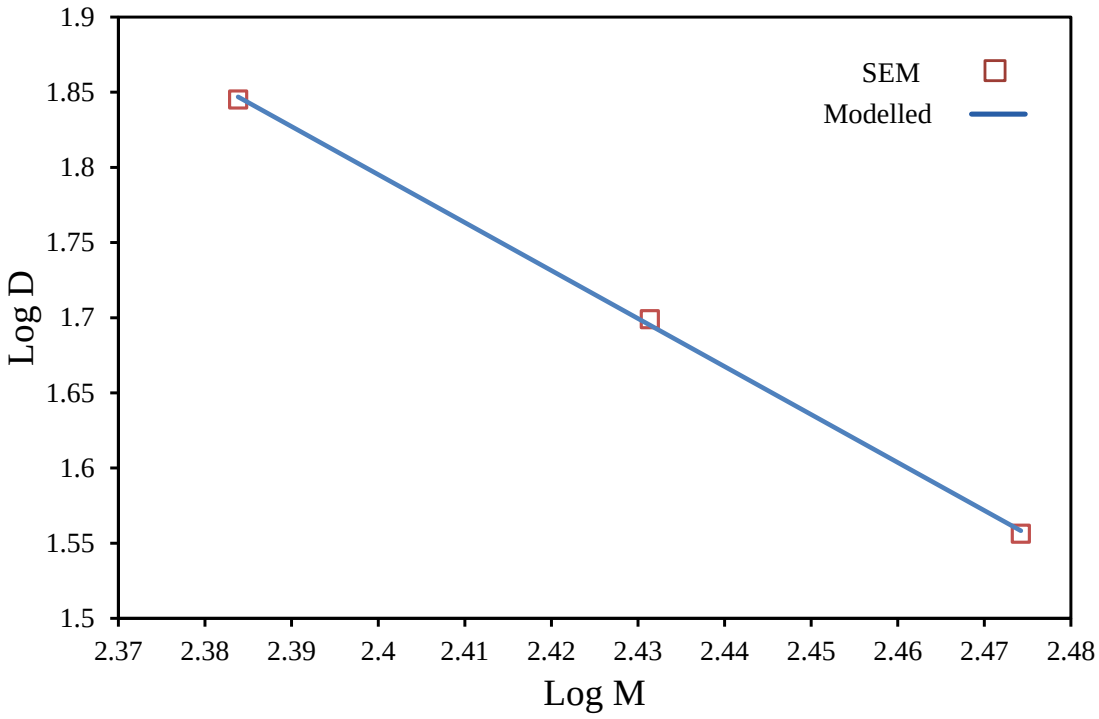

Figure 4-8 Fitted empirical equation for determination of the characterized size of Fe_2O_3 nanoparticles vs molecular weight of cationic surfactant

4.4. Proposed mechanism for relationship between surfactant structure and Fe_2O_3 film

In order to predict and manipulate the size of Fe_2O_3 nanoparticles treated with cationic surfactants, a model has been developed based on obtained experimental results. In this section, the model will be expanded further to find the correlation between surfactant adsorption time, molecular weight of surfactants and characterized size of nanoparticles. Two different methods: namely, adsorption density of the surfactant and the vacant spaces between the surfactant particles will be utilized to explain the relationship.

4.4.1. Adsorption density of cationic surfactants

The presented equation in chapter 2 (equation 2-3) can be used to describe the growth of individual crystals of average particle diameter, *D*, dispersed in a homogeneous matrix:

$$D = D_0 + k\, t_{eff}^{1/2} \qquad (2\text{-}3)$$

Comparing equation 2-3 and the obtained equation from experimental data (equation 4-3) will provide us with:

$$k\ t_{eff}^{1/2} = \frac{C_0}{M} \tag{4-5}$$

Thus, t_{eff} can be calculated as:

$$t_{eff} = (\frac{C_0}{M\ k})^2 \tag{4-6}$$

As it can be clearly understood from equation (4-6), $t_{eff} = (\frac{A_1}{M})^2$ (A_1 is constant). Therefore, the adsorption time of the cationic surfactant has an inverse relationship with the molecular weight of the surfactant (equation 4-6), and there is a direct correlation with the characterized size of the nanoparticles (equation 2-3). These results are consistent with experimental data and prove the obtained data on characterization size of Fe_2O_3 nanoparticles using cationic surfactant.

4.4.2. Vacant space between cationic surfactants

Equation 2-4 can be utilized to find the relationship between the vacant space between cationic surfactant (C_p) and the characterized size of the nanoparticles, thus:

$$D = D_0 + k\ C_p\ t_{eff}^{1/2} \tag{2-4}$$

Applying equation (4-5) into equation (2-4), we would have:

$$D = D_0 + \frac{C_0\ C_p}{M} \tag{4-7}$$

Moreover, calculating C_p would provide us with the following equation (A_2 is constant):

$$C_p = \frac{1}{A_2\ M} \tag{4-8}$$

Therefore, from equations (4-7) and (4-8) it can be concluded that, with increasing vacant position between each pair of cationic surfactant characterized size of Fe_2O_3 nanoparticle would be increased. Also, molecular weight of cationic surfactant has an

inverse relationship with the vacant position of cationic surfactant. Moreover, these correlations are consistent with the obtained experimental results for the Fe_2O_3 nanoparticles.

The influence of vacant space between cationic surfactants (C_p) on characterized size of Fe_2O_3 nanoparticle is presented in Figure 4-9 schematically. During calcination, surfactants are adsorbed into the crystal surface and prevent the ions (Fe^{3+}, O^{2-}) from contacting the crystal surface. For the range of concentrations, > 10 CMC, the surfactant adsorption layer should be saturated immediately after nucleation. However, some ions, being smaller than surfactant tail, can get through the spaces between the adsorbed surfactant. For the smaller surfactants, the spaces between adsorbed surfactants remain relatively large and thus allow more ions to pass through. Consequently, larger grains and thicker film are formed after nucleation. For large surfactants, in contrast, the spaces between adsorbed surfactants are smaller and, thus, less ions can pass though. As a result, the grains are smaller.

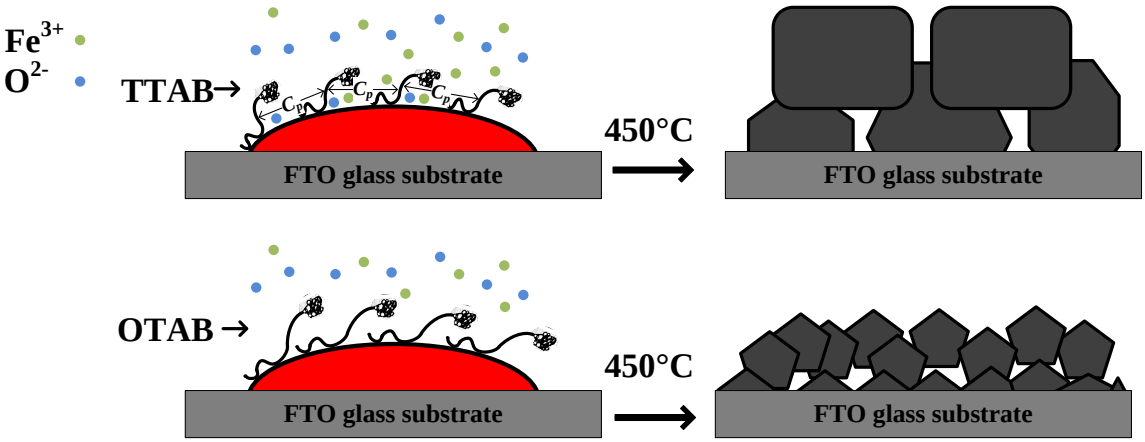

Figure 4-9 Influence of vacant space between cationic surfactants on characterized size of Fe_2O_3 nanoparticle

4.5. Discussion

Among the six samples, the TTAB-treated film clearly demonstrated the best photoresponse. The high photocurrent of the TTAB sample is consistent with UV-vis optical absorption and the estimated band-gap. Therefore, it can be concluded that the

TTAB-treated sample can generate the highest number of electron-hole pairs under illumination. This conclusion also is supported by morphology characterization, which showed that TTAB produced larger grain size. Additionally, surface roughness has an enhancement effect upon photocurrent yield due to the large specific surface area (contact area) and strong scattering of light (diffuse reflection).

The results showed that surfactant-treating of the film can release the internal stress, relax the distortion of the crystal lattice and improve the crystallinity, which increases the photocatalytic activity. On the other hand, decreasing particle size increases the surface tension and causes a crystal lattice distortion. Hence, the larger grain size can increase the photocatalytic activity of the Fe_2O_3 thin film, as demonstrated by the TTAB-treated sample. The results highlighted the superior performance of cationic surfactants over non-ionic surfactants in preparing photoanodes by the sol-gel method. Among the cationic surfactants, TTAB had the best photoresponse. The improved performance of the TTAB sample can be attributed to the shorter surfactant tail length. It is evident that the crystallite size decreases gradually as the surfactant tail length increases: TTAB > CTAB > OTAB. The results are consistent with another result in the literature for the same surfactant series: increasing the surfactants' tails led to decreasing crystallite size [119].

4.6. Conclusions

Fe_2O_3 nanostructures have successfully been prepared with surfactants (PEG, Triton, F127, CTAB, OTAB and TTAB) on an FTO substrate using the sol-gel spin coating technique. The surfactants distinguishably altered the morphology of the resulting Fe_2O_3 nanoparticle layers. The PEG and F127 surfactants produced smoother surfaces than the other surfactants. PEG produced the smoothest surface and the lowest photocurrent. More significantly, the surfactants significantly influenced the photocurrent and optical absorption of the Fe_2O_3 layer. Overall, the three cationic surfactants exhibited better photocatalytic activity of the Fe_2O_3 nanostructured photoanode than the three non-ionic surfactants. Among the cationic surfactants, TTAB revealed the best performance: highest current density (more than eight times in comparison with PEG), lowest band-gap (1.92 eV) and highest absorption (350 A.U.). These results indicate that the TTAB-

treated sample had the highest number of electron-hole pairs under illumination, which also is supported by morphological characterization (largest grain size and roughest surface). The study demonstrates that the photoelectrochemical performance of Fe_2O_3 nanostructures can be improved by simply varying the surfactant.

In this chapter, a model prediction was also obtained to predict the behaviour of Fe_2O_3 nanoparticles using a series of different cationic surfactants. A linear equation of $Log\ D = Log\ D_0 - C_0\ Log\ M$ was obtained to predict the behaviour of Fe_2O_3 nanoparticles using cationic surfactants. The values of slopes and intercepts of the line also were calculated (C_0 = 3.1924, $Log\ D_0$ = 9.457).

The results highlighted the superior performance of cationic surfactants over non-ionic surfactants in preparing Fe_2O_3 photoanodes by the sol-gel method. In comparison to PEG, a common surfactant used in the sol-gel method, TTAB can increase the grain size by six times and increase photocurrent density by eight times (at 1 V). The results can be attributed to the crystallization process of TTAB which leads to the larger grain size and highest photocatalytic activity. In summary, the study found two main results: (i) cationic surfactant is better than non-ionic surfactant and (ii) among cationic surfactants, shorter tails produce better photoanodes.

5. CONTROLLING PARTICLE SIZE AND PHOTOELECTROCHEMICAL PROPERTIES OF NANOSTRUCTURED WO_3 WITH TRITON SURFACTANT

5.1. Material and methods

5.1.1. Materials

Chemicals, and their suppliers, used for this study are listed in Table 5-1. Fluorine-doped tin oxide (FTO) glass with a sheet resistance of $R_\Omega < 15$ Ω/sq was purchased from Pilkington Glass (USA).

Table 5-1 List of the chemicals used in the study

Name	Formula	Grade (%)	Supplier
Tungsten powder	W	99	Sigma Aldrich
Hydrogen peroxide	H_2O_2	30	AMRESCO
Ethanol	C_2H_6O	70	Sigma Aldrich
Platinum black powder	Pt	99	Sigma Aldrich
Propan-2-ol	C_3H_7OH	70	Chem Supply
T-X45 (Triton X-45)	$(C_2H_4O)_{4.5}C_{14}H_{22}O$	99	Sigma Aldrich
T-X100 (Triton X-100)	$(C_2H_4O)_{9.5}C_{14}H_{22}O$	99	Sigma Aldrich
T-X305 (Triton X-305)	$(C_2H_4O)_{30}C_{14}H_{22}O$	99	Sigma Aldrich
T-X405 (Triton X-405)	$(C_2H_4O)_{35}C_{14}H_{22}O$	99	Sigma Aldrich
T-X705 (Triton X-705)	$(C_2H_4O)_{55}C_{14}H_{22}O$	99	Sigma Aldrich

5.1.2. Preparation of the electrodes

Six FTO conductive glasses with dimensions of 20×25×2 mm (width/length/thickness) were ultrasonically cleaned for 15 minutes with acetone, ethanol and acetone, sequentially. Finally, after rinsing, the FTO glasses were blow-dried with nitrogen.

The solutions, with compositions given in Table 5-2, were prepared according to the following method [120]:

(1) Dissolving 0.5 g of tungsten powder in 15 mL of 30% (w/w) hydrogen peroxide aqueous solution, in a Pyrex container, to form peroxotungstic acid (PTA) and setting aside for about 6 hours.

(2) Decomposing the excess hydrogen peroxide by adding 1 mg of platinum black.

(3) Diluting the solution to 0.1 M by adding about 10 mL of propan-2-ol.

Propan-2-ol was added to extend the stability of the PTA solution by preventing the precipitation of an amorphous WO_3-based hydrate phase [121]. It is worth noting that the prepared solution containing 2-propanol must be used within two days, in order to avoid any cracking of the WO_3 film surface [99]. The experimental setup has been described in detail previously [120]. The deposition process for the WO_3 nanostructure used surfactants as structure-directing agents. For each sample, 3 mL solution of 0.8g Triton surfactant and 5 mL ethanol were added to the tungsten solution. Since critical micelle concentrations (CMC) of Triton surfactants in pure water are around 1 mM [122], the selected concentrations are higher than 10 CMC for all surfactants. The pH values, measured with a pH/conductivity meter (Horiba F54, Japan), were between 1 and 2. The pH values for each sample have been reported in Table 5-2. WO_3 nanostructure photoanodes were prepared via the sol-gel spin coating method onto FTO glass, based on this author's previous published work [8].

Table 5-2 WO_3 preparation methods for different samples

Sample	WO_3 powder (g)	H_2O_2 (mL)	Platinum black (mg)	propan-2-ol (mL)	Surfactant	Solvent (mL)	pH
T-X45	0.5	15	1	10	0.8 g Triton X-45	5 ethanol	1.1
T-X100	0.5	15	1	10	0.8 g Triton X-100	5 ethanol	1.4
T-X305	0.5	15	1	10	0.8 g Triton X-305	5 ethanol	1.9
T-X405	0.5	15	1	10	0.8 g Triton X-405	5 ethanol	1.6
T-X705	0.5	15	1	10	0.8 g Triton X-705	5 ethanol	1.3

5.1.3. Characterization of electrodes

Crystallite size analysis and phase identification were performed using X-ray diffraction (XRD, Bruker D8 Advance), Cu Kα radiation (λ = 0.15418 nm). Diffraction peaks were recorded in the interval $20° \leq 2\theta \leq 60°$ at a scan rate of $0.01° \ s^{-1}$ in order to characterize the film samples. The absorbance was measured with a UV-visible Spectrophotometer (JASCO, V- 670 spectrophotometer), while field emission scanning electron microscopy (FESEM, Zeiss NEON 40EsB CrossBeam FIBSEM) and atomic force microscopy (Nanoscope (R) IIIa, Digital Instruments, Santa Barbara, CA) were used to determine the morphology of the thin films. The surface area also was investigated using the BET technique under constant N_2 adsorption at 77 K (Quantachrome, Autosorb-1).

5.1.4. Photoelectrochemical measurements

PEC measurements were performed in a three-electrode cell (reference, counter and working) equipped with an optical quartz window. The reference and counter electrodes were Ag/AgCl and platinum wire, respectively, which were immersed in a 1 M sulfuric acid solution as the electrolyte, while the working electrode was made by sol-gel deposition of films consisting of WO_3 nanoparticles with different surfactants. The preparation method for these films was mentioned, in detail, in the author's previous work [8].

5.2. Results and discussion

5.2.1. Characterization

Crystalline properties

Crystalline properties and the formation of phases were investigated by X-ray diffraction analysis (Figure 5-1). The WO_3 peaks (⋆) were observed at 23.3°, 24.1°, 24.9°, 29°, 33.9°, 35.1°, 42.5°, 50.5° and 56.4°. The sharp diffraction peaks at 23.3°, 24.1° and 24.9° demonstrated a monoclinic WO_3 crystal phase. Furthermore, diffraction peaks positioned at 33.9° and 35.1° correspond to orthorhombic subcell packing, according to JCPDS data (JCPDS 43-1035). Similar signatures were obtained for all samples. The obtained XRD results were in a good agreement with the literature [48, 123]. Also, peaks related to SnO_2 were observed in two ranges (26.5°, 34.5°, 38° and 51.2°, 57°) on conductive glass (▼). It is noteworthy that no surfactant-corresponding peak was observed, which confirms a complete removal of the surfactants during calcination.

Surface morphology

Field emission scanning electron microscopy (FESEM) was employed to investigate the morphology of the samples by operating at 3 kV for both top surface and cross-sectional views. The SEM micrographs in Figure 5-2 reveal the distinctive grain sizes of samples calcined at 450 °C. The nanoparticles with grain sizes of between 75 ± 15 and 140 ± 15 was dispersed homogeneously within a film thickness. The cross-sectional views (insets in Figure 5-2) demonstrate the effects of the surfactant heads on the film thickness. The thickness was decreased from 3.532 µm for the Triton X-45 sample to 2.520 µm for Triton X-705.

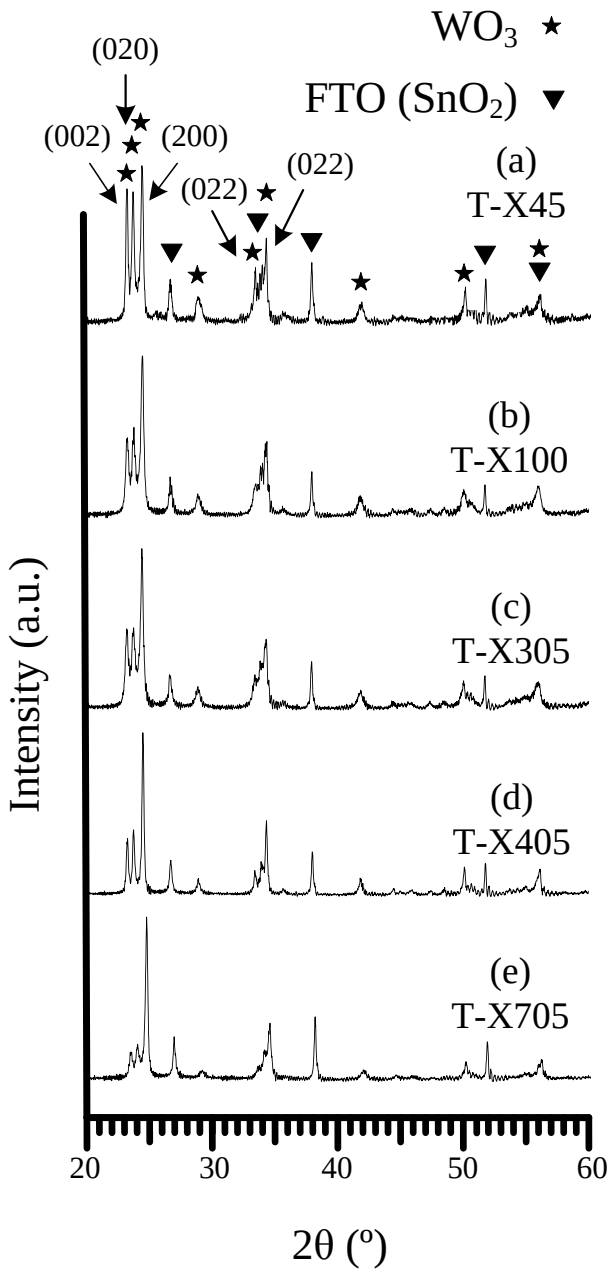

Figure 5-1 X-ray diffraction patterns for annealed samples of (a) WO_3/Triton X-45, (b) WO_3/Triton X-100, (c) WO_3/Triton X-305, (d) WO_3/Triton X-405 and (e) WO_3/Triton X-705

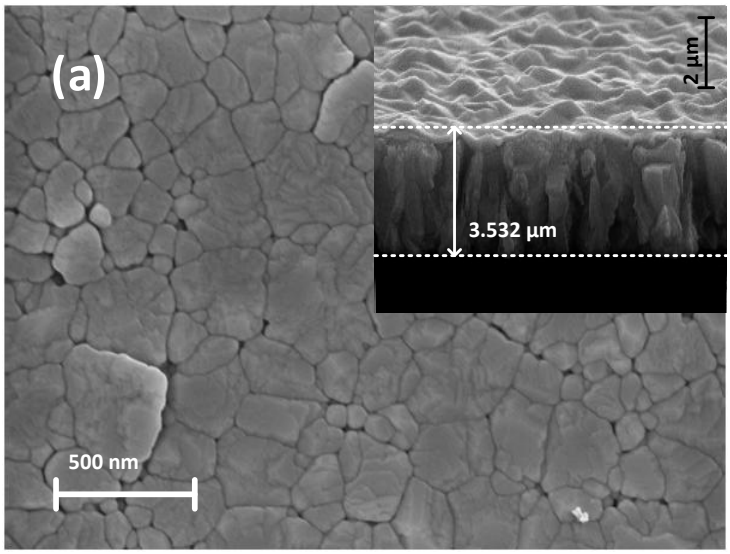
(a)
2 µm
3.532 µm
500 nm

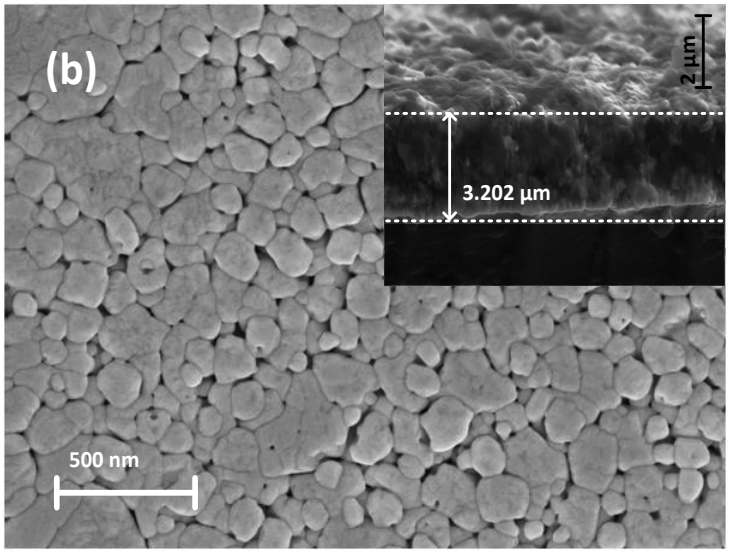
(b)
2 µm
3.202 µm
500 nm

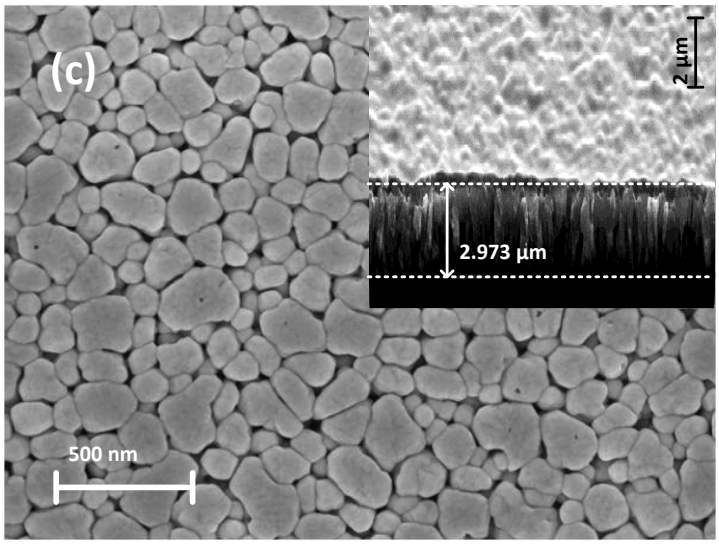
(c)
2 µm
2.973 µm
500 nm

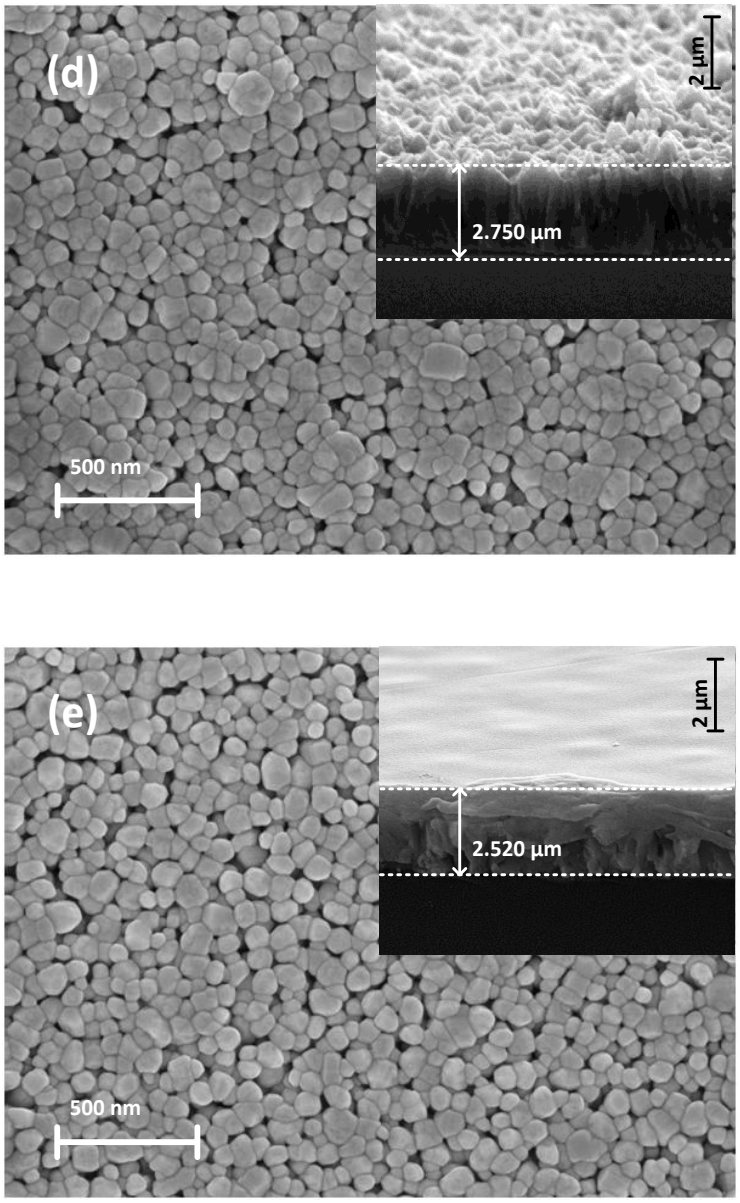

Figure 5-2 SEM images of the surfaces of films deposited by spin coating solution onto the FTO substrate with a thickness of about 820 nm: (a) WO_3/Triton X-45, (b) WO_3/Triton X-100, (c) WO_3/Triton X-305, (d) WO_3/Triton X-405 and (e) WO_3/Triton X-705

Particle size

Crystallite, grain and particle sizes were obtained from BET, SEM and XRD, respectively. The average crystallite size via XRD was calculated from the Debye-Scherrer equation:

$$D = \frac{0.94\lambda}{\beta} cos\theta \quad (5\text{-}1)$$

where D is the crystalline dimension, λ is the wavelength of the X-ray radiation (0.15418 nm), θ is the diffraction angle and β is the full width at half maximum.

Particle size also was calculated from BET surface area [124] by:

$$D = \frac{6}{\rho\, S_g} \quad (5\text{-}2)$$

where ρ is the specific density of WO_3 (7.16 g/cm^3) and S_g is BET surface area.

The effect of increasing the molecular weight of surfactants on particle size is shown in Figure 5-3. It can be seen that, as the hydrophobic surfactant head length increased, the overall particle size of the surfactant decreased dramatically from 140 nm to around 80 nm. The values for particle size, grain size and crystallite size are tabulated in Table 5-3. Later, in Chapter 6, the behaviour of surfactant-treated WO_3 photocatalysts will be modelled in terms of particle size. Having this model will help us to synthesis nanoparticles with desirable sizes.

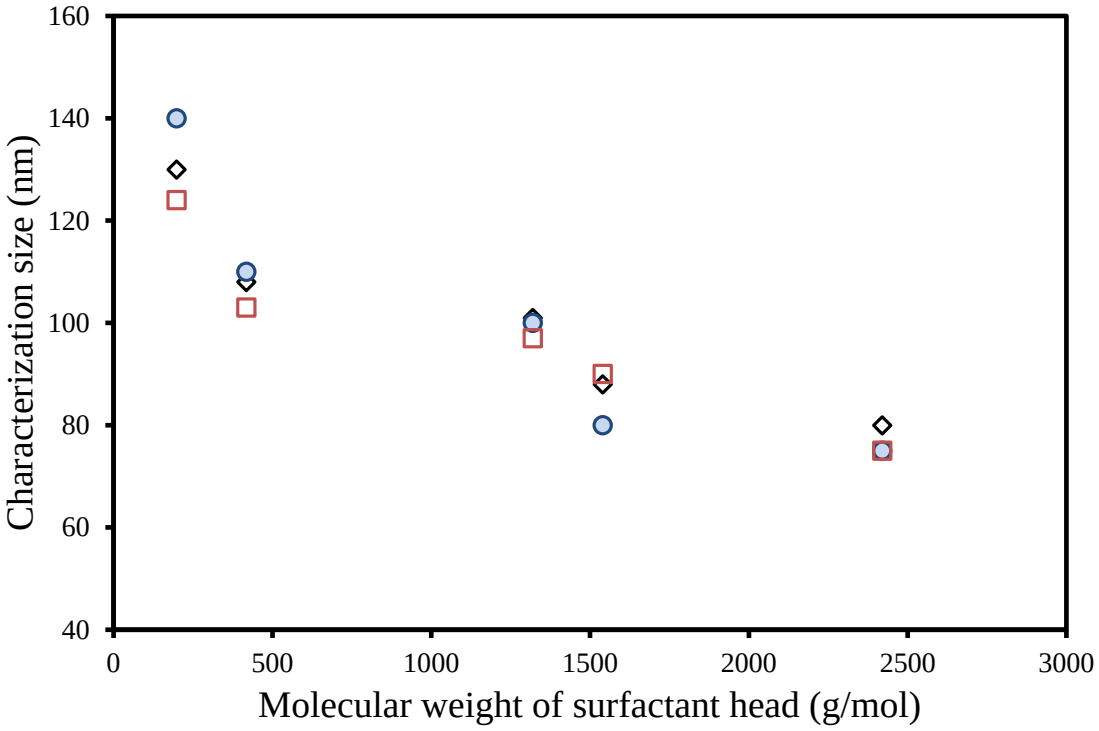

Figure 5-3 Characterized sizes obtained from XRD □, SEM ○ and BET ◊ versus molecular weight of Triton surfactants

Table 5-3 Surface area and characterized size of different samples

Sample	BET area (m^2/g)	Particle size (from BET area) (nm)	Grain size (from SEM image) (nm)	Crystallite size (from XRD patterns) (nm)	Surface roughness (nm)	Film Thickness (μm)
T-X45	6.4	130	140 ± 15	124	17 ± 1	3.532
T-X100	7.7	108	110 ± 15	103	14 ± 1	3.202
T-X305	8.3	101	100 ± 15	97	12 ± 1	2.973
T-X405	9.5	88	80 ± 15	90	9 ± 1	2.750
T-X705	10.4	80	75 ± 15	75	4 ± 1	2.520

Surface roughness

The AFM images are shown in Figure 5-4, with measured roughness tabulated in Table 5-3. The Triton X-45 film showed the roughest surface among the six samples. On the other hand, Triton X-705 significantly reduced the surface roughness and produced the smoothest surface, with a roughness of 4 nm.

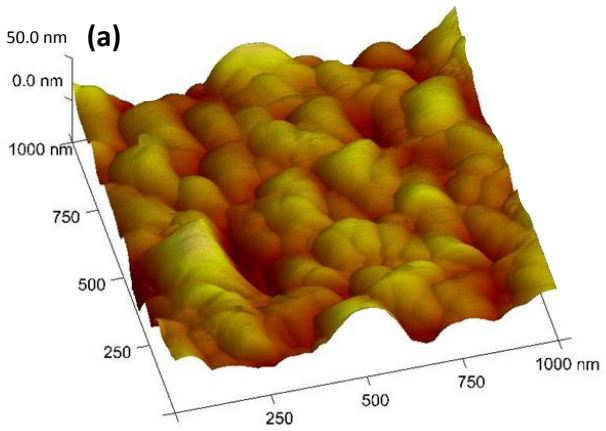

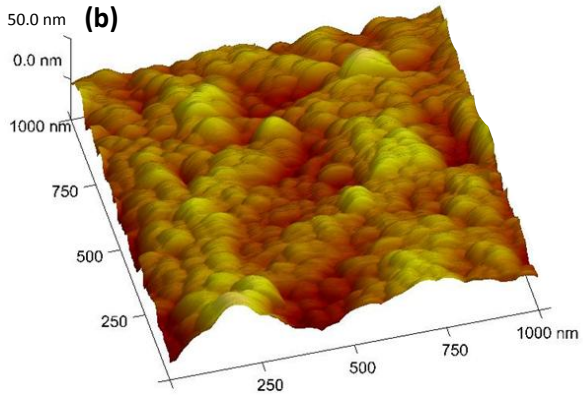

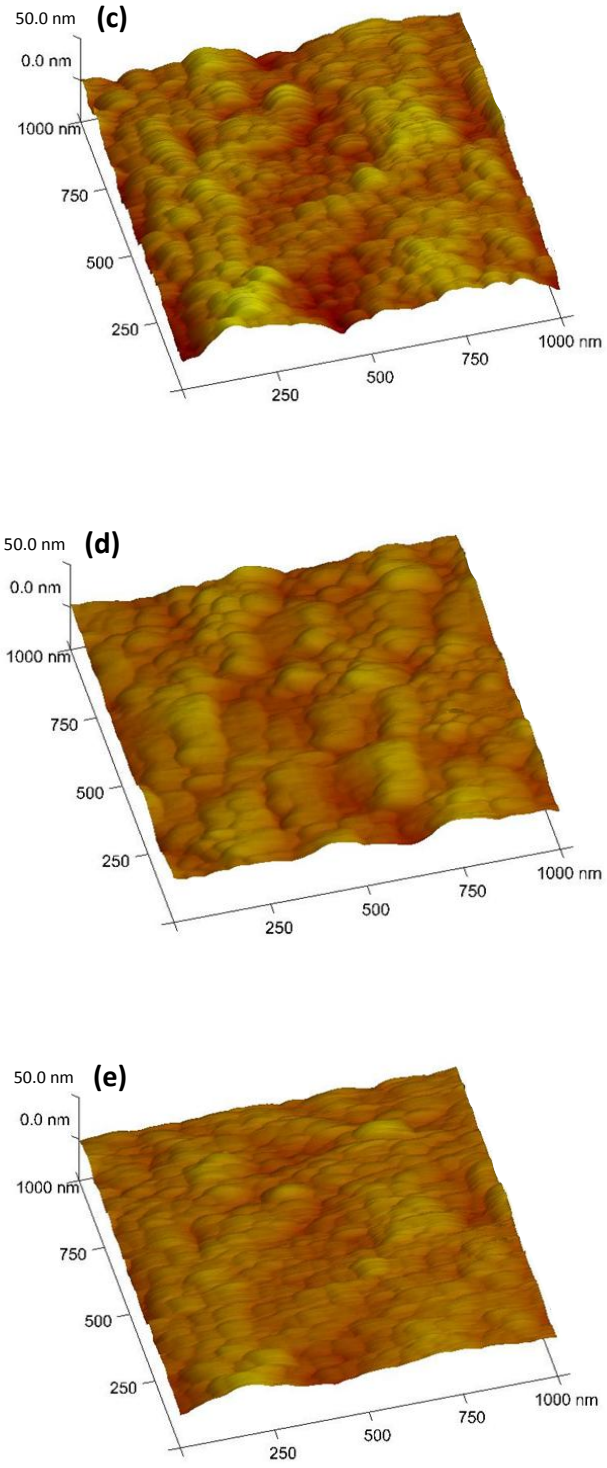

Figure 5-4 AFM images for (a) WO_3/Triton X-45, (b) WO_3/Triton X-100, (c) WO_3/Triton X-305, (d) WO_3/Triton X-405 and (e) WO_3/Triton X-705

In summary, the surfactant size had a deterministic influence on the particle size as well as the film morphology. Both film thickness and roughness showed a linear correlation, (R^2 > 0.95), with surfactant size (Figure 5-5). The underpinning mechanism can be explained schematically, as in Figure 5-6. During calcination, surfactants are adsorbed into the crystal surface and prevent the ions (W^{6+}, O^{2-}) from contacting the crystal surface. For the range of concentrations, > 10 CMC, the surfactant adsorption layer should be saturated immediately after nucleation. However, some ions, being smaller than surfactant head, can get through the spaces between the adsorbed surfactant. For the smaller surfactants, the spaces between adsorbed surfactants remain relatively large and thus allow more ions to pass through. Consequently, larger grains and thicker film are formed after nucleation. For large surfactants, in contrast, the spaces between adsorbed surfactants are smaller and, thus, less ions can pass though. As a result, the grains are smaller.

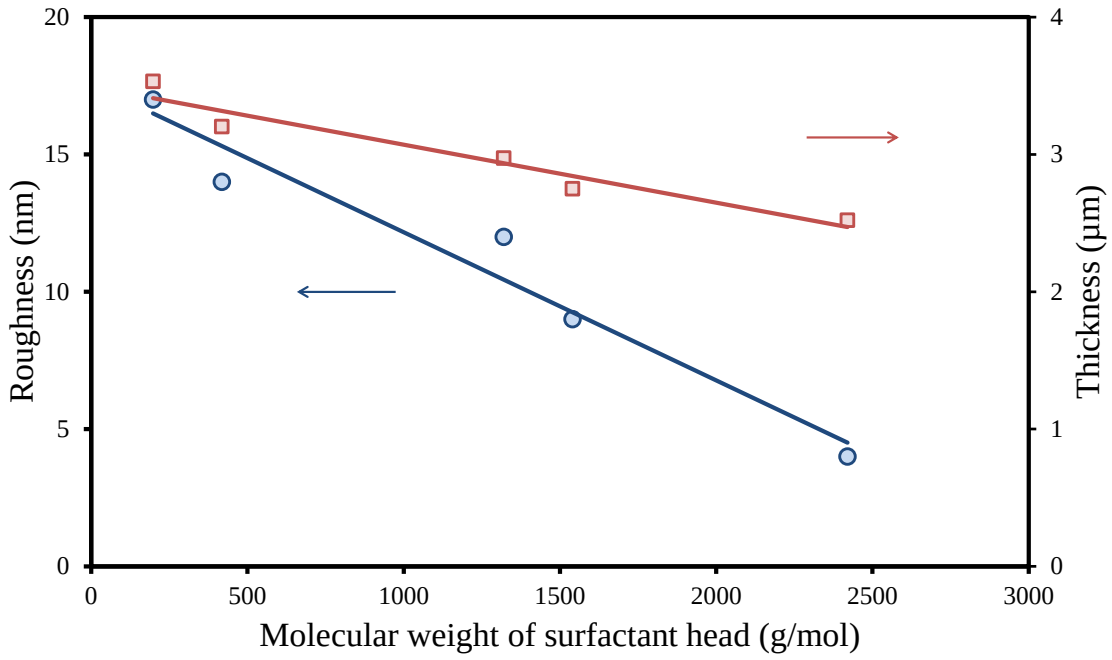

Figure 5-5 Influence of surfactants on the produced WO_3 films

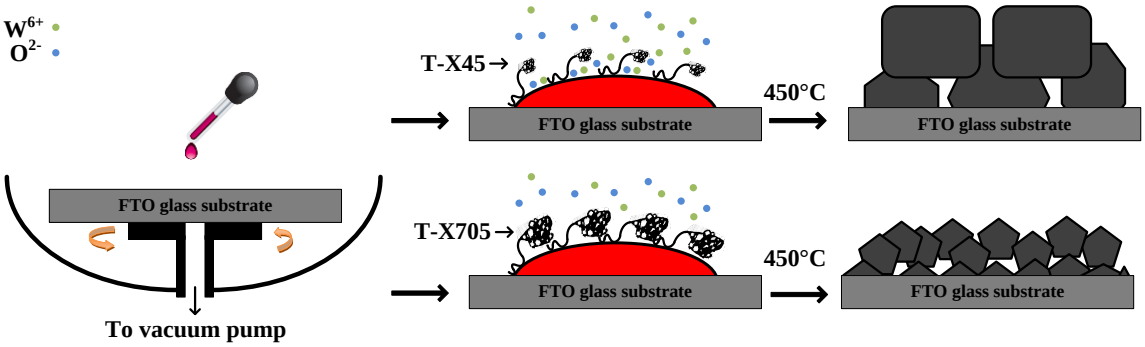

Figure 5-6 Schematic showing formation of different nanostructures

5.2.2. Optical characterization

Figure 5-7 shows the optical properties of the WO_3 films, which can be calculated by varying the absorption density, between 320 and 670 nm. The maximum solar absorption was observed in the ultraviolet and visible regions for the WO_3/Triton X-45 sample (532 A.U.). It is well known that the scattering efficiency of larger crystals is higher than that of smaller particles [8]. Consequently, the enhanced absorption of Triton X-45 corresponded to the increased crystallite size.

The band-gap of samples can be obtained from the absorption coefficient data, considering the solid band theory [116]:

$$(\alpha h\nu) = A\,(h\nu - E_g)^m \tag{5-3}$$

where α is the absorption coefficient, $h\nu$ is the energy of the incident photon, A is a constant related to the effective mass of the electrons and holes, E_g represents the energy band-gap of samples and $m = 2$ for indirect transition.

The band-gaps were obtained by the curve extrapolations (Figure 5-8). It can be seen that the energy increased slightly to 2.53 and 2.70 eV for the Triton X-45 and Triton X-705 samples, respectively. All of the samples started to absorb light between about 459 and 490 nm, which corresponds to a band-gap between 2.53 and 2.70 eV. The results (Table 5-4) were comparable to literature values [99, 120]. The obtained band-gaps were consistent with the optical absorption data, with Triton X-45 showing the smallest value.

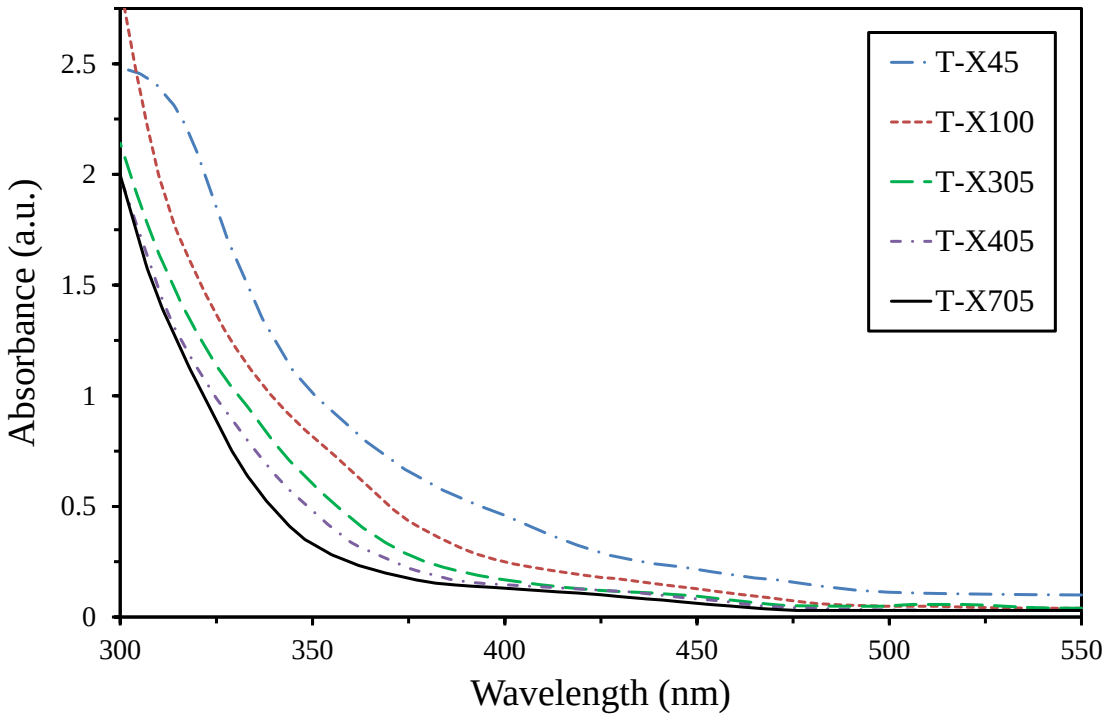

Figure 5-7 Absorption spectra of WO_3/Triton X-45, WO_3/Triton X-100, WO_3/Triton X-305, WO_3/Triton X-405 and WO_3/Triton X-705

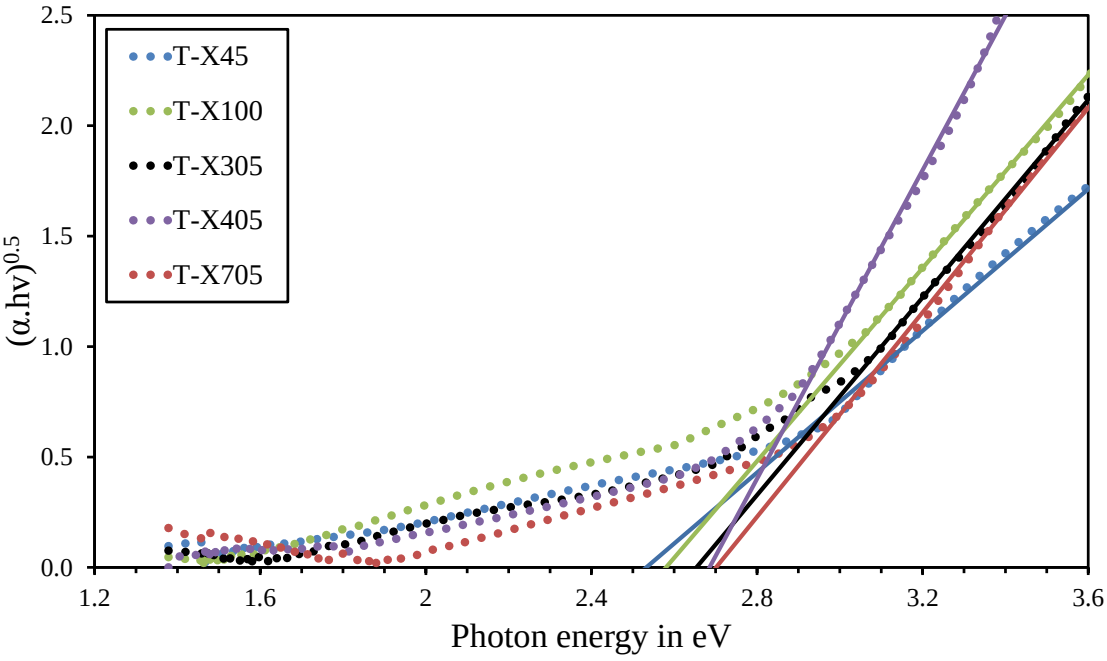

Figure 5-8 Calculation of the indirect electronic transition

5.2.3. Performance of the photoelectrochemical cell

The PEC measurements were performed under solar irradiation (100 mW cm^{-2}) to determine the photocurrent generation on the thin film surfaces (Figure 5-9). The photocurrent was obtained by subtracting the dark current from the light current at a given potential. The photocurrents demonstrated a clear correlation between surfactant size and photocatalytic activity. As can be seen from Figure 5-9, the obtained photocurrent increased from Triton X-705 through to Triton X-45 (i.e. the bigger the surfactant head, the lower was the current density). At 1.3 V/SCE, the photocurrent density of the Triton X-45-treated sample was 2.10 mA cm^{-2}, which was 70% higher than that of the Triton X-705-treated sample (Table 5-4). The high photocurrent density of Triton X-45 can be directly attributed to the improved grain size, which was a result of having a smaller hydrophobic head.

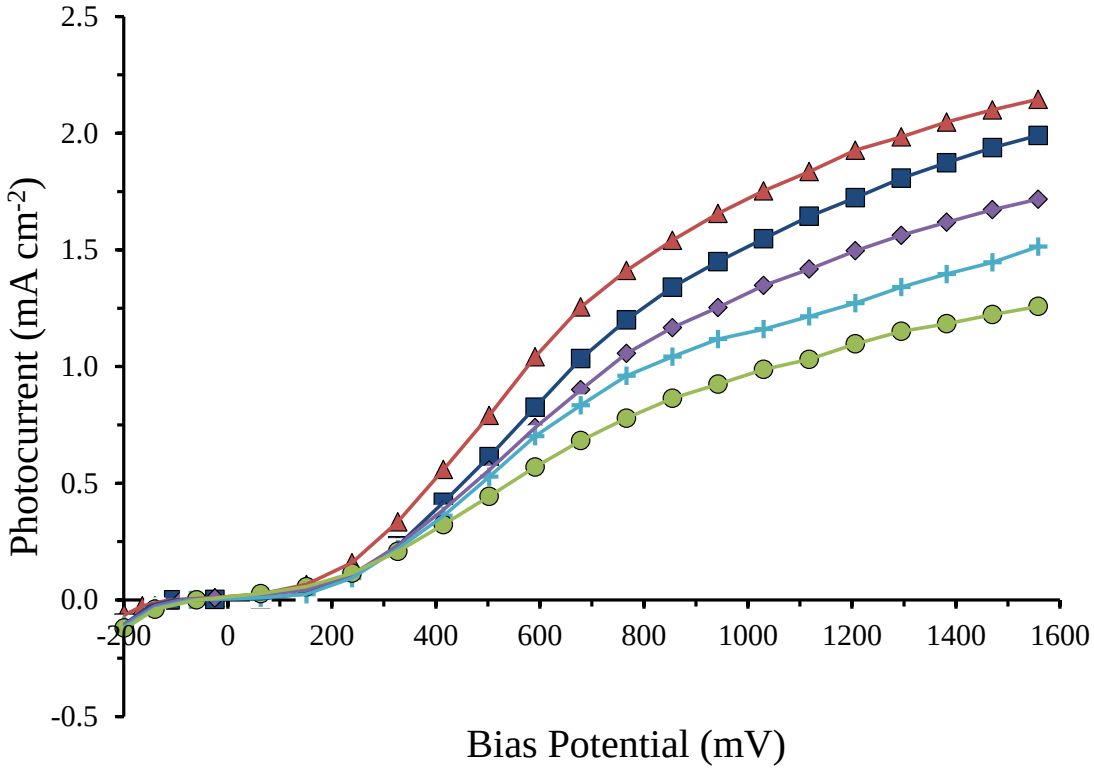

Figure 5-9 Photocurrent activity of WO_3/Triton X-45 (▲), WO_3/Triton X-100 (■), WO_3/Triton X-305 (♦), WO_3/Triton X-405 (+) and WO_3/Triton X-705 (●)

The onset potential values of WO_3 films, both in the dark and under simulated solar light (100 mW cm^{-2}), are shown in Figure 5-10. It was found that there is no significant difference between the onset potential in the dark or under light, which also is obvious from Figure 5-10. For comparison, the values are listed in Table 5-4. The onset potential of the Triton X-705 film (-0.062 V vs. Ag/AgCl) was about 50 mV higher than that of the Triton X-45 film (-0.112 V vs. Ag/AgCl).

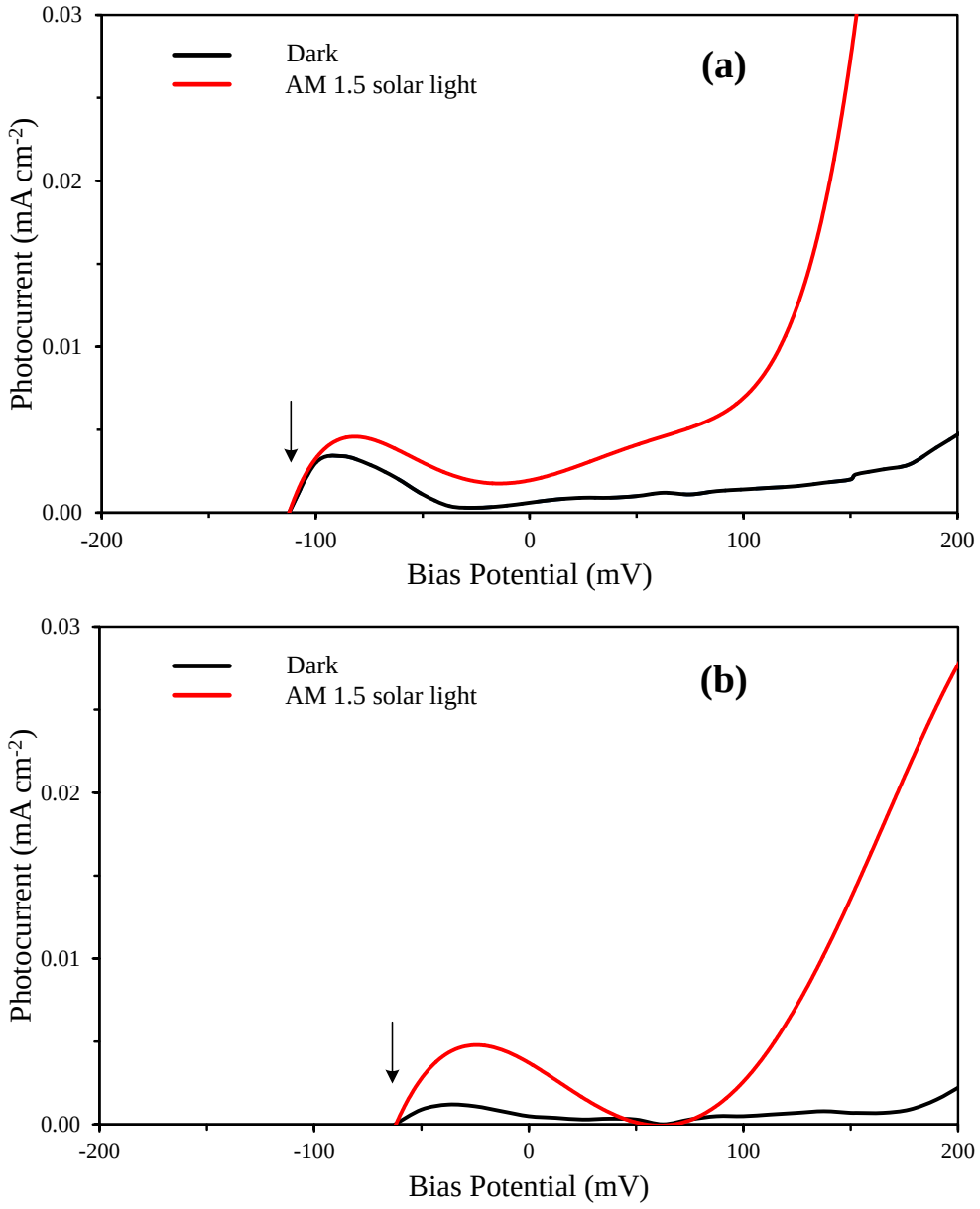

Figure 5-10 Values of the onset potential of (a) WO_3/Triton X-45 sample and (b) WO_3/Triton X-705 sample

The applied bias photon-to-current efficiency (ABPE) is one of the key parameters used to quantify a material's performance for PEC water splitting. The ABPE can be calculated from the photocurrent data using the following equation [27]:

$$\text{ABPE} = \left[\frac{J_{ph} \times (1.23 - |V_b|)}{P_{total}}\right] \quad (5\text{-}4)$$

where J_{ph} is the photocurrent density (mA cm^{-2}), P_{total} is the intensity of the incident light (mW cm^{-2}), V_b is the applied bias (eV) between the working and counter electrodes, to assist the water splitting reaction, and 1.23 eV is the Gibbs free energy for the water splitting reaction.

The maximum ABPE value was calculated for all the samples (Table 5-4). As shown in Figure 5-11, the Triton X-45 electrode exhibited 0.69 % ABPE at 0.68 V. It is noteworthy that the maximum ABPE obtained from the available literature was only 0.33 % at 0.82 V, for pristine tungsten oxide [125]. The efficiency of WO_3 was almost doubled by reducing the surfactant size from Triton X-705 down to Triton X-45.

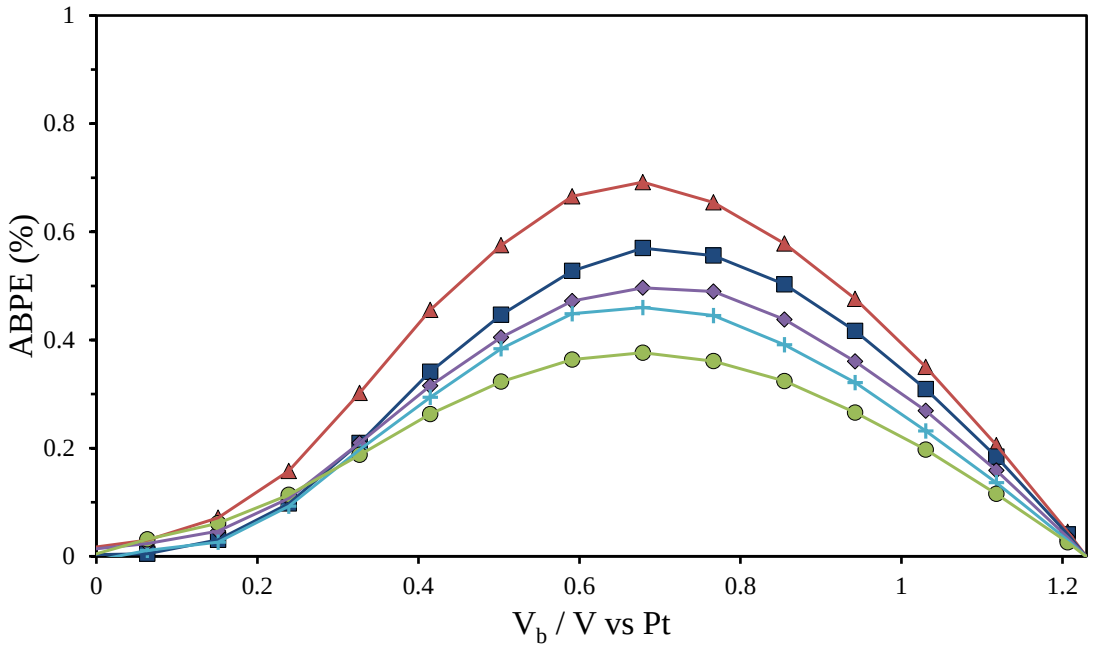

Figure 5-11 Applied bias photon-to-current efficiency (ABPE, %) as a function of applied potential, employing two electrodes of: WO_3/Triton X-45 (▲), WO_3/Triton X-100 (■), WO_3/Triton X-305 (♦), WO_3/Triton X-405 (+) and WO_3/Triton X-705 (●)

Table 5-4 Properties of WO_3 nanostructures

Surfactant	E_g (ev)	Absorption (A.U.) 320–670 nm	Onset potential V_{on} (V/SCE)	Photocurrent density (mA cm^{-2}) (at 1.3 V/SCE)	ABPE (%)
T-X45	2.53	532	-0.112	2.10	0.69
T-X100	2.59	473	-0.104	1.93	0.57
T-X305	2.65	346	-0.088	1.67	0.50
T-X405	2.69	263	-0.071	1.44	0.46
T-X705	2.70	225	-0.062	1.22	0.38

The effects of crystal size on photoactivity behaviour have been verified previously [8, 48]. Upon absorption of light, the electron-hole pairs are generated in the semiconductor. The produced electron-hole pairs must be effectively separated for reduction and oxidation reactions, respectively. In the case of a WO_3 photoanode, the hole diffusion length (L_h) can be estimated to be $\sim$ 150 nm [124, 126]. Since all samples had a grain size < L_h, the generated holes could reach to the electrode/electrolyte interface with minimum recombination, resulting in strong photoactivity behaviour [124]. If the grain size is too small, however, a greater grain boundary can be produced within the film. Thus, a higher number of volume recombinations can occur during the electron migration. Consequently, the Triton X-45 sample, with the grain size closest to 150 nm, demonstrated the highest photoactivity. A schematic diagram of the mechanism of charge separation and photocatalytic reaction in a photoelectrochemical system is presented in Figure 5-12.

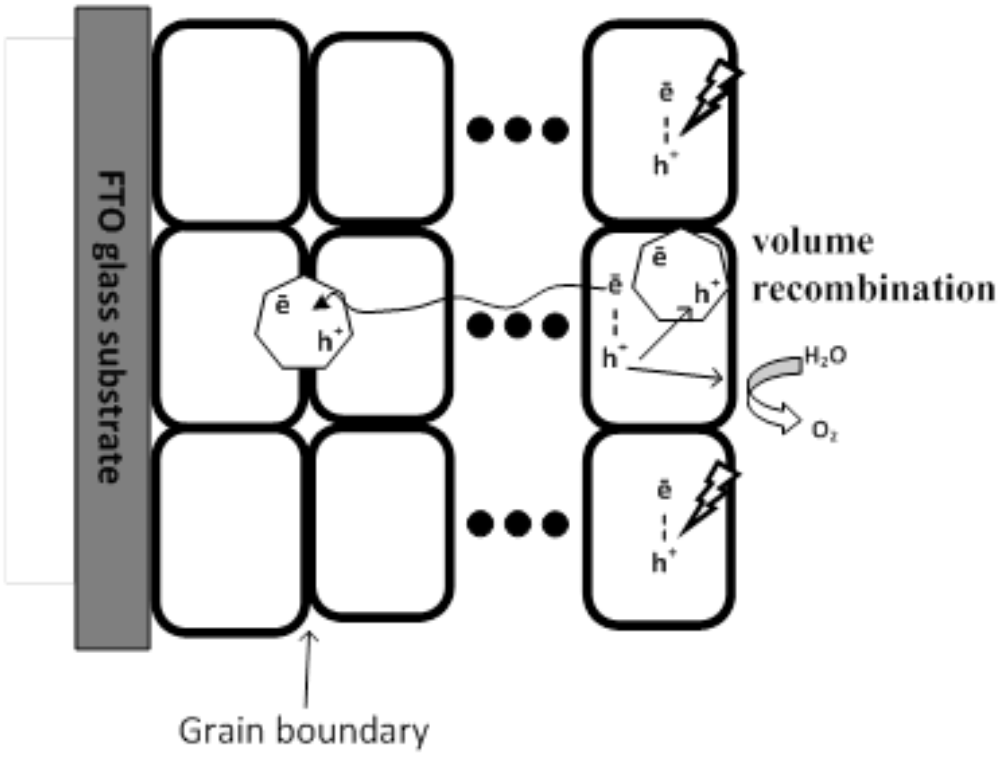

Figure 5-12 Mechanism of charge separation during the PEC water splitting reaction

5.3. Controlling particle size of WO_3 nanoparticles with Triton surfactant

In section 5-2-1, we have presented the procedure to synthesise WO_3 nanostructured material in the range of 75 - 124 nm. A series of different Triton surfactants (Triton X-45, Triton X-100, Triton X-305, Triton X-405 and Triton X-705) was used in the synthesis procedure. As can be seen in Figure 5-13, with increasing molecular weight of the Triton surfactant, the characterized size of WO_3 nanoparticles decreased. An empirical equation was used to model the behaviour of WO_3 nanoparticles:

$$\frac{D}{D_0} = \frac{1+ C_0\, M}{C_0\, M} \tag{5-5}$$

where D is the particle size, D_0 is the critical particle size, C_0 is constant and M is the molecular weight of the surfactant head.

The best-fit values of D_0 and C_0 (D_0 = 77 nm, C_0 = 0.006) were obtained by fitting equation (5-5) to the experimental data. As Figure 5-13 clearly shows, the particle size

decreased with increasing molecular weight of the surfactant head (*M*). However, there is a theoretical limitation, viz., critical particle size (D_0) at 77 nm. The practical limit, by contrast, should be around 80 nm for Triton surfactants.

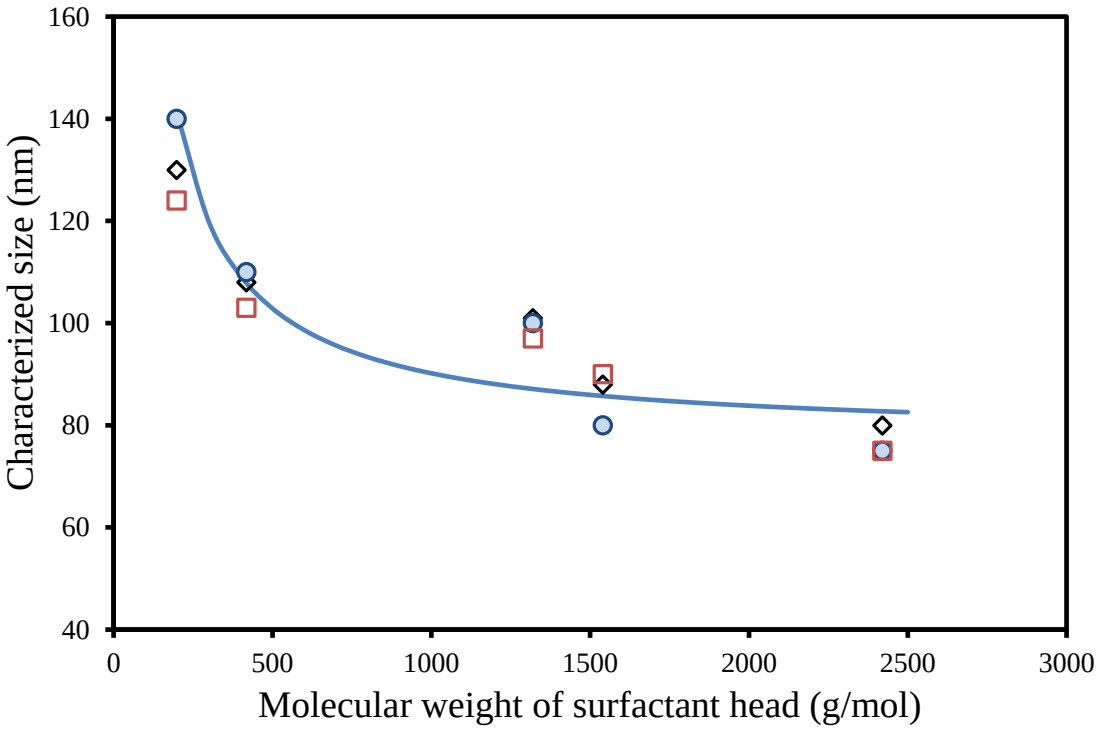

Figure 5-13 Fitted empirical equation for determination of the characterized size and actual values obtained from XRD □, SEM ○ and BET ◊ versus molecular weight of Triton surfactants

5.4. Proposed mechanism for relationship between surfactant structure and WO_3 film

In this section, a model is developed, based on the characterized sizes (particle size, grain size and crystallite size) of WO_3 nanoparticles, using different series of Triton surfactants. Having this model will help to predict results and manipulate the sizes of WO_3 nanoparticles treated with Triton surfactants.

In Chapter 2 (Section 2.2.2), a correlation was shown between surfactant structure and the synthesized nanoparticles based on two different methods: namely, adsorption density of the surfactant and the vacant spaces between the surfactant particles. In this

section, these equations are expanded further to find the correlation between surfactant adsorption time, molecular weight of surfactants and characterized size of nanoparticles.

5.4.1. Adsorption density of Triton surfactant

The presented equation in chapter 2 (equation 2-3) can be used to describe the growth of individual crystals of average particle diameter, *D*, dispersed in a homogeneous matrix:

$$D = D_0 + k\, t_{eff}^{1/2} \tag{2-3}$$

By rearranging equation 5-5, *D* can be calculated as:

$$D = D_0 + \frac{D_0}{C_0\, M} \tag{5-6}$$

Therefore, comparing equation 2-3 and 5-6 will provide us with:

$$k\, t_{eff}^{1/2} = \frac{D_0}{C_0\, M} \tag{5-7}$$

Thus, t_{eff} can be calculated as:

$$t_{eff} = \left(\frac{D_0}{C_0\, M\, k}\right)^2 \tag{5-8}$$

As it can be clearly understood from equation (5-8), $t_{eff} = \left(\frac{A_1}{M}\right)^2$ (A_1 is constant). Therefore, the adsorption time of the surfactant has an inverse relationship with the molecular weight of the surfactant, and there is a direct correlation with the characterized size of the nanoparticles. These results are consistent with experimental data and prove the obtained data on characterization size of WO_3 nanoparticles using Triton surfactant.

5.4.2. Vacant space between Triton surfactant

Equation 2-4 can be utilized to find the relationship between the vacant space between Triton surfactant (C_p) and the characterized size of the nanoparticles, thus:

$$D = D_0 + k\, C_p\, t_{eff}^{1/2} \tag{2-4}$$

Applying equation (5-7) into equation (2-4), we would have:

$$D = D_0 + \frac{D_0 C_p}{C_0 M} \tag{5-9}$$

Moreover, calculating C_p would provide us with the following equation (A_2 is constant):

$$C_p = \frac{1}{A_2 M} \tag{5-10}$$

Therefore, from equations (5-9) and (5-10) it can be conclude that, with increasing vacant position between each pair of surfactant characterized size of WO_3 nanoparticle would be increased. Also, molecular weight of Triton surfactant has an inverse relationship with the vacant position of Triton surfactant. Moreover, these correlations are consistent with the obtained experimental results for the WO_3 nanoparticles. The influence of vacant space between Triton surfactant on characterized size of WO_3 nanoparticle is presented in Figure 5-14 schematically. During calcination, surfactants are adsorbed into the crystal surface and prevent the ions (W^{6+}, O^{2-}) from contacting the crystal surface. For the range of concentrations, > 10 CMC, the surfactant adsorption layer should be saturated immediately after nucleation. However, some ions, being smaller than surfactant head, can get through the spaces between the adsorbed surfactant. For the smaller surfactants, the spaces between adsorbed surfactants remain relatively large and thus allow more ions to pass through. Consequently, larger grains and thicker film are formed after nucleation. For large surfactants, in contrast, the spaces between adsorbed surfactants are smaller and, thus, less ions can pass though. As a result, the grains are smaller.

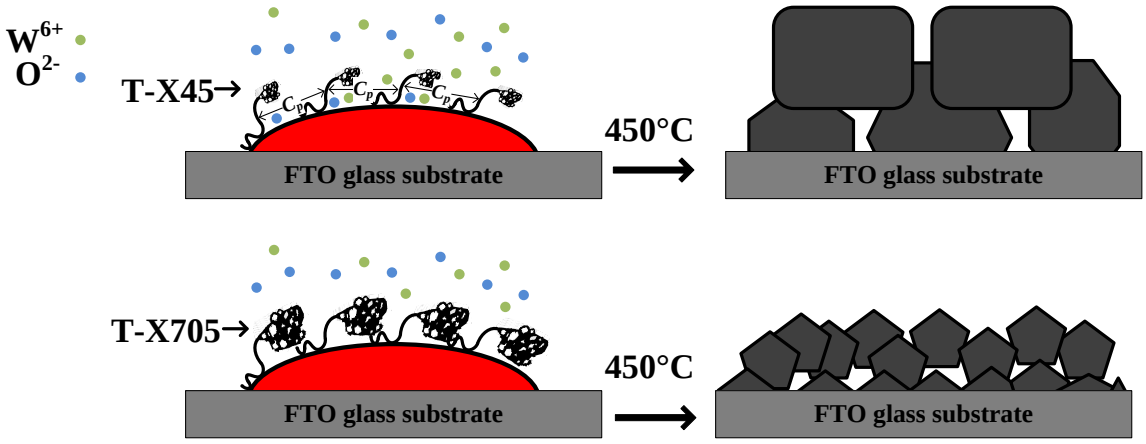

Figure 5-14 Influence of vacant space between Triton surfactant on characterized size of WO_3 nanoparticle

5.5. Conclusions

Nanostructured crystalline WO_3 films were prepared using a peroxotungstic acid precursor. The addition of surfactants (Triton X-45, Triton X-100, Triton X-305, Triton X-405 and Triton X-705) was used as the structural template. Physical properties (measured via XRD, SEM, BET and AFM) showed deterministic correlations with surfactant size. Also, the correlation between produced particle size and original surfactant size was presented. Additionally, the film thickness and roughness were linearly correlated to the surfactant size. The photoelectrochemical properties of the synthesized films also were correlated with the surfactant size. Triton X-45 revealed the best performance: the highest current density, smallest band-gap (2.53 eV) and highest absorption (532 A.U.). The WO_3/Triton X-45 sample also showed the highest efficiency, with an ABPE of 0.69 %, and the highest solar absorption in the ultraviolet and visible regions.

Most notably, the correlation between produced particle and surfactant size followed a monotonic equation $\frac{D}{D_0} = \frac{1+ C_0 M}{C_0 M}$ when they have been treated with Triton surfactants. The best-fit values of D_0 and C_0 (D_0 = 77 nm, C_0 = 0.006) were obtained by fitting the empirical equation to experimental data.

For the investigated systems, the largest grain size, which was obtained with the smallest surfactant particle size, produced the best PEC performance. The results highlighted the significance of surfactant size on the calcination process and the produced anodes. In addition to water splitting, the findings have important implications for other applications in which a precise control of the metal oxide grain size is desirable.

6. CONCLUSIONS AND RECOMMENDATIONS

6.1. Conclusions

Fe_2O_3 nanostructured photoanodes were prepared, via a sol-gel spin coating method, using fluorine-doped tin oxide glass substrates with six different surfactants: polyethylene glycol (PEG-300), Triton X-100, pluronic F127, cetyl trimethyl ammonium bromide (CTAB), octadecyl trimethyl ammonium bromide (OTAB) and tetradecyl trimethyl ammonium bromide (TTAB). The resulting films had thicknesses ranging from 520 $\pm$ 10 to 980 $\pm$ 10 nm, after calcination at 450 °C in the air. A comparative study of the photocatalytic activity of thin films was performed. The photogeneration of the samples was determined by measuring the currents and voltages under illumination by UV-vis light. The highest photocurrent density of 1.77 mA/cm^2 at 1 V/SCE, under an illumination intensity of 100 mW cm^{-2} from a solar simulator with a global AM 1.5 filter, was produced by the TTAB-treated sample. The optical properties, morphology, surface roughness and structure of the films were characterized by UV-visible spectroscopy, SEM, AFM and XRD. The results are consistent with the photocatalytic performance: the TTAB-treated sample produced the highest values for both grain size and optical absorption. The improved performance of this sample can be attributed to the crystallization process of TTAB, which leads to the larger grain size and highest photocatalytic activity.

The study demonstrates that the photoelectrochemical performance of a metal oxide can be improved by simply changing the surfactant. The results highlighted the superior performance of cationic surfactants over non-ionic surfactants in preparing Fe_2O_3 photoanodes via the sol-gel method. Moreover, the study showed that decreasing the size of the hydrocarbon tail of cationic surfactants can increase the film's crystallite size and improve its photocatalytic activity.

Also in this study, tungsten trioxide films have been prepared via the sol-gel method, using peroxotungstic acid (PTA) as the precursor sol and with different surfactants: anionic sodium dodecyl sulphate (SDS) and non-ionic Triton X-n, (with n = 45, 100,

305, 405, 705). The physical and photoelectrochemical (PEC) properties of the synthesized nanocrystalline films also were studied. The PEC experiments were performed by measuring the currents and voltages obtained under illumination by UV-vis light. The highest photocurrent density of 2.10 mA cm^{-2} at 1.3 V/SCE, under an illumination intensity of 100 mW cm^{-2}, was produced by the Triton X-45-treated sample. The optical properties, morphology, surface roughness and crystalline structure of the films were characterized by UV-visible spectroscopy, SEM, AFM and XRD, respectively. The results highlighted a clear relationship between the sizes of surfactant heads, grains and crystallites. Also, the thickness of samples is influenced by surfactant size (with smaller surfactant size producing thicker film). Consequently, the photocatalytic activity of the photoanode was investigated and found to be related to the grain size. Results showed that the Triton X-45 sample had the largest grain size and highest optical absorption. The improved performance of this sample can be attributed to the size of the surfactant, which leads to formation of the larger grain size during the calcination process and the highest photocatalytic activity. Results suggested a simple method to control the grain size and performance of WO_3 anodes.

Furthermore, two different models were obtained to predict the behaviour of Fe_2O_3 and WO_3 nanoparticles when they are treated with cationic and Triton surfactants. These models have been developed to control the overall particle size by varying surfactant size. Also, the effect of adsorption time on the particle size of nanoparticles was presented.

6.2. Recommendations

This study explores the influences of surfactants on the photocatalytic activity of different photocatalysts. Ultimately, the study quantifies an economical and routine pathway to improve the efficiency and stability of photoelectrodes for photoelectrochemical water splitting applications.

The following recommendations are offered for related research:

- Performance of the developed nanostructured electrodes for water splitting and hydrogen generation should be verified experimentally in a photoelectrochemical water splitting photoreactor.
- In order to confirm the presented theory on relation between surfactant size (either head or tail) and characterized size of nanoparticles, this theory can be applied to other metal oxide nanoparticles.
- Effects of annealing temperature and time on characterized size of surfactant assisted nanoparticles can be modelled and compared with the obtained data from this study.
- The present method can be combined with, and complements, other methods, i.e. doping, mixing and multilayering, to achieve the desirable properties. The method can be extended to other applications in addition to water splitting.

References:

1. Mu, Y., et al., *Biological hydrogen production by anaerobic sludge at various temperatures.* International Journal of Hydrogen Energy, 2006. **31**(6): p. 780-785.

2. *Australia Energy Information Administration (eia), 2012 Annual Energy Review*. Available from: http://www.eia.gov/countries/cab.cfm?fips=AS#note.

3. Twidell, J. and T. Weir, *Renewable energy resources*. 2003: Taylor & Francis.

4. Yilanci, A., I. Dincer, and H. Ozturk, *A review on solar-hydrogen/fuel cell hybrid energy systems for stationary applications.* Progress in Energy and Combustion Science, 2009. **35**(3): p. 231-244.

5. Grätzel, M., *Solar energy conversion by dye-sensitized photovoltaic cells.* Inorganic Chemistry, 2005. **44**(20): p. 6841-6851.

6. Hasobe, T., et al., *Enhancement of light-energy conversion efficiency by multi-porphyrin arrays of porphyrin-peptide oligomers with fullerene clusters.* The Journal of Physical Chemistry B, 2005. **109**(1): p. 19-23.

7. Zheng, X.-J., et al., *Research on photocatalytic H_2 production from acetic acid solution by Pt/TiO_2 nanoparticles under UV irradiation.* International Journal of Hydrogen Energy, 2009. **34**(22): p. 9033-9041.

8. Memar, A., C.M. Phan, and M.O. Tade, *Influence of surfactants on Fe_2O_3 nanostructure photoanode.* International Journal of Hydrogen Energy, 2012.

9. Boudjemaa, A., et al., *Physical and photo-electrochemical characterizations of α-Fe_2O_3. Application for hydrogen production.* International Journal of Hydrogen Energy, 2009. **34**(10): p. 4268-4274.

10. Rajeshwar, K., R.D. McConnell, and S. Licht, *Solar hydrogen generation: toward a renewable energy future*. 2008: Springer Science+ Business Media.

11. Tromp, T.K., et al., *Potential environmental impact of a hydrogen economy on the stratosphere.* Science, 2003. **300**(5626): p. 1740-1742.

12. Elam, C.C. and R.J. Evans, *Overview of hydrogen production.* Prepared Paper-American Chemical Society, Division of Fuel Chemistry, 2004. **49**(2): p. 481-482.

13. Bak, T., et al., *Photo-electrochemical hydrogen generation from water using solar energy. Materials-related aspects.* International Journal of Hydrogen Energy, 2002. **27**(10): p. 991-1022.

14. Nowotny, J., et al., *Solar-hydrogen: Environmentally safe fuel for the future.* International Journal of Hydrogen Energy, 2005. **30**(5): p. 521-544.

15. Chakraborty, J., *The geographic distribution of potential risks posed by industrial toxic emissions in the US.* Journal of Environmental Science and Health, Part A, 2004. **39**(3): p. 559-575.

16. Kim, A., *The current state of the earth's climate and the future effects of global warming.* Asia's Emerging Nuclear Era: p. 21.

17. Fujishima, A., *Electrochemical photolysis of water at a semiconductor electrode.* Nature, 1972. **238**: p. 37-38.

18. Ni, M., et al., *A review and recent developments in photocatalytic water-splitting using TiO_2 for hydrogen production.* Renewable and Sustainable Energy Reviews, 2007. **11**(3): p. 401-425.

19. Fazleev, N., *Surface states and annihilation characteristics of positrons trapped at reconstructed semiconductor surfaces.* Applied surface science, 2006. **252**(9): p. 3333-3341.

20. Nakata, S., et al., *Characteristic nonlinear responses for gas species on the surface of different semiconductor gas sensors.* Applied surface science, 1998. **135**(1): p. 285-292.

21. VAN SON, N., et al., *Influence of cluster size and surface functionalization of ZnO nanoparticles on the morphology, thermo-mechanical and piezoelectric properties of P (VDF-TrFE) nanocomposite films.* Applied surface science, 2013. **279**: p. 204-211.

22. Pileni, M.-P., *The role of soft colloidal templates in controlling the size and shape of inorganic nanocrystals.* Nature materials, 2003. **2**(3): p. 145-150.

23. Zhuo, Y., et al., *Surfactant-assisted synthesis of Ag nanostructures and their self-assembled films on copper and aluminum substrate.* Applied Surface Science, 2011. **257**(24): p. 10395-10401.

24. Minggu, L.J., W.R. Wan Daud, and M.B. Kassim, *An overview of photocells and photoreactors for photoelectrochemical water splitting.* International Journal of Hydrogen Energy, 2010. **35**(11): p. 5233-5244.

25. Butler, M. and D. Ginley, *Principles of photoelectrochemical, solar energy conversion.* Journal of Materials Science, 1980. **15**(1): p. 1-19.

26. Glasscock, J., et al., *Structural, optical and electrical properties of undoped polycrystalline hematite thin films produced using filtered arc deposition.* Thin Solid Films, 2008. **516**(8): p. 1716-1724.

27. Chen, Z., et al., *Accelerating materials development for photoelectrochemical hydrogen production: Standards for methods, definitions, and reporting protocols.* Journal of Materials Research 2010. **25**(1): p. 3.

28. van de Krol, R., Y. Liang, and J. Schoonman, *Solar hydrogen production with nanostructured metal oxides.* Journal of Materials Chemistry, 2008. **18**(20): p. 2311-2320.

29. Glasscock, J.A., *Nanostructured materials for photoelectrochemical hydrogen production using sunlight*, 2008, University of New South Wales.

30. Chandra, N., B.L. Wheeler, and A.J. Bard, *Photocurrent efficiencies at p-indium phosphide electrodes in aqueous solutions.* The Journal of Physical Chemistry, 1985. **89**(23): p. 5037-5040.

31. Nozik, A., *p-n photoelectrolysis cells.* Applied Physics Letters, 1976. **29**(3): p. 150-153.

32. Bolton, J.R., *Solar photoproduction of hydrogen: a review.* Solar Energy, 1996. **57**(1): p. 37-50.

33. Grimes, C.A., O.K. Varghese, and S. Ranjan, *Light, water, hydrogen: the solar generation of hydrogen by water photoelectrolysis*. 2008: Springer.

34. Grätzel, M., *Photoelectrochemical cells.* Nature, 2001. **414**(6861): p. 338-344.

35. Miller, E.L., et al., *Development of reactively sputtered metal oxide films for hydrogen-producing hybrid multijunction photoelectrodes.* Solar Energy Materials and Solar Cells, 2005. **88**(2): p. 131-144.

36. Miller, E., R. Rocheleau, and X. Deng, *Design considerations for a hybrid amorphous silicon/photoelectrochemical multijunction cell for hydrogen production.* International Journal of Hydrogen Energy, 2003. **28**(6): p. 615-623.

37. Bohra, M., et al., *RF Sputter Deposited Nanocrystalline (110) Magnetite Thin Film from Fe_2O_3 Target.* Journal of Nanoscience and Nanotechnology, 2007. **7**(6): p. 2055-2057.

38. Tjong, S. and H. Chen, *Nanocrystalline materials and coatings.* Materials Science and Engineering: R: Reports, 2004. **45**(1): p. 1-88.

39. Khaselev, O., A. Bansal, and J. Turner, *High-efficiency integrated multijunction photovoltaic/electrolysis systems for hydrogen production.* International Journal of Hydrogen Energy, 2001. **26**(2): p. 127-132.

40. Licht, S., et al., *Over 18% solar energy conversion to generation of hydrogen fuel; theory and experiment for efficient solar water splitting.* International Journal of Hydrogen Energy, 2001. **26**(7): p. 653-659.

41. Solarska, R., B.D. Alexander, and J. Augustynski, *Electrochromic and photoelectrochemical characteristics of nanostructured WO_3 films prepared by a sol–gel method.* Comptes Rendus Chimie, 2006. **9**(2): p. 301-306.

42. Sun, Y., et al., *Photoelectrochemical and structural characterization of carbon-doped WO_3 films prepared via spray pyrolysis.* International Journal of Hydrogen Energy, 2009. **34**(20): p. 8476-8484.

43. Luo, W., et al., *Enhanced photocurrent–voltage characteristics of WO_3/Fe_2O_3 nano-electrodes.* Journal of Physics D: Applied Physics, 2007. **40**(4): p. 1091.

44. Tomkiewicz, M. and J.M. Woodall, *Photoelectrolysis of water with semiconductor materials.* Journal of The Electrochemical Society, 1977. **124**(9): p. 1436-1440.

45. Kohl, P.A., S.N. Frank, and A.J. Bard, *Semiconductor Electrodes XI. Behavior of n-and p-Type Single Crystal Semconductors Covered with Thin Films.* Journal of The Electrochemical Society, 1977. **124**(2): p. 225-229.

46. Wheeler, D.A., et al., *Nanostructured hematite: synthesis, characterization, charge carrier dynamics, and photoelectrochemical properties.* Energy & Environmental Science, 2012. **5**(5): p. 6682-6702.

47. Rahimnejad, M., et al., *Synthesis, characterization and application studies of self-made Fe_3O_4/PES nanocomposite membranes in microbial fuel cell.* Electrochimica Acta, 2011.

48. Memar, A., et al., *Study on photocurrent of bilayers photoanodes using different combination of WO_3 and Fe_2O_3.* Solar Energy, 2010. **84**(8): p. 1538-1544.

49. Ghasemi, M., et al., *New generation of carbon nanocomposite proton exchange membranes in microbial fuel cell systems.* Chemical Engineering Journal, 2012. **184**: p. 82-89.

50. Miyake, H. and H. Kozuka, *Photoelectrochemical properties of Fe_2O_3-Nb_2O_5 films prepared by sol-gel method.* The Journal of Physical Chemistry B, 2005. **109**(38): p. 17951-17956.

51. Ghasemi, M., et al., *Activated carbon nanofibers as an alternative cathode catalyst to platinum in a two-chamber microbial fuel cell.* International Journal of Hydrogen Energy, 2011. **36**(21): p. 13746-13752.

52. Zhang, Y., et al., *Structural and electrochromic properties of tungsten oxide prepared by surfactant-assisted process.* Solar Energy Materials and Solar Cells, 2009. **93**(8): p. 1338-1344.

53. Liu, J., et al., *Effect of surfactants on the structure and photoelectric properties of ITO films by sol-gel method.* Rare Metals, 2010. **29**(2): p. 143-148.

54. Shahi, A.K., et al., *Surfactant assisted surface studies of zinc sulfide nanoparticles.* Applied Surface Science, 2011. **257**(23): p. 9846-9851.

55. Kandel, D. and E. Kaxiras, *The surfactant effect in semiconductor thin-film growth.* Solid State Physics, 1999. **54**: p. 219-262.

56. Guo, J., et al., *Influence of temperature on structure as well as adhesion and friction and wear behavior of hydrogenated carbon nitride films prepared on silicon substrate.* Applied Surface Science, 2011. **258**(2): p. 791-799.

57. Suriye, K., P. Praserthdam, and B. Jongsomjit, *Control of Ti^{3+} surface defect on TiO_2 nanocrystal using various calcination atmospheres as the first step for surface defect creation and its application in photocatalysis.* Applied Surface Science, 2007. **253**(8): p. 3849-3855.

58. Asim, N., S. Radiman, and M.b. Yarmo, *Preparation of WO_3 Nanoparticles Using Cetyl Trimethyl Ammonium Bromide Supermolecular Template.* American Journal of Applied Sciences, 2009. **6**(7): p. 1422-1426.

59. Baeck, S.H., et al., *Enhancement of photocatalytic and electrochromic properties of electrochemically fabricated mesoporous WO_3 thin films.* Advanced Materials, 2003. **15**(15): p. 1269-1273.

60. Naseri, N., et al., *Photoresponse and H_2 production of topographically controlled PEG assisted Sol–gel WO_3 nanocrystalline thin films.* International Journal of Hydrogen Energy, 2011. **36**(21): p. 13461-13472.

61. Dare-Edwards, M.P., et al., *Electrochemistry and photoelectrochemistry of iron (III) oxide.* J. Chem. Soc., Faraday Trans. 1, 1983. **79**(9): p. 2027-2041.

62. Kennedy, J.H. and K.W. Frese, *Photooxidation of Water at α-Fe_2O_3 Electrodes.* Journal of the Electrochemical Society, 1978. **125**(5): p. 709-714.

63. Bjoerksten, U., J. Moser, and M. Graetzel, *Photoelectrochemical studies on nanocrystalline hematite films.* Chemistry of materials, 1994. **6**(6): p. 858-863.

64. Teng, X. and H. Yang, *Effects of surfactants and synthetic conditions on the sizes and self-assembly of monodisperse iron oxide nanoparticles.* Journal of Materials Chemistry, 2004. **14**(4): p. 774-779.

65. Butler, M., *Photoelectrolysis and physical properties of the semiconducting electrode WO.* Journal of Applied Physics, 1977. **48**: p. 1914.

66. Asim, N., S. Radiman, and M.b. Yarmo, *Synthesis of WO_3 in nanoscale with the usage of sucrose ester microemulsion and CTAB micelle solution.* Materials Letters, 2007. **61**(13): p. 2652-2657.

67. Deepa, M., A. Srivastava, and S. Agnihotry, *Influence of annealing on electrochromic performance of template assisted, electrochemically grown, nanostructured assembly of tungsten oxide.* Acta materialia, 2006. **54**(17): p. 4583-4595.

68. Lai, W., et al., *Effect of copolymer and additive concentrations on the behaviors of mesoporous tungsten oxide.* Journal of alloys and compounds, 2005. **396**(1): p. 295-301.

69. Huang, F., H. Zhang, and J.F. Banfield, *Two-stage crystal-growth kinetics observed during hydrothermal coarsening of nanocrystalline ZnS.* Nano Letters, 2003. **3**(3): p. 373-378.

70. Kirchner, H., *Coarsening of grain-boundary precipitates.* Metallurgical Transactions, 1971. **2**(10): p. 2861-2864.

71. Speight, M., *Growth kinetics of grain-boundary precipitates.* Acta Metallurgica, 1968. **16**(1): p. 133-135.

72. Wagner, C., *Theory of precipitate change by redissolution.* Z. Electrochem, 1961. **65**(7-8): p. 581-591.

73. Kittel, C. and B.C. Kittel, *Introduction to solid state physics.* 1986.

74. Thursfield, A., et al., *Defect Chemistry and Transport in Metal Oxides.* CHEMICAL INDUSTRIES-NEW YORK-MARCEL DEKKER-, 2006. **108**: p. 55.

75. Rothenberger, G., et al., *Charge carrier trapping and recombination dynamics in small semiconductor particles.* Journal of the American Chemical Society, 1985. **107**(26): p. 8054-8059.

76. Kee, C.-S. and H. Lim, *Tunable complete photonic band gaps of two-dimensional photonic crystals with intrinsic semiconductor rods.* Physical Review B, 2001. **64**(12): p. 121103.

77. Morrison, S.R., *Electrochemistry at semiconductor and oxidized metal electrodes.* 1980.

78. Jonker, G., *Analysis of the semiconducting properties of cobalt ferrite.* Journal of Physics and Chemistry of Solids, 1959. **9**(2): p. 165-175.

79. Augustynski, J., *The role of the surface intermediates in the photoelectrochemical behaviour of anatase and rutile TiO_2.* Electrochimica Acta, 1993. **38**(1): p. 43-46.

80. Licht, S., et al., *Fullerene photoelectrochemical solar cells.* Solar Energy Materials and Solar Cells, 1998. **51**(1): p. 9-19.

81. Khaselev, O. and J.A. Turner, *A monolithic photovoltaic-photoelectrochemical device for hydrogen production via water splitting.* science, 1998. **280**(5362): p. 425-427.

82. Abe, R., *Recent progress on photocatalytic and photoelectrochemical water splitting under visible light irradiation.* Journal of Photochemistry and Photobiology C: Photochemistry Reviews, 2010. **11**(4): p. 179-209.

83. Janai, M., et al., *Optical properties and structure of amorphous silicon films prepared by CVD.* Solar Energy Materials, 1979. **1**(1): p. 11-27.

84. Murphy, A., et al., *Efficiency of solar water splitting using semiconductor electrodes.* International Journal of Hydrogen Energy, 2006. **31**(14): p. 1999-2017.

85. Markvart, T., *Solar electricity*. 2000: John Wiley & Sons.

86. Bird, R.E., R.L. Hulstrom, and L. Lewis, *Terrestrial solar spectral data sets.* Solar Energy, 1983. **30**(6): p. 563-573.

87. Dare-Edwards, M.P., et al., *Electrochemistry and photoelectrochemistry of iron (III) oxide.* Journal of the Chemical Society, 1983. **79**(9): p. 2027-2041.

88. Brillet, J., M. Gratzel, and K. Sivula, *Decoupling feature size and functionality in solution-processed, porous hematite electrodes for solar water splitting.* Nano letters, 2010. **10**(10): p. 4155-4160.

89. Aroutiounian, V., et al., *Photoelectrochemistry of tin-doped iron oxide electrodes.* Solar Energy, 2007. **81**(11): p. 1369-1376.

90. Souza, F.L., et al., *Nanostructured hematite thin films produced by spin-coating deposition solution: Application in water splitting.* Solar Energy Materials and Solar Cells, 2009. **93**(3): p. 362-368.

91. Kumari, S., et al., *Spray pyrolytically deposited nanoporous Ti $^{4+}$ doped hematite thin films for efficient photoelectrochemical splitting of water.* International Journal of Hydrogen Energy, 2010. **35**(9): p. 3985-3990.

92. Kumar, P., et al., *Electrodeposited zirconium-doped α-Fe_2O_3 thin film for photoelectrochemical water splitting.* International Journal of Hydrogen Energy, 2011. **36**(4): p. 2777-2784.

93. Liu, Y., Y.-X. Yu, and W.-D. Zhang, *Photoelectrochemical properties of Ni-doped Fe_2O_3 thin films prepared by electrodeposition.* Electrochimica Acta, 2012. **59**: p. 121-127.

94. Lian, X., et al., *Enhanced photoelectrochemical performance of Ti doped hematite thin films prepared by the sol–gel method.* Applied Surface Science, 2012. **258**(7): p. 2307-2311.

95. Shen, S., et al., *Effect of Cr doping on the photoelectrochemical performance of hematite nanorod photoanodes.* Nano Energy, 2012. **1**(5): p. 732-741.

96. Lee, C.-Y., et al., *Si-doped Fe_2O_3 nanotubular/nanoporous layers for enhanced photoelectrochemical water splitting.* Electrochemistry Communications, 2013.

97. Frites, M., Y.A. Shaban, and S.U. Khan, *Iron oxide (n-Fe_2O_3) nanowire films and carbon modified (CM)-n-Fe_2O_3 thin films for hydrogen production by photosplitting of water.* International Journal of Hydrogen Energy, 2010. **35**(10): p. 4944-4948.

98. Bak, A., W. Choi, and H. Park, *Enhancing the photoelectrochemical performance of hematite (α-Fe_2O_3) electrodes by cadmium incorporation.* Applied Catalysis B: Environmental, 2011. **110**: p. 207-215.

99. Kim, J.K., et al., *Synthesis of transparent mesoporous tungsten trioxide films with enhanced photoelectrochemical response: application to unassisted solar water splitting.* Energy & Environmental Science, 2011. **4**(4): p. 1465-1470.

100. Yang, B., et al., *Enhanced photoelectrochemical activity of sol-gel tungsten trioxide films through textural control.* Chemistry of Materials, 2007. **19**(23): p. 5664-5672.

101. Giannouli, M. and G. Leftheriotis, *The effect of precursor aging on the morphology and electrochromic performance of electrodeposited tungsten oxide films.* Solar Energy Materials and Solar Cells, 2011. **95**(7): p. 1932-1939.

102. Pokhrel, S., et al., *Synthesis, Mechanism, and Gas-Sensing Application of Surfactant Tailored Tungsten Oxide Nanostructures.* Advanced Functional Materials, 2009. **19**(11): p. 1767-1774.

103. Santato, C., et al., *Crystallographically oriented mesoporous WO3 films: synthesis, characterization, and applications.* Journal of the American Chemical Society, 2001. **123**(43): p. 10639-10649.

104. Deepa, M., et al., *Influence of polyethylene glycol template on microstructure and electrochromic properties of tungsten oxide.* Solar Energy Materials and Solar Cells, 2008. **92**(2): p. 170-178.

105. Livage, J. and D. Ganguli, *Sol–gel electrochromic coatings and devices: a review.* Solar Energy Materials and Solar Cells, 2001. **68**(3): p. 365-381.

106. Marsen, B., et al., *Progress in sputtered tungsten trioxide for photoelectrode applications.* International Journal of Hydrogen Energy, 2007. **32**(15): p. 3110-3115.

107. Solarska, R., et al., *Tailoring the morphology of WO_3 films with substitutional cation doping: Effect on the photoelectrochemical properties.* Electrochimica Acta, 2010. **55**(26): p. 7780-7787.

108. Li, W., et al., *Photoelectrochemical and physical properties of WO_3 films obtained by the polymeric precursor method.* International Journal of Hydrogen Energy, 2010. **35**(24): p. 13137-13145.

109. Li, W., et al., *Effect of citric acid on photoelectrochemical properties of tungsten trioxide films prepared by the polymeric precursor method.* Applied Surface Science, 2010. **256**(23): p. 7077-7082.

110. Chen, Q., et al., *Preparation of well-aligned WO_3 nanoflake arrays vertically grown on tungsten substrate as photoanode for photoelectrochemical water splitting.* Electrochemistry Communications, 2012. **20**: p. 153-156.

111. Biswas, S.K. and J.-O. Baeg, *A facile one-step synthesis of single crystalline hierarchical WO_3 with enhanced activity for photoelectrochemical solar water oxidation.* International Journal of Hydrogen Energy, 2013. **38**(8): p. 3177-3188.

112. Kim, S. and J. Choi, *Photoelectrochemical anodization for the preparation of a thick tungsten oxide film.* Electrochemistry Communications, 2012. **17**: p. 10-13.

113. Memar, A., C.M. Phan, and M.O. Tade, *Controlling particle size and photoelectrochemical properties of nanostructured WO< sub> 3</sub> with surfactants.* Applied Surface Science, 2014. **305**: p. 760-767.

114. Galinska, A. and J. Walendziewski, *Photocatalytic water splitting over Pt-TiO_2 in the presence of sacrificial reagents.* Energy & Fuels, 2005. **19**(3): p. 1143-1147.

115. Lopes, T., et al., *Characterization of photoelectrochemical cells for water splitting by electrochemical impedance spectroscopy.* International Journal of Hydrogen Energy, 2010. **35**(20): p. 11601-11608.

116. Tauc, J., R. Grigorovici, and A. Vancu, *Optical properties and electronic structure of amorphous germanium.* Physica Status Solidi (B), 1966. **15**(2): p. 627-637.

117. Jitianu, A., et al., *Influence of the silica based matrix on the formation of iron oxide nanoparticles in the Fe_2O_3–SiO_2 system, obtained by sol–gel method.* Journal of Materials Chemistry, 2002. **12**(5): p. 1401-1407.

118. Cherepy, N.J., et al., *Ultrafast studies of photoexcited electron dynamics in γ-and α-Fe_2O_3 semiconductor nanoparticles.* The Journal of Physical Chemistry B, 1998. **102**(5): p. 770-776.

119. Ghobeiti Hasab, M., S. Seyyed Ebrahimi, and A. Badiei, *The effect of surfactant hydrocarbon tail length on the crystallite size of Sr-hexaferrite powders synthesized by a sol–gel auto-combustion method.* Journal of Magnetism and Magnetic Materials, 2007. **310**(2): p. 2477-2479.

120. Yang, B., et al., *Tungsten Trioxide Films with Controlled Morphology and Strong Photocatalytic Activity via a Simple Sol–Gel Route.* Catalysis Letters, 2007. **118**(3-4): p. 280-284.

121. KangáShen, P. and C. Alfred, *Study of electrodeposited tungsten trioxide thin films.* Journal of Materials Chemistry, 1992. **2**(11): p. 1141-1147.

122. Fainerman, V., et al., *Adsorption layer characteristics of Triton surfactants: 1. Surface tension and adsorption isotherms.* Colloids and Surfaces A: Physicochemical and Engineering Aspects, 2009. **334**(1): p. 1-7.

123. Li, W., et al., *Preparation and water-splitting photocatalytic behavior of S-doped WO3.* Applied Surface Science, 2012. **263**: p. 157-162.

124. Hong, S.J., et al., *Size effects of WO_3 nanocrystals for photooxidation of water in particulate suspension and photoelectrochemical film systems.* International Journal of Hydrogen Energy, 2009. **34**(8): p. 3234-3242.

125. Chakrapani, V., J. Thangala, and M.K. Sunkara, *WO_3 and W_2N nanowire arrays for photoelectrochemical hydrogen production.* International Journal of Hydrogen Energy, 2009. **34**(22): p. 9050-9059.

126. Butler, M., *Photoelectrolysis and physical properties of the semiconducting electrode WO_3*. Journal of Applied Physics, 1977. **48**: p. 1914.